Georgia Institute of Technology

Daniel Guggenheim School of Aerospace Engineering

CCL Report CCL-TR-2010-11-03

Subgrid Combustion Modeling for the Next Generation Combustion Code

Baris A. Sen, Srikant Srinivasan, Andrew Smith and Suresh Menon

Computational Combustion Laboratory
School of Aerospace Engineering
Georgia Institute of Technology
270 Ferst Drive
Atlanta, Georgia 30332-0150
http://www.ccl.gatech.edu

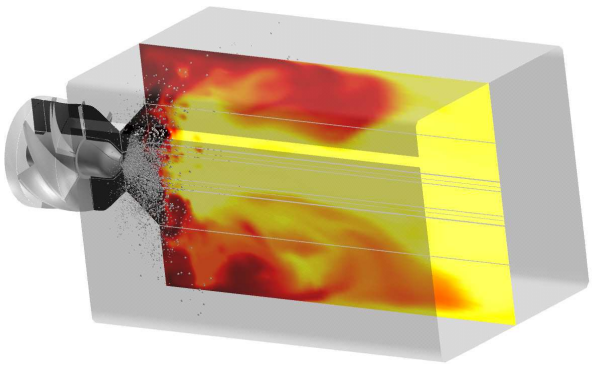

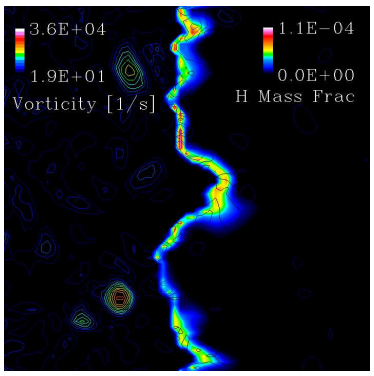

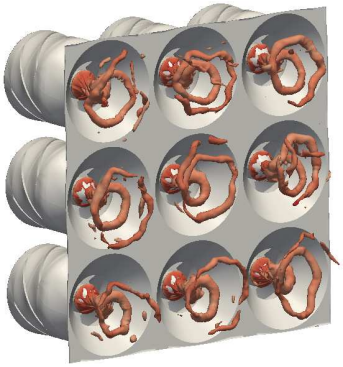

Sponsored by: *NASA GRC*
Contract Number: *NNX07AB32A*
Date: *November 2010*

TABLE OF CONTENTS

I TECHNICAL OBJECTIVES **1**

II INTRODUCTION **3**

III RESULTS AND DISCUSSION **7**

3.1 ANN for Turbulent Premixed Flame Modeling 7

3.1.1 Test cases 7

3.1.2 Description of the LEM tabulation and ANN training 9

3.1.3 Case A - LEMLES of turbulent flame-turbulence-vortex interaction 13

3.1.4 Case B - LEM studies of premixed methane/air flames 16

3.1.5 Case C - LEM studies of non-premixed syngas/air flames . . 18

3.1.6 ANN speed-up and memory savings 20

3.2 ANN for Turbulent Non-premixed Combustion Modelling with LEM-LES 22

3.2.1 Extinction and Reignition Studies 22

3.2.2 Numerical Setup and ANN Training 22

3.2.3 Extinction and reignition predictions 23

3.2.4 Scalar field conditional statistics 26

3.2.5 Syngas flame structure 29

3.2.6 Scalar dissipation rate statistics 32

3.2.7 Time and memory savings 34

3.2.8 Conclusions 35

3.3 TANN based Filtered Reaction Rate Closure for LES 38

3.3.1 ANN based Chemical Kinetics Model 38

3.3.2 Problem Setup and ANN training 39

3.3.3 TANN-LES validation: Case M 40

3.3.4 TANN-LES validation: Cases L and H 42
3.3.5 Capability of TANN for a range of Re and grid resolution . . 47
3.3.6 Conclusions 51
3.4 Application of TANN-LES in a Stagnation Point Reverse Flow Combustor (SPRF) 53
3.4.1 SPRF combustor 53
3.4.2 TANN-LES of the SPRF combustor 54
3.4.3 Time and memory savings 58
3.5 Conclusions 58
3.6 LEMLES of LDI combustor with ANN chemistry 60
3.6.1 ANN Training 60
3.6.2 Results for LEMLES with ANN 61
3.7 Kinetic Eddy Simulation of a Lean Direct Injection Combustor . . . 67
IV CONCLUSIONS **69**
V FUTURE WORK **72**

LIST OF FIGURES

3.1 Schematics of the actual problem and the LEM sub-domain 9

3.2 Effect of diffusivity for different species. 10

3.3 ANN training phase 11

3.4 ANN speed-up with respect to the number of connections. 12

3.5 Vorticity contour plot superimposed onto H surface plot obtained for the LEMLES of turbulence-flame-vortex interaction problem - (a) Case 3, (b) Case 4. 13

3.6 Comparison of the time-averaged species profiles obtained by the DI (•), the P-ANN (- - -), F-ANN (- . - .), and L-ANN (—) for Case A1. 14

3.7 Comparison of the instantaneous species profiles obtained by the DI (•), the P-ANN (- - -), F-ANN (- . - .), and L-ANN (—), at $t = 5t^*$ for Case A2. 15

3.8 Comparison of the instantaneous species profiles obtained by the DI (•), the P-ANN (- - -), F-ANN (- . - .), and L-ANN (—), at $t = 5t^*$ for Case A3. 16

3.9 Comparison of the instantaneous species profiles obtained by the DI (•), the P-ANN (- - -), F-ANN (- . - .), and L-ANN (—), at $t = 5t^*$ for Case A4. 17

3.10 Instantaneous scalar profiles obtained for Re_t =290 and at $N_{iter} = 5N^*$. Case B. 18

3.11 Conditional means of OH mass fraction and χ_{st} with respect to the mixture fraction for Case C. 18

3.12 Time evolution of the scalar profiles for Re_t =80 19

3.13 Comparison of the OH statistics obtained by the ANN-LEMLES and DNS at t_j = (a) 20 and (b) 40. (•) DNS, (- - -) Case M-1, (—) Case M-2, (...) initial data and (- . -) laminar flamelet value at extincion. . 24

3.14 Variation of the mean temperature at the stoichiometric mixture fraction obtained by the DNS (•), Case M-1 (- - -) and Case M-2 (—). . 24

3.15 Comparison of the instantaneous data obtained by the Case M-2 LEMLES using DI (•) and ANN (—) at t_j=4.5. 25

3.16 Conditional means of $\tilde{Y}_{CO}$ and $\tilde{Y}_{H_2}$ at extinction (a, c) and reignition (b, d) obtained by ANN-LEMLES and DNS. (•) DNS, (—) ANN-LEMLES, (...) initial data and (- . -) laminar flamelet value at extincion. 26

3.17 Conditional means of the $\tilde{Y}_{CO_2}$ and $\tilde{Y}_H$ at extinction (a, c) and reignition (b, d) obtained by ANN-LEMLES and DNS. (•) DNS, (—) ANN-LEMLES, (...) initial data and (- . -) laminar flamelet value at extincion. 27

3.18 Conditional mean of the temperature at extinction (a) and reignition (b) obtained by ANN-LEMLES and DNS. (•) DNS, (—) ANN-LEMLES, (...) initial data and (- . -) laminar flamelet value at extincion. 28

3.19 The time variation of the PDF of temperature at the stoichiometric surface obtained by the ANN-LEMLES. 29

3.20 Instantaneous surface plot of $\tilde{Y}_{CO}$ ((a)-(b)) and $\tilde{Y}_{H_2}$ ((c)-(d)) mass fraction at $t_j = 20$ ((a)-(c)) and $t_j = 40$ ((b)-(d)) obtained by ANN-LEMLES. 30

3.21 Instantaneous surface plot of $\tilde{Y}_{OH}$ at (a) $t_j = 20$, (b) $t_j = 40$ obtained by the ANN-LEMLES and at (c) $t_j = 20$, (d) $t_j = 40$ obtained by the DNS. 31

3.22 Instantaneous surface plot of $\tilde{Y}_{HO_2}$ at (a) $t_j = 20$ and (b) $t_j = 40$ obtained by ANN-LEMLES. 32

3.23 Surface plot of $log_{10}(\tilde{\chi}_{st}/\chi_q)$ at (a) $t_j = 20$ and (b) $t_j = 40$ obtained by ANN-LEMLES. 33

3.24 PDF of normalized logarithm of scalar dissipation rate at the stoichiometric mixture fraction at $t_j = 30$. (—) DNS, (- - -) ANN-LEMLES, (-..-..-) log-normal distribution 34

3.25 PDFs of normalized logarithm of scalar dissipation rate at the stoichiometric mixture fraction at (a) $t_j = 20$ and (b) $t_j = 40$ obtained by ANN-LEMLES. (•) log-normal distribution, (—) $\tilde{\chi}$, (- - -) $\tilde{\chi}_{CO}$, (-..-..) $\tilde{\chi}_{OH}$. 35

3.26 The time variation of the PDF of $\tilde{\chi}$, $\tilde{\chi}_{CO}$, $\tilde{\chi}_{OH}$ at the stoichiometric surface obtained by the ANN-LEMLES. 36

3.27 Conditional mean of OH mass fraction obtained by TANN-LES and DNS. (•) DNS, (—) TANN-LES at $t_j = 20$; (⧫) DNS, (- - -) TANN-LES at $t_j = 40$; (- . -) laminar flamelet value at extinction. 41

3.28 Conditional means of (a) CO and (b) H_2 mass fraction obtained by TANN-LES and DNS. (•) DNS, (—) TANN-LES at $t_j = 20$; (⧫) DNS, (- - -) TANN-LES at $t_j = 40$; (- . -) laminar flamelet value at extinction. 42

3.29 Mean value of the PDF of Y_{OH} conditioned on mixture fraction calculated by LANN-LES, TANN-LES and EBU-LES at t_j = (a) 20 and (b) 40. 42

3.30 (a) Variation of the mean of temperature at stoichiometric mixture fraction with respect to non-dimensional time for Case L, (b) Variation of the mean χ/χ_q at stoichiometric mixture fraction with respect to non-dimensional time for Case L 43

3.31 Variation of mixture fraction (Z) along the 1D standalone LEM domain at the DNS level and the LES level 44

3.32 Conditional mean of temperature and Y_{H_2O} at extinction (a and c) and reignition (b and d) 45

3.33 Variation of the PDF of temperature on the stoichiometric plane at extinction: black and reignition: red. Continuous line: DNS, Dashed line: TANN-LES 46

3.34 Variation of the PDF of H_2O mass fraction on the stoichiometric plane at (a) extinction and (b) reignition. Black continuous line: DNS data, Red continuous line: beta pdf corresponding to DNS data, Black symbols: TANN-LES data, Red symbols: beta pdf corresponding to TANN-LES data. 47

3.35 Case H (a) Variation of the mean of temperature at stoichiometric mixture fraction with respect to non-dimensional time, (b) Variation of the mean χ/χ_q at stoichiometric mixture fraction with respect to non-dimensional time 47

3.36 Variation of PDF of temperature, H_2O and OH mass fraction on stoichiometric plane at extinction: (a),(c),(e) and reignition: (b),(d),(f) for Case H with TANN-2 49

3.37 PDF of the normalized scalar dissipation rate at the stoichiometric mixture for Case H with TANN-2. (a) C-Grid, (b) F-Grid 50

3.38 Distribution of χ_{st} with respect to temperature on the stoichiometric plane for Case H. Black dots: $t_j = 10$, Red dots: $t_j = 40$ for (a) C-GRID, (b) F-GRID 50

3.39 Comparison of the variation of (a) mean temperature and (b) mean χ/χ_q on the stoichiometric plane for Case L using TANN-1 and TANN-2 50

3.40 Schematics of the SPRF combustor [1]. 54

3.41 Side and cross-sectional views of the grid used for the LES. 55

3.42 (a) Instantaneous and (b) time-averaged temperature surface plot. . . 55

3.43 (a) Instantaneous and (b) time-averaged CH_4 mass fraction surface plot. 56

3.44 Comparison of the time-averaged (a) axial velocity and (b) temperature along the centerline. 56

3.45 Comparison of the time-averaged (a) CH_4 and (b) CO_2 mole fraction along the centerline. Experiment, LEMLES, TF-LES and EBU-LES, from [1]. 57

3.46 Comparison of the time-averaged axial velocity radial profiles at four sections. (•) Experiments, (—) LEMLES with DTSE and (- - -) TANN-LEMLES. Experiments and LEMLES from [1]. 57

3.47 ANN training phase. 61

3.48 Time-averaged centerline axial velocity 62

3.49 Instantaneous centerline temperature 62

3.50 Instantaneous centerline pressure 63

3.51 Instantaneous centerline fuel mass fraction 63

3.52 Instantaneous centerline CO mass fraction 64

3.53 LEMLES with ANN: temperature contours and fuel droplets after 1τ 64

3.54 LEMLES with ANN: CO_2 mass fraction after 1τ 65

3.55 LEMLES with ANN: CO mass fraction after 1τ 65

3.56 LEMLES with ANN: Fuel mass fraction after 1τ 66

3.57 Multiblock LDI combustor grid 67

3.58 Subgrid length scale near walls without proper limiting 67

3.59 Subgrid length scale and $\ell^{sgs}/\overline{\Delta}$ profiles in the swirler region with near-wall limiting 68

3.60 $\ell^{sgs}/\overline{\Delta}$ in the swirler vane region 68

5.1 Updated LDI grid with 3.65 million cells 73

5.2 9 injector LDI grid with 19 million cells 74

5.3 9 injector LDI grid clustering at the dump plane 75
5.4 9 injector LDI grid clustering at $x/D_0 \approx 2$ 76
5.5 9 injector LDI instantaneous density contour for cold flow simulation 77

LIST OF TABLES

3.1 Test Cases 7

3.2 LEMLES Test Cases 8

3.3 Flame Parameters for LEMLES Case A 8

3.4 List of ANN architectures and their properties used for Case C 12

3.5 Memory saving by ANN for Case A 20

3.6 Timing for Case B 20

3.7 Timing for Case C 20

3.8 Test Case Specifics 22

3.9 Comparison of Speed-up Obtained by Different Models 35

3.10 DNS parameters for test cases 40

3.11 LES grid resolution 40

3.12 Boundary conditions used for the LES [1]. 54

3.13 Speed-up obtained for 12 steps methane skeletal mechanism. 58

CHAPTER I

TECHNICAL OBJECTIVES

(1) *Comparison of different ANN training table generation methodologies on the LEM-LES of premixed flames.*

In our previous reports three different approaches to generate ANN training tables were discussed. This report mainly aims to evaluate the accuracy of the ANNs trained on these differen tabulation methodologies. For this purpopose, a series of premixed flame-turbulence-vortex interaction studies with different level of turbulence and premixing are conducted. Results obtained by the ANNs trained on the tables constructed through different tabulation methodologies are compared against each other and the direct integration technique.

(2) *Evaluating the generalizability of the ANNs trained on stand-alone LEM computations.*

The thermo-chemical tables generated through stand-alone LEM cannot contain all the states accessed during the computations due to the memory limit. In order to understand the capability of ANNs trained on these thermo-chemical tables to fill the gaps in the database, the stand-alone LEM computation is repeated by using ANN to calculate the reaction rates.

(3) *Development of an ANN for filtered reaction rate modeling*

A novel approach to create multi-dimensional look-up tables using off-line linear eddy mixing (LEM) model computations for the filtered chemical source terms is proposed. These multi-dimensional tables are then used together with the artificial neural networks (ANN) approach [2] to directly account for the filtered reaction rates in large eddy simulation (LES) of reactive flows. This approach, called Turbulent ANN or TANN, is an extension of an earlier strategy [2, 3, 4], where the ANN was used to retrieve the instantaneous (unfiltered) reaction rates. The proposed methodology is used for the LES of both non-premixed and premixed turbulent reacting cases that offer different types of modeling challenges.

(4) *TANN for chemical kinetics calculations in the LES of the SPRF combustor*

The stagnation point reverse flow combustor (SPRF) is simulated using TANN to evaluate its peformance in a practical application. The results are compared with data as well as a previous LEMLES study.

(5) *ANN for chemical kinetics calculations in the LEMLES of LDI combustor*

Thermo-chemical database is created by stand-alone LEM computations with conditions relevant to the LDI combustor. The ANN trained on this database is used to replace the chemical kinetics calculations on the sub-grid.

(6) *Two-equation subgrid kinetic energy model for VLES-LES*

A two-equation subgrid kinetic energy model solves transport equations for both subgrid kinetic energy and the product of subgrid kinetic energy and a representative

length scale. The addition of the second equation allows for a length scale not explicitly set to the grid size as traditionally done in implicit LES thus there is a smooth transition between LES and very large eddy simulation (VLES).

CHAPTER II

INTRODUCTION

Turbulent combustion is described as the continuous distortion of the local flame front with eddies distributed over a wide range of length and time scales [5]. The response of the flame front depends on the combined effect of molecular diffusion, turbulent transport and chemical reaction occurring across the flame, without any clear scale separation. Eventually the flame may experience complex, unsteady, local and/or global features such as extinction, re-ignition and quenching. From a computational point of view, direct numerical simulation (DNS) of high Reynolds number flows (typical of turbulent combustion) are not yet affordable, and thus, to render a practical solution to the turbulent combustion processes, the governing equations are solved either on a time (Reynolds Averaged Navier Stokes (RANS)), or space averaged (Large Eddy Simulation (LES)) sense [6]. For all of these methodologies, what is common, however, is the calculation of the chemical reaction rates: a set of coupled, non-linear ordinary differential equations (ODEs) has to be solved. It must be noted that the accurate prediction of the aforementioned features need radical species information [5, 7, 8]. However, as the number of the species increases, the size of the system of ODE increases as well. Furthermore, since the radical species have time scales different by several orders of magnitude compared to the major species, the ODEs become stiff as well [9]. Thus, the process of calculating chemical source terms adds further computational burden to the flow simulation and needs to be handled carefully in a cost efficient manner.

Many approaches for efficient kinetics evaluation has been reproted in the literature. The look-up table approach (LUT) [10], intrinsic low-dimensional manifolds (ILDM) [11], and, *in-situ* adaptive tabulation (ISAT) [12], have all shown speed-up of the chemical kinetics calculations. LUT and ILDM depends on pre-computing and tabulating the reaction rate and/or the species information. Since generating a structural table for the whole thermo-chemical state space require tabulation in $(Ns+2)$ dimensions, for most of the applications the dimensions are reduced by using several reaction progress variables. This procedure is handled automatically in ILDM and the intrinsic manifold can be found directly by a dynamical system approach, which is not the case for LUT. One major drawback for both ILDM and LUT is that the information on the thermo-chemical state space that is going to be accessed by the flow solver is not known *a-priori*, and thus, huge tables have to be created. ISAT, on the other hand, constructs the look-up table during the actual flow simulation, and only the accessed region is stored. Thus it yields a considerable amount of memory savings compared to ILDM and LUT. However, the ISAT table may also keep increasing beyond the memory limit of the PC parallel clusters especially for LES applications [13].

The main purpose of the current study is to propose a tabulation strategy and

an interpolation scheme, that may predict the thermo-chemical state space *a-priori* (unlike ILDM), and which can reduce locally memory needs (unlike ISAT) without any loss of accuracy and with speed-up. Here, the tabulation is achieved by using the stand-alone Linear-Eddy Mixing (LEM) [14, 15, 16] model calculations. LEM has been previously demonstrated to account for the interaction between turbulent transport, molecular diffusion and chemical reaction at their respective time and length scales [17, 18, 19]. In LEM, the diffusion-reaction equation is solved on a one-dimensional line and the turbulent stirring is handled explicitly by a stochastic model. Once the thermo-chemistry is extracted through stand-alone LEM computations, an Artificial Neural Networks (ANN) architecture is trained on this data-set. ANN is basically an interpolation scheme that can be used to map arbitrary number of inputs to outputs [20]. The strength of the ANN lies in the fact that, through a learning (training) stage it can adapt itself to any function by the use of interconnected non-linear processing elements [21]. The learning process involves adjusting the synaptic weights to get the most appropriate output for a given input. Thus, once it is trained, unlike LUT, ILDM, and ISAT, there is no need to couple the flow solver with a multi-dimensional thermo-chemical table, or a direct solver for the stiff kinetics equations.

ANN for the reactive flow computations has been used by different research groups in the past. Blasco et al. [22] performed one of the first attempts to incorporate ANN into chemical kinetics calculations, where the accuracy of the proposed model was tested in a plug flow reactor calculation. A speed-up of 2700 with ANN was obtained when compared to direct integration (DI). In a later study [23], time step size was included as an additional parameter, and it was reported that the memory requirement for such an ANN computation requires only 24 kbytes as opposed to 19934 kbytes for tabulated chemistry calculations. Choi and Chen [24] trained ANN for ignition delay time calculations, where they used temperature, pressure, equivalence ratio and exhaust gas re-circulation as input for their predictions. The ANN model was later coupled with a well-mixed reactor solver to predict the ignition delay time, and a speed-up of 600 was obtained. Finally, an integration of ISAT with ANN for a partially stirred reactor computation was studied by Chen et al. [25], where ANN was trained based on an already existing ISAT table. Same approach was later re-visited by Kapoor et al. [26] and applied to unsteady scalar field evolution within LEM approach.

In more recent studies, ANN has been used within the LES computations of reactive flows. The work by Kempf et al. [27] investigated the structure of the SANDIA Flame D [28] by LES, where ANN was used to store a steady flamelet library to provide species mass fractions, density and viscosity. The thermo-chemical state-space was parametrized by the filtered mixture fraction, sub-grid variance of the mixture fraction and the filtered scalar dissipation rate. The sub-grid distributions were modeled by presumed-shaped PDFs. They reported that the ANN reduces the storage size of the chemistry library by three orders of magnitude having almost same efficiency with a linear interpolation scheme. Ihme and co-workers [29] used ANN to store a flamelet library and applied it to a bluff body stabilized flame. A general strategy to optimize ANNs (O-ANN) for the given number of layers and neurons per layers was also proposed. The ANN performance with respect to accuracy, data

retrieval time and storage requirements was compared with the structured tabulation methods, and it was shown that ANN yielded comparable accuracy with considerably lower storage and computational time.

Previous work by Kempf et al. [27] and Ihme et al. [29] used ANN to store flamelet libraries in connection with the presumed PDF approach, where the thermo-chemistry is not computed directly within the LES, but rather interpolated from a look-up table. In this approach, flamelet itself already provides a considerable amount of speed-up compared to directly simulating the scalar field, and the merit of using ANN lies in the memory savings. An alternative approach is to use ANN to directly represent the multi-step kinetics within the LES approach, and this has been recently investigated by Sen and Menon [4]. Here, a series of simulations of the *unsteady* evolution of flame-vortex interactions (FVI) were used extract the thermo-chemical information for ANN training table construction. These simulations of FVI showed that, although the computations are started for a single large scale vortex, actually a large number of scales are present over the entire simulation period. Hence, each test case with an initial single vortex of a given size provided additional data over a much wider range of scales. The ANN was later used to replace the DI based on a 14-species, 11-steps reduced chemical kinetics mechanism within the LES sub-grid calculations of premixed, syngas/air flames. A speed-up factor of 11.22 with considerable amount of memory savings was reported.

The current report is providing a discussion for extending the approach developed earlier [4]. The key difference lies in the fact that, in the current study the thermo-chemical states for ANN training are extracted from stand-alone LEM simulations, rather than the DNS of FVI done previously. The major advantage in this strategy is that LEM allows explicitly incorporating (albeit indirectly) the effect of the turbulent small-scale eddies on the reaction kinetics. This is in contrast to our previous approach [4] where only the effect of deterministic vortices on the reaction kinetics was considered. Both strategies attempt to capture *unsteady* flame-turbulence-vortex interaction effects during the ANN database development. This approach is therefore considered a new strategy for ANN training. Once the ANN is trained, we use it in both LES and in the stand-alone LEM to demonstrate its ability. Different ANNs are trained for different kinetics model using the same strategy and therefore, demonstrates the generalibility of the approach.

In a variation over the above mentioned approach call the Turbulent ANN (TANN), the ANN is trained using a modified procedure to yield the filtered reaction rate directly. Here we still explore the multi-scale flame-turbulence interaction physics in the off-line LEM simulation to generate tables that contain the scalar information including the effect of local interaction between the small-scale processes (turbulent stirring, molecular diffusion) and the chemical reactions, but this time use them to estimate the filtered reaction rates for LES or even conventional RANS. As mentioned above the ANN as a subgrid combustion model was used previously successfully in combination with the flamelet approach to achieve memory savings and decrease the interpolation errors [27, 29]. The current approach, in contrast to the ANN-flamelet approach, attempts to combine the scalar field with the turbulence PDF (without *a-priori* assumptions), resulting a new approach to estimate the filtered chemistry

$\bar{\dot{\omega}}_k$ within the LES. Note that, once $\bar{\dot{\omega}}_k$ is estimated, LEM is no longer needed, and thus, a significant reduction in cost is apparent. Hence a new type of closure for the filtered reaction rate using the TANN approach is presented with accompanying demonstrations that prove that the predictions are still accurate for two distinctly different turbulent combustion cases using this method with considerable reduction in simulation cost. TANN is then used to simulate the Stagnation Point Reverse Flow combustor (SPRF) using a CH4/air 16-step mechanism. The quality of results are assessed with reference to data and a previous LEMLES study and peformance gains of this approach, quantified.

The main objective of large eddy simulation is to reduce the computational cost with minimal loss of accuracy as compared with direct numnerical simulations. For high Reynolds number wall-bounded flows the computational requirement for LES is still very expensive thus methods are necessary for modeling subgrid turbulence on coarse LES grids. Hybrid RANS-LES models generally require ad-hoc blending functions to transition between the RANS and LES regions. If improperly blended, the hybrid solution can actually be worse than that of the RANS or LES solution alone [30]. To avoid such problems, a single model for coarse grids known as the kinetic eddy simulation model was developed [31]. The model which includes a second subgrid turbulence equation which explicitly calculates the subgrid turbulence length scale acts as a bridge between large eddy simulation and very large eddy simulation (VLES). This model is investigated and evaluated for simulations of a lean direct injection (LDI) combustor.

The rest of the report is organized as follows: The mathematical formulation of the LEM, ANN and other subgrid models is reviewed in the next section, which is followed in Section 3.1.1 by the description of the test cases used to evaluate the accuracy of the proposed ANN methodology. ANN is used to replace a stiff ODE solver within the LES and stand-alone LEM computations. Results are presented in Section 3 while conclusions are drawn in the final section.

CHAPTER III

RESULTS AND DISCUSSION

3.1 ANN for Turbulent Premixed Flame Modeling

3.1.1 Test cases

The proposed methodology for thermo-chemical database construction and ANN accuracy is tested for three distinct reduced (or skeletal) mechanisms and test cases (Table 3.1). The first case (Case A) is essentially a series of LEMLES of flame-turbulence-vortex interaction computations (Table 3.2). For the LES cases, the ANNs trained on the thermo-chemical data extracted from stand-alone LEM computations are used to replace the stiff ODE solver to predict the instantaneous reaction rates at the sub-grid model. The strategy for the remaining cases (Case B and C) is to test the ANN capabilities within the stand-alone LEM computations for different flames and kinetics mechanisms. Similar to Case A, the thermo-chemical database is constructed with stand-alone LEM computations, and the ANNs are trained on the data-base. Once training is achieved, ANN is used to replace the DI technique to asses the ANN accuracy. Multiple test simulations are conducted in each of the test cases (Cases A-C).

Case A is a series of LEMLES computations conducted for a premixed syngas (PSI [32])/air flame. The LEMLES cases are listed in Table 3.2. The LES cases are selected so that they can be compared with the earlier study [4], where the ANNs were trained using tables extracted from the FVI simulation. Here, we compare the baseline LEMLES using (a) stiff ODE solver, (b) ANN trained on FVI (F-ANN) [4], (c) ANN trained on LEM (L-ANN) [3], and (d) ANN trained on laminar premixed flame simulations (P-ANN) [33]. The flame properties for the flames considered in the LEMLES computations are summarized in Table 3.3. For all cases the ratio of the integral length scale to the laminar flame thickness (L_F) is selected to be 5, and all the flames are in the thin reaction zone regime. The LES for all cases is initialized by using a 1D, laminar, steady solution for a premixed flame. Then, a pair of counter-rotating vortices are superimposed on an isotropic background turbulence to induce both large and small scale wrinkling of the flame front. The details of the initialization process can be found in our earlier studies [32, 33, 4]. A 64^3 grid is used for all cases, and the

Table 3.1: Test Cases

	Mode	ANN Testing	Reduced Mechanism
Case A	Premixed syngas/air	LES	10 steps, 14 species (skeletal)
Case B	Premixed methane/air	Stand-Alone LEM	12 steps, 16 species (skeletal)
Case C	Non-premixed syngas/air	Stand-Alone LEM	21 steps, 11 species

Table 3.2: LEMLES Test Cases

	u'/S_L	$U_{C,max}/S_L$	D_C/L_F	ϕ
Case A1	5	–	–	0.6
Case A2	5	50	5	0.6
Case A3	10	50	5	0.8
Case A4	10	50	5	0.6

Table 3.3: Flame Parameters for LEMLES Case A

Equivalence Ratio	S_L [m/s]	l_f [m]
0.6	0.2105	8.755×10^{-4}
0.8	0.3920	5.611×10^{-4}

grid resolution is approximately four times larger than the Kolmogorov's length scale ($\Delta x = 4 \times \eta$). For sub-grid scalar field evolution, 24 LEM cells are used within each LES grid, allowing a resolution in the sub-grid approximately of the order of η. The chemical kinetics is represented by a 14-species, 10-step reduced skeletal mechanism. Based on the u' and L selected for each of the cases, the thermo-chemistry is extracted by running stand-alone LEM computations for a fixed L and varying Re_t. The process of creating the LEM tables is described in details later in Section 3.1.2.

The second series of test cases (Case B) are selected to construct the thermo-chemical state-space occuring inside the stagnation point reverse flow (SPRF) combustor [1]. Rather than performing the actual LES, here we perform stand-alone LEM computations for the SPRF conditions and evaluate the performance of the ANNs within the LEM framework. Characteristic eddy size (L), fluctuating velocity (u') and the local viscosity obtained in a separate LEMLES of this combustor [1] are used to find the critical Re_t. The characteristic eddy size (integral length scale) is selected to be the radius of the whole injector assembly (L =8.25×10^{-3}m). Also, previous LEMLES studies of this configuration obtained u' ∼10 m/s [1]. The stand-alone LEM computations are performed for 20 (N_{Re_t}=20) different Re_t values ranging from 10 to 400 for a fixed L. For the given each different Re_t, both η and λ are changing, so the initial scalar field experiences different level of interaction. This is similar to the process observed in turbulent flames. It is also found that, as the N_{Re_t} is further increased, the states accessed by the LEM computations become nearly identical for two consecutive simulations, thus N_{Re_t}=20 is found to be an optimum value for this particular case.

The last case (Case C) is based on a DNS of a temporally evolving, plane jet, syngas/air flame from the literature [34, 35]. The DNS is performed on approximately 350M grid points ($\Delta x = 2 \times \eta$), using a relatively detailed syngas/air chemical kinetics mechanism with 11 species and 21 reactions. The flame is reported to exhibit strong flame-turbulence interaction with local extinction and re-ignition, which makes it a challenging test case to evaluate LEM based table construction and ANN. The maximum Re_t for this case is reported to be 175 in the DNS study. Also, the integral length scale is roughly $H/3$, with H denoting the initial fuel jet height [34]. The stand-alone LEM computations are performed for 20 (N_{Re_t}=20) Re_t values ranging

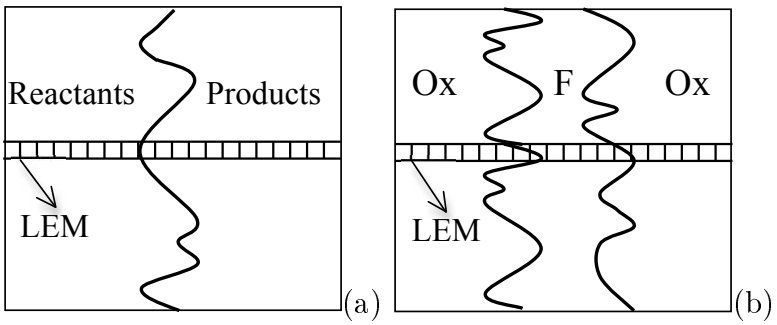

Figure 3.1: Schematics of the actual problem and the LEM sub-domain

from 10 to 180, for a fixed L.

It is noted that LEMLES of Cases B-C using the ANNs developed in this study are currently being conducted and these results will be reported in the near future. Hence, we focus primarily on the development and use of ANN for these test cases. Future studies will emlpoy these ANN in an actual LEMLES of the corresponding problem.

3.1.2 Description of the LEM tabulation and ANN training

3.1.2.1 LEM tabulation

The ANN training table is constructed by using stand-alone LEM computations for all cases presented in this report. The details of the tabulation process (i.e, reduced mechanism, range of Re_t and L etc.) are different for each test case. The LEM computations start from an initially laminar profile, which is also different based on the type of the problem (i.e. premixed or non-premixed). The LEM domain for premixed cases extends from reactants to the products, whereas for non-premixed cases, it spans the oxidizer and fuel streams, as shown schematically in Fig. 3.1. However, it should be noted that the basic structure of the tabulation and the capabilities of the stand-alone LEM computation are the same for all cases.

For the premixed cases (Case A and B) the initial profile is calculated as function of the equivalence ratio and the reactant temperature. For the non-premixed simulations, however, strain rate is an additional parameter to the thermodynamic variables. From the LEM perspective, once the non-premixed simulations are started from an initial strain rate, the small scale turbulent structures will change the straining locally resulting in different scalar field evolution based on the Re_t and L. Hence, non-premixed LEM computations (Case C) are initialized for a relatively lower strain-rate than the one used in the DNS computations [34]. During the simulation it is expected that the database created with LEM computations will cover a broader range in the compositional state-space, compared to the case initialized by a strain rate very close to the extinction. As will be discussed later, an increase in Re_t results in flame extinction although the initial strain rate is very low.

Once the scalar field is initialized, the stand-alone LEM for all cases is run with

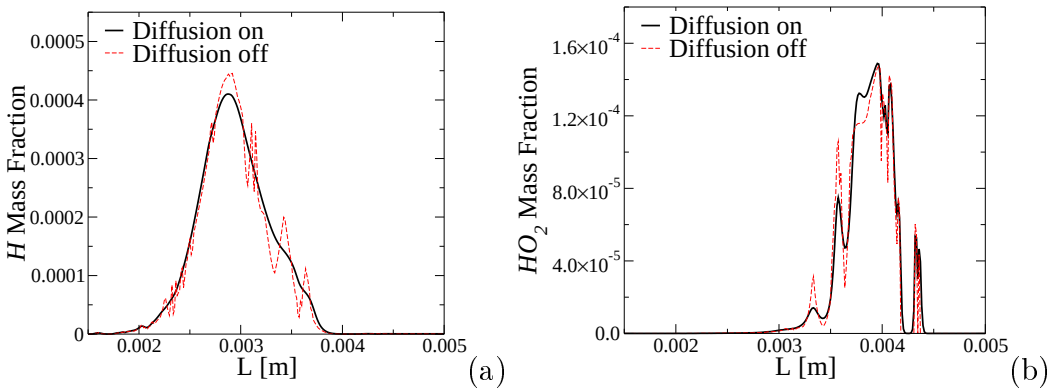

Figure 3.2: Effect of diffusivity for different species.

a given time step size (Δt). Here it should be noted that, for the given Δt, both turbulent stirring and molecular diffusion proceeds with sub-iterations with their respective time steps (Δt_{stir}, Δt_{diff}). Thus, the LEM evolution is independent of Δt.

For two LEM computations with different Re_t, the number of stochastic turbulent stirring events per given time interval (Δt) is distinct, which results in a different level of flame-turbulence interaction process. Also, the diffusion process counteracts turbulent stirring at its own time and length scale. A typical picture demonstrating these unsteady interactions is shown in Fig. 3.2 for Case C. For the given Re_t, the dashed lines represent the LEM result obtained without simulating the effect of diffusion. The LEM computation with diffusion turned on exhibits smooth variation for both of the species. Here, first thing to note is that the scalar profile obtained for HO_2 is highly wrinkled, whereas H seems almost not affected by the turbulent stirrings. This is a direct result of using non-equal diffusion coefficients for the species. Hence, HO_2 is more sensitive to the turbulent forcing, which can be captured through LEM diffusion sub-iterations.

3.1.2.2 ANN training

Once the LEM database is created, the instantaneous species reaction rates corresponding to each state are calculated and added to the look-up table, which is used for ANN training. Since each LEM iteration requires a certain number of diffusion and stirring sub-iterations, the generated database cannot be expected to contain all the available states. Such an attempt would require tabulation of a table of Ns dimensions, which is probably not affordable for large chemical mechanisms. However, if well trained, ANN has the potential to fill out the gaps between the existing states in the database and provide predictions to the states that it was not trained for. This is one of the goals of this study.

The temperature-H_2 reaction rate hyperplane from the training table generated for test Case C is shown in Fig. 3.3 (a). There are approximately 5M states included within the training table. In order to increase the sensitivity of the reaction rate calculations with respect to the temperature, the whole database is divided into nine

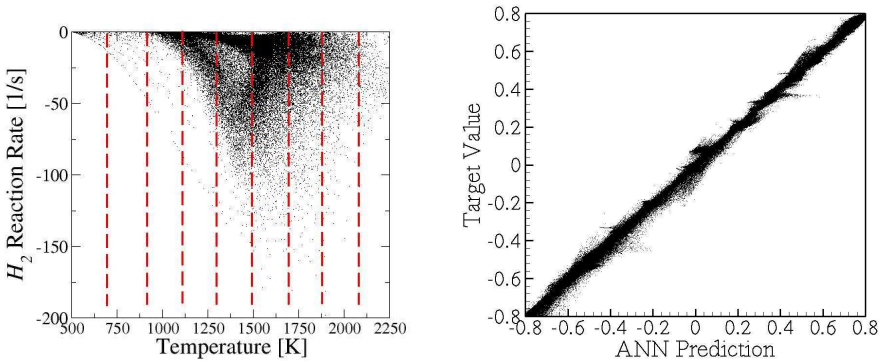

(a) Thermo-chemical database accessed by the 1D-LEM solver.

(b) Correlation obtained by the ANN testing

Figure 3.3: ANN training phase

equi-distance temperature bins. The number of bins are selected so as to leave at least 100K datapoints at each bin to achieve a proper training. The effect of having non-equal bin sizes on the accuracy of ANN training is underway and will be addressed in a future study. The boundaries of each temperature bin is shown with dashed lines in the figure. Once all states are divided into temperature bins, ANN training is achieved for each bin separately. A multi-layer perceptron type of ANN is used for the training with arbitrary number of hidden layers and PEs. The inputs for the ANNs are the species mass fractions and the temperature, whereas the output is the reaction rates of all species.

Approximately 85 % of the database is selected randomly and used for training the selected ANN architecture. The remaining 15 % of the database (test table) is then used for testing the ANN during the training phase. In order to avoid over-training, which would cause ANN to memorize the training data and may avoid it to be general, the training is stopped if there is no improvement for consecutive iterations. A typical correlation curve obtained during the training phase is given in Fig. 3.3 (b). Here, the y axis is the actual value of the test data, whereas x axis denotes the ANN predictions. The figure shows the correlation obtained for all temperature bins, and for all the species, and proves that a good correlation is achieved on the training phase.

The correlation curve shown in Fig. 3.3 (b) is obtained for an ANN architecture with 5, 3, 2 number of PEs at each hidden layer, respectively (hereafter, identified as 5/3/2 ANN). The selection of the number of hidden layers and number of PEs for each hidden layer is an important issue that has to be handled in care. In the current study, the optimum ANN is selected with experimenting different ANNs based on the speed-up provided and the RMS error achieved. It is known that the number of floating point operations for a given ANN is a function of the number of connections between each PE. Figure 3.4 shows the ANN speed-up against using a stiff ODE solver

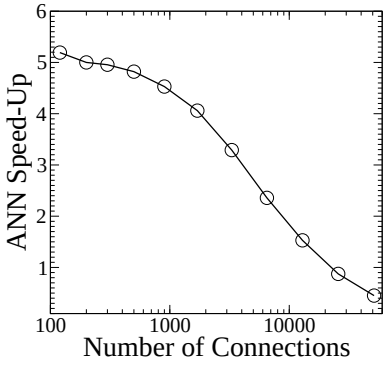

Figure 3.4: ANN speed-up with respect to the number of connections.

Table 3.4: List of ANN architectures and their properties used for Case C

ANN	Error	Connections	Time/(Iter×Sample)
5	-3.521	230	1.922×10^{-5}
10	-3.801	340	2.021×10^{-5}
20	-4.056	460	2.279×10^{-5}
5/4	-3.889	358	2.058×10^{-5}
10/5	-3.920	500	2.199×10^{-5}
20/5	-4.114	770	2.437×10^{-5}
20/10	-4.619	1080	2.635×10^{-5}
5/3/2	-4.201	371	2.060×10^{-5}
10/5/2	-4.327	574	2.259×10^{-5}
20/10/5	-4.870	1240	2.813×10^{-5}

with respect to the number of connections, and it is seen that the maximum speed-up that can be obtained for this particular reduced mechanism is slightly larger than 5. As the number of connections are increased, the speed-up decreases, and at 500 it is almost 4 % less than the ideal speed-up, which is still an acceptable value. Beyond 500, however, ANN speed-up seems to be more sensitive to the changes in the number of connections and it decreases exponentially. Eventually beyond 20K connections, ANN is slower than using a stiff ODE, which suggests that there should be a limit for the number of connections used in ANN computations. For this particular study, the limit is approximately 500, since it gives the best speed-up with respect to the number of connections.

Once the limit for maximum number of PEs is determined, different ANN architectures are investigated to obtain the optimum speed-up with respect to the ANN error. The error and the number of connections for some of the tested ANNs are summarized in Table 3.4. Here, the ANN error is calculated as

$$E = log\left((1/N_{test})\sum_{k=1}^{N_{test}}(1/(2I))\sum_{i=1}^{I}[d_i - y_i[k]]^2\right) \tag{3.1}$$

which is an average over the number of PEs at the output layer (I) and number of test

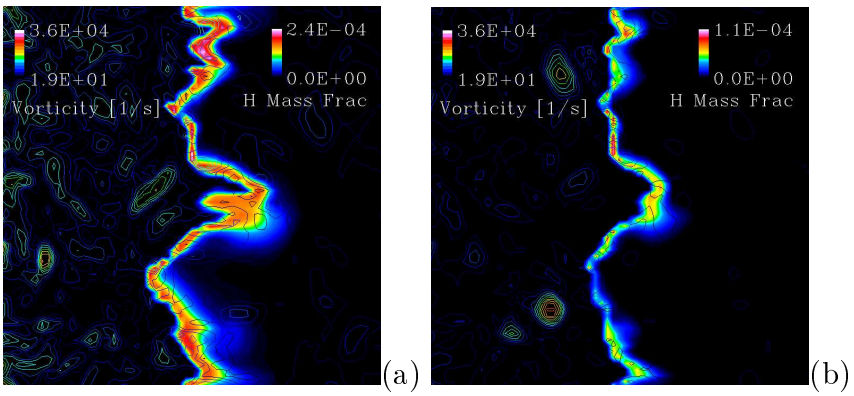

Figure 3.5: Vorticity contour plot superimposed onto H surface plot obtained for the LEMLES of turbulence-flame-vortex interaction problem - (a) Case 3, (b) Case 4.

samples (N_{test}). As seen in the Table, the best speed-up is obtained for a 3 hidden layer ANN architecture with 20, 10, 5 number of PEs at each hidden layer, respectively (hereafter identified as 20/10/5 ANN). However, the number of connections for this particular ANN is 1240, which is beyond the optimum limit obtained from speed-up analysis. Considering the speed-up and the error, 1 hidden layer ANN with 20 PEs and 3 hidden layer ANN with 5/3/2 PEs looks like and optimum ANN for this test Case C. It is noted that recently an automatic way of defining the optimum number of PEs for the given hidden layers has been proposed in the literature [36, 29] (O-ANNs), and for future studies the applicability of the algorithm with our new learning rule will be tested for LEM based tabulation procedure. The time required to do one training iteration per number of training and testing samples for the current ANN approach is given in Table 3.4. For the optimum case, with approximately 500K number of samples and 500 iterations (which is typical number of training iterations), it takes only 1.4 hours to finish the training, which is considerably quite reasonable. Of course, this cost may change with larger skeletal mechanisms and is an issue being looked at.

3.1.3 Case A - LEMLES of turbulent flame-turbulence-vortex interaction

The LEMLES cases are selected based on our earlier study [4], and are listed in Table 3.2. For the each given test case, the LEMLES is carried out using different kinetics evaluation strategies (DI, F-ANN, L-ANN, and P-ANN). The F-ANN is identical to the one used in our earlier calculation [4], and the whole methodology of creating the data-base and ANN training is not repeated here for sake of brevity. The training table for P-ANN is constructed based on performing laminar, 1-D, premixed flame calculations for multiple equivalence ratios. Our previous observations on premixed flames revealed that the species mass fractions may locally deviate from that obtained from the laminar flame calculations as a result of the unsteady mixing induced by the flame-turbulence interaction [33]. Hence, rather than creating a table for a single

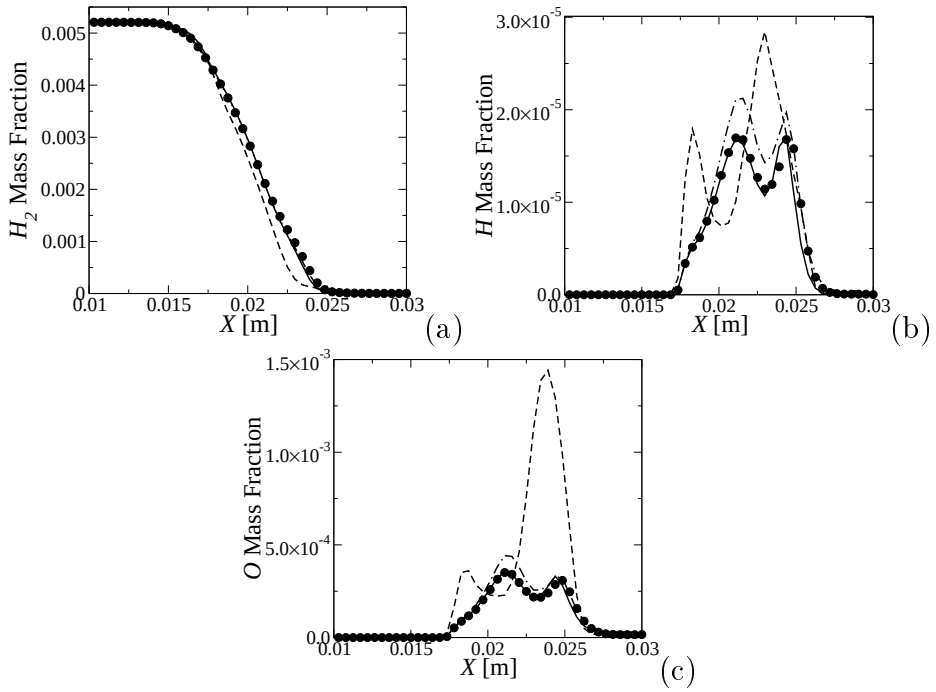

Figure 3.6: Comparison of the time-averaged species profiles obtained by the DI (•), the P-ANN (- - -), F-ANN (- . - .), and L-ANN (—) for Case A1.

equivalence ratio (Φ), the training table is formed for multiple-equivalence ratios, by changing Φ from 0.4 to 1.10, with a step size of 0.001 ($\Delta\Phi$ =0.001). The final training table includes approximately 482K total entries. For L-ANN, the training table is constructed similar to the way explained in Section 3.1.2. The stand-alone LEM code is run for a fixed L ($L = 5\times L_f$) and varying Re_t, for the values given in Table 3.2. The optimum ANN based on F-ANN for this case was previously found to be a three hidden layer 10/5 architecture [4]. It should be noted that the optimum ANN architecture depends highly on the training data, and should be different for each F-ANN, P-ANN and L-ANN. However, for comparison purposes, same ANN architecture is used for all ANN models considered in Case A.

The time-averaged and instantaneous species profiles obtained across the flame front at mid-y and z planes is used toevaluate the different ANN methodologies, and to compare them with the DI computations. The time averaged results for the variation of a major (H_2) and two intermediate species (H, O) across the flame front for Case A1 are presented in Figs. 3.6a-c. Other species show qualitatively similar trends and therefore not shown for brevity. Here, dots represent the LES results with DI, dashed lines P-ANN, dash-dot lines F-ANN and straight lines L-ANN. The agreement between all ANN models are acceptable for H_2 as seen in Fig. 3.6a. However, for H (Fig. 3.6b), the P-ANN exhibits the most error, with almost 1.5 times larger values than the DI predictions. P-ANN overpredicts the O mass fraction as well (Fig. 3.6c), suggesting that it is not very accurate for minor species prediction. The F-ANN successfully follows the same profile calculated by DI computations for all species

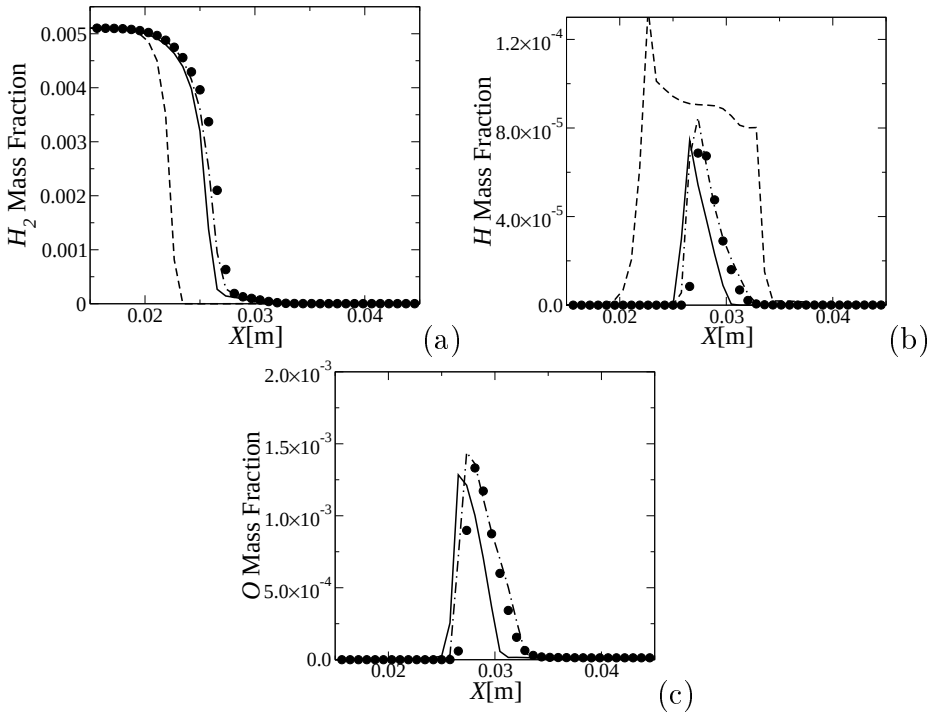

Figure 3.7: Comparison of the instantaneous species profiles obtained by the DI (•), the P-ANN (- - -), F-ANN (- . - .), and L-ANN (—), at $t = 5t^*$ for Case A2.

with an acceptable error, which is in consistency with our previous observations [4]. The L-ANN, on the other hand, is even better than F-ANN for this case, showing almost identical variation with DI.

The corresponding instantaneous results for species H_2, H and O at $t = 5t^*$ is shown in Figs. 3.7a-c for Case A2, respectively. The non-dimensional time (t^*) is calculated based on the maximum velocity induced by the initial coherent vortex and its size (u', D_C). At this instant, the results obtained by P-ANN is not following the same trend even for the major species H_2, and denotes an early consumption of the fuel (3.7a). This is supported by the fact that the peak value for H is reached at approximately 0.022, whereas DI results detect the peak at 0.028, as seen in Fig. reffig:Case2b. P-ANN results are not shown for O mass fraction in Fig. 3.7c, since it exhibits large amount of error compared to the other ANN models. Similar to Case A1, the F-ANN and L-ANN results are comparable with each other with an acceptable error. The L-ANN results seem to be slightly shifted towards the reactants for both of the minor species.

Case A3 shows the instantaneous species mass fraction profiles at $t = 5t^*$ for an equivalence ratio of 0.8, and a higher background turbulence intensity compared to Cases A1 and A2. The equivalence ratio is an indirect input to the F-ANN and L-ANN computations through the initial data profile used to run both 3D simulations and the stand-alone LEM. Hence, a different ANN is used for F-ANN and L-ANN in Case A3, than the previous cases, whereas P-ANN is not changed. Interestingly,

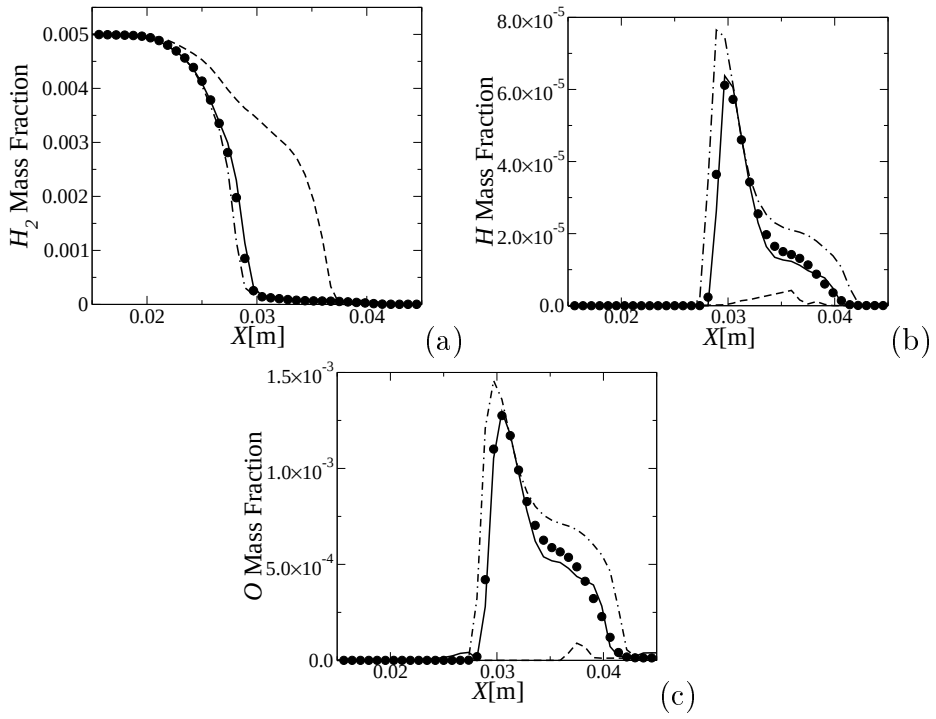

Figure 3.8: Comparison of the instantaneous species profiles obtained by the DI (•), the P-ANN (- - -), F-ANN (- . - .), and L-ANN (—), at $t = 5t^*$ for Case A3.

the P-ANN underpredicts the actual profiles of the minor species as seen in Figs. 3.8a-c at $t = 5t^*$ for Case A3. This indicates a non-complete combustion process, which is supported by the H_2 plot (Fig. 3.8a) as well. The H_2 mass fraction exists at locations where it should have been consumed as calculated by the DI. Results obtained by F-ANN is very accurate in capturing the variation of H_2, similar to the previous cases. The location of the reaction zone is also detected well, with a slight overprediction of the peak value of the mass fractions. The maximum deviation is 7 % for the O mass fraction. The L-ANN results for this case exhibit better agreement with the DI computations than the F-ANN.

Finally the instantaneous profiles for H_2, H and O species obtained at $t = 5t^*$ for Case A4 are given in Figs. 3.9a-c. This case is for the same initial turbulence quantities with Case A3, but, for $\Phi = 0.8$. Hence, the same ANN used for cases A1 and A2 is used for A4. The increase in initial turbulent intensity resulted in flame thickening compared to case A2, as seen in the plots. Similar to that was observed in A3, the P-ANN tends the underpredict the correct profiles, and is wrong for all species.

3.1.4 Case B - LEM studies of premixed methane/air flames

The LEM is initialized based on the solution obtained from a steady, laminar, one-dimensional premixed methane/air flame computation at an equivalence ratio of 0.6.

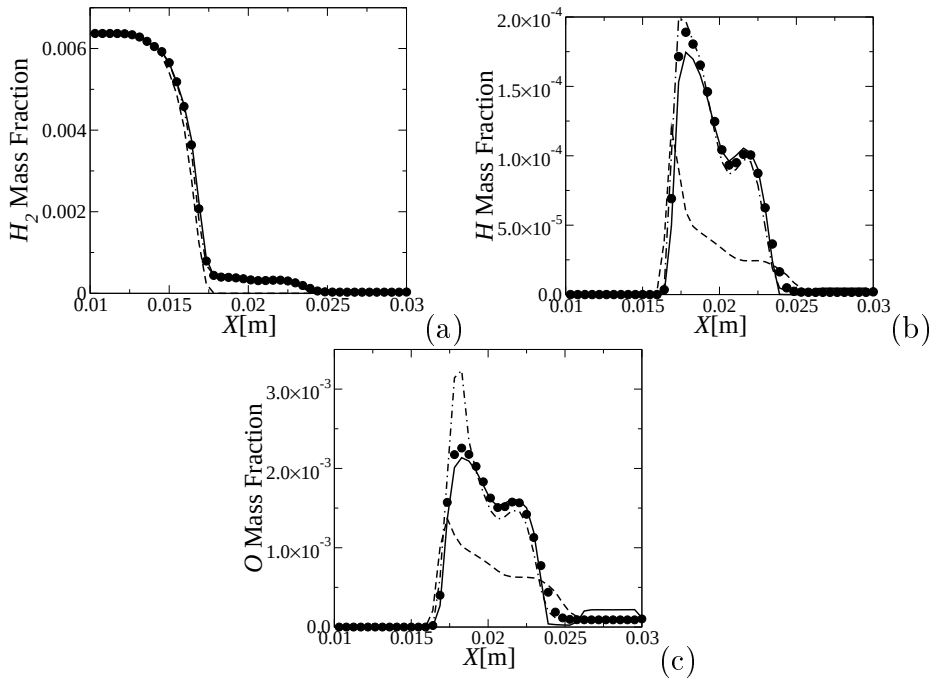

Figure 3.9: Comparison of the instantaneous species profiles obtained by the DI (•), the P-ANN (- - -), F-ANN (- . - .), and L-ANN (—), at $t = 5t^*$ for Case A4.

A 16-species, 12-step skeletal mechanism is employed for chemical kinetics calculations. A database is constructed for a range of Re_t with a fixed integral length scale L. The recent LES data on the SPRF combustor [1] reveals that the maximum value of Re_t is of the order of 400. Hence, the Re_t is varied from 10 (diffusion dominated) to 400 (turbulent stirring dominated). The thermo-chemical state-space is recorded at every five iterations, and later the instantaneous species reaction-rates are calculated and stored in a training table. The LEM computations are run for a number of iterations up to 1000 number of iterations (N^* =10). The optimum ANN architecture is found to be a three hidden layer architecture with ten, eight and four (10/8/4) number of PEs at each hidden layer.

The comparison of the LEM results for species CH_4, H_2O, and OH obtained by DI and ANN at Re_t =290 is shown in Figs. 3.10a-c at $N = 5N^*$. The integral length scale for this case is larger than the laminar flame thickness of the premixed flame. Hence, for the given turbulent Reynolds number, the flame front is distributed more effectively by turbulent stirrings than Case C, as it was shown in Fig. 3.2. The turbulent stirrings create multiple flame crossings at each instant, resulting in a thick turbulent flame brush. The agreement between the ANN and DI predictions is fairly good within the flame brush.

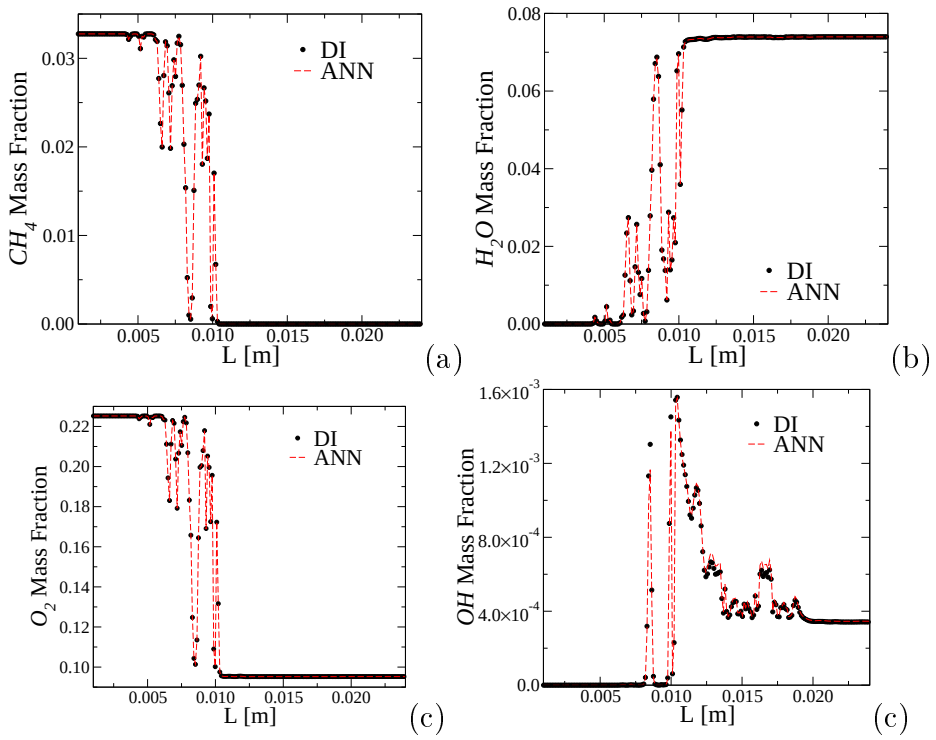

Figure 3.10: Instantaneous scalar profiles obtained for Re_t =290 and at $N_{iter} = 5N^*$. Case B.

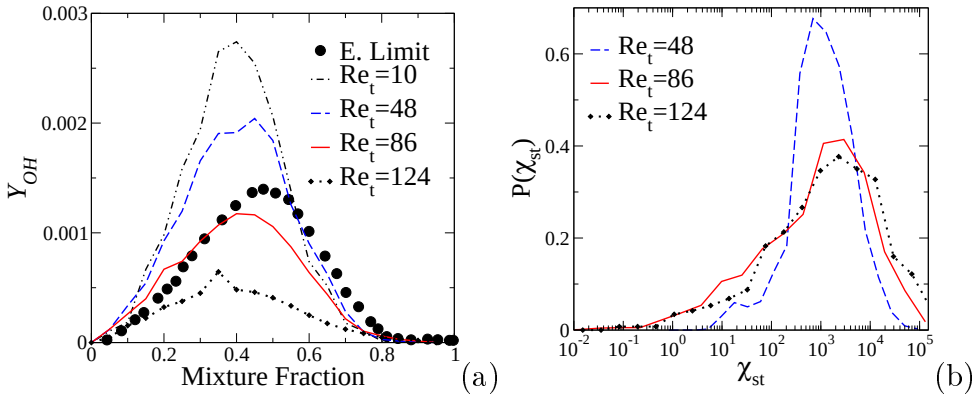

Figure 3.11: Conditional means of OH mass fraction and χ_{st} with respect to the mixture fraction for Case C.

3.1.5 Case C - LEM studies of non-premixed syngas/air flames

The initial scalar dissipation rate is selected to be χ=0.50χ_q, with χ_q denoting the extinction scalar dissipation rate (χ_q=2194s^{-1}). Here, stand-alone LEM computations are run for 2000 iterations (N_{iter} =2000) with a time step (Δt) size of 4.510^{-8} s (t_j = 20), at which, the DNS study reports considerable amount of local extinction occurs. Similar to the DNS study, the non-dimensional time (t_j) is calculated by

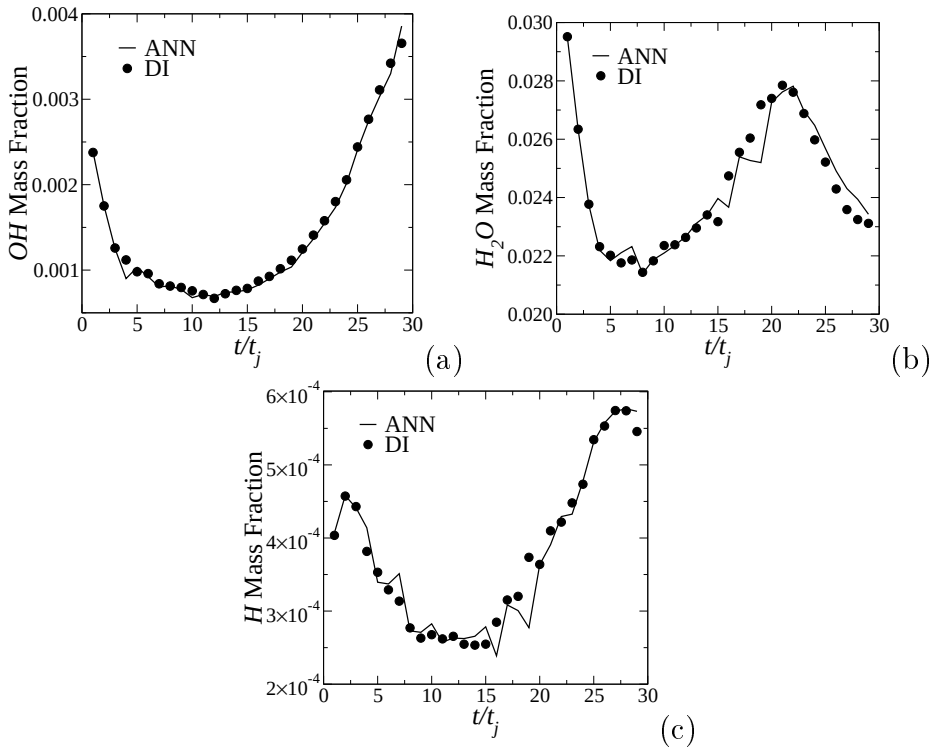

Figure 3.12: Time evolution of the scalar profiles for Re_t =80 at a location within the flame zone - Case C.

using the width of the fuel slab (H) and the characteristic jet velocity U [34]. Δt is selected in accordance with an LES study performed for the same case [3]. As noted earlier, the LEM is independent of Δt as stirring and diffusion proceeds with their own time step sizes.

The mean value of the PDF of OH mass fraction conditioned on the mixture fraction ($Y_{OH}|Z$) is shown in Fig. 3.11a for four different Re_t values at approximately $t = 20t_j$. The laminar flamelet value at extinction (extinction limit) [34] is also presented for comparison purposes. For a very low Re_t (i.e., Re_t =10), the initial profile remains almost unaffected by the turbulence, which is consistent with our previous observations. As the turbulent Reynolds number increases, the flame is pushed towards extinction and the LEM data agrees well laminar flamelet at approximately Re_t =86, denoting that LEM predicts extinction at this turbulent Reynolds number. As the Re_t is increased beyond 86, the LEM profiles demonstrate increased level of extinction. The PDF of the scalar dissipation rate at the stoichiometric mixture fraction $P(\chi_{st})$ is given in Fig. 3.11 (b) for the same conditions shown in Fig. 3.11 (a). Scalar dissipation rate is calculated as $\chi_{st} = 2D(\partial f/\partial s)(\partial f/\partial s)$, where f is the mixture fraction calculated by Bilger's definition and D is the mixture diffusivity calculated with a unity Lewis number assumption [34]. Here, it is seen that the tails of the PDF spreads-out as the Re_t is increased. Also, the mean value of $P(\chi_{st})$ shifts towards higher values of scalar dissipation rate as Re_t is increased, and is approximately 2300 s^{-1} for Re_t =86. The DNS study reports that the extinction scalar dissipation rate

is 2194 s^{-1}. The current LEM prediction is close to this value suggesting that some of the underlying physics has been captured in our LEM simulation.

In order to evaluate the generalization of the trained ANNs, the stand-alone LEM simulation is repeated, by using the trained ANN for the chemical-kinetics. It is observed that at $Re_t = 80$ the time variation of some of the key minor species mass fraction (OH, H_2O, H) obtained by using DI and ANN are in fair agreement. This is demonstrated in Figs. 3.12a-c at a location within the flame zone, where the reaction rates for the species are at their maximum value. Here, results at every 100 iterations are shown for both of the simulations. For t/t_j between 15 and 22 there is some discrepancy between the ANN and DI, although the error is less than 1 %. In order to understand

Table 3.5: Memory saving by ANN for Case A

	Look-up table size	ANN size
F-ANN	212.6 MB	0.107 MB
P-ANN	67.5 MB	0.107 MB
L-ANN	242.1 MB	0.107 MB

Table 3.6: Timing for Case B

	Time/(Step×Grid)
Stirring Only	5.66×10^{-5}
Diffusion Only (Le #)	4.52×10^{-4}
Diffusion Only (M.A.)	7.21×10^{-4}
Reaction Only	2.44×10^{-2} (7.02×10^{-4} with ANN)

Table 3.7: Timing for Case C

	Time/(Step×Grid)
Stirring Only	3.12×10^{-5}
Diffusion Only (Le #)	3.69×10^{-4}
Diffusion Only (M.A.)	7.22×10^{-4}
Reaction Only	2.35×10^{-3} (6.62×10^{-4} with ANN)

3.1.6 ANN speed-up and memory savings

The speed-up achieved by all ANNs considered for Case A is identical, and approximately 11X, since the same ANN architecture (10/5) is used for the LES cases. The memory saving is different for each distinct ANN method, since the training tables are different. As given in Table 3.5, there is considerable amount of memory saving achieved by using ANN. The tables used for training F-ANN and L-ANN have nearly the same size. The table used for P-ANN training is, however, much smaller by almost 3 times than the ones used for F-ANN and L-ANN. So, the poor performance of P-ANN could be attributed to using a smaller training table size. However, the $\Delta\Phi$

used for generating the table is already very small, and the number of grid points has been increased extensively. Thus, for the range of Φ considered in the LES, increasing the training table size of P-ANN would be only possible by including states, which are very similar to those already in the table, and is therefore redundant. These observations suggest that there is an inherent limitation of the P-ANN approach compared to the F-ANN and L-ANN.

The time required to perform stirring, diffusion and reaction computations per number iterations and grid points on an Intel PC (Pentium 4, 2.40 GHz) is given in Table 3.6 for Case B. The least time consuming process is the turbulent stirring, since it is handled in a stochastic manner. The time required to do diffusion calculation is approximately one order of magnitude larger than for stirrring. The diffusion cost is increased further by using mixture averaged (M.A.) diffusivities for the species equation compared to the constant Lewis number assumption. Regardless, the reaction rate calculation by using a stiff ODE solver is the most time consuming process, which is 430 times more expensive than stirring, and approximately 30 times larger than the diffusion. The time required to calculate reaction rates through ANN computations is, however, of the same order with the diffusion calculations, and therefore, results in approximately 35X speed-up for the chosen ANN.

Table 3.7 lists the time required to perform stirring, diffusion and reaction rate calculations in the LEM simulation for Case C. The most important difference between Case B and Case C timing comparison is the reaction rate calculations. For the methane skeletal mechanism used in Case B, the chemical source term computation was approximately 30 times slower than the diffusion. For the syngas case, however, it is only 7 times slower than diffusion. It is well known, the syngas reaction mechanism is not as stiff as methane, since syngas combustion is a sub-set of the larger methane combustion [9]. So, for this configuration and kinetics model, ANN is only 3.5 times faster than the DI. Regardless, there is still a speed-up in the computations. Finally, the ANN table used for training is 3.18 GB, whereas only 0.1 MB of memory is required to store the ANN coefficients used during the actual computation. Hence, there is considerable amount of memory saving, which is very beneficial for employing PC parallel clusters with limited memory. This result is expected to hold regardless of the mechanism itself.

3.2 ANN for Turbulent Non-premixed Combustion Modelling with LEMLES

3.2.1 Extinction and Reignition Studies

Here, the DNS study by Hawkes et al. involving a temporally evolving reacting turbulent jet [34] is revisited using LES. Due to the non-equilibirum aspects of this low Damkohler number based configuration, the problem gives an opportunity to investigate the physics of flame-turbulence interaction near extinction/reignition. Issues and features investigated in the original DNS study, are re-examined using the LES based approach. New properties (e.g., conditional statistics) from the DNS are extracted and compared to the LES predictions. The same kinetics as in [34] is employed for the LES, and the subgrid turbulence-chemistry interactions are accounted for by using the LEM model incorporating a subgrid resolution comparable with the DNS mesh. Dual benefits arise from solving the scalar equations in the subgrid and, in the form of CPU-savings in side-stepping the temproally constraining requirements of the stiff kinetics calculations. This, potentially, offer possibilities in studying the physics rich phenomenon of extinction-reignition [34, 37, 38] without the compuational demands imposed by a true DNS option [34]. Whether the accuracy of predictions using this approach relative to DNS is acceptable is discussed below. For these studies the L-ANN approach mentioned in Section 3.1.2.2, is used. In the following discussions, this approach will be referred to as ANN-LEMLES.

3.2.2 Numerical Setup and ANN Training

Three cases, "L", "M" and "H" representing low, medium and high Reynolds numbers were investigated in the original study ([34]). Here, the case M with a Reynolds number of 4478 and a Damkohler number of 0.011 is investigated using ANN-LEMLES. The DNS study showed that this case exhibits complex extinction and reignition during flow/flame interaction and evolution. The computational domain (L_x, L_y, L_z) is ($12H$, $14H$, $8H$), where H denotes the initial width of the jet velocity, and $H = 0.96$ mm for Case M. The DNS employs 64 grid points along H, which leads to approximately 350 M grid points in total, with a minimum resolution of around 2η.

Table 3.8: Test Case Specifics

	Δx [m]	Δy [m]	Δz [m]	Δs (LEM) [m]
Case M-1	1.2×10^{-4}	max. 2.50×10^{-4}	1.2×10^{-4}	max. 1.28×10^{-5}
		min. 0.70×10^{-4}		min. 0.84×10^{-5}
Case M-2	0.6×10^{-4}	max. 1.25×10^{-4}	0.6×10^{-4}	max. 0.64×10^{-5}
		min. 0.35×10^{-4}		min. 0.42×10^{-5}

Two LES results are presented here: Cases M-1 and M-2, as outlined in Table 3.8. Grids used for both of the cases are clustered in the shear layer with smooth stretching towards the transverse boundaries. For Case M-1, the minimum LES resolution in the shear layer is 5η, whereas, it is 2.5η for Case M-2. Thus, these resolution are similar to

the DNS. The grid resolution in the two periodic directions, however, is much larger than the DNS resolution as noted in Table 3.8. Overall, based on the resolution given in Table 3.8, Cases M-1 and M-2 are using approximately 700K (96×112×64) and 5.5M (192×224×128) grid points, respectively. 12 LEM cells are used within each LES cell to account for subgrid turbulence-chemistry interactions. With this grid, the subgrid resolution is reasonable to capture the small-scale flame-turbulence interaction.

The LES is initialized identical to the original DNS study with a laminar flamelet solution at a scalar dissipation rate χ =0.75χ_q. Here, χ_q is the extinction scalar dissipation rate, which is 2194 s^{-1}. The fuel is composed of 50 % CO, 10 % H_2 and 40 % N_2, whereas the oxidizer is air. Isotropic background turbulence is added to trigger the evolution of shear-generated turbulence. The initial turbulent integral length scale is $H/3$ and the turbulence intensity is $0.05U$. Characteristic perfectly non-reflecting outflow boundary conditions are used in the transverse direction, whereas in the streamwise and the spanwise directions periodicity condition is imposed. A 21 steps, 11 species ($H_2, O_2, O, OH, H_2O, H, HO_2, CO, CO_2, HCO, N_2$) reduced mechanism is used for the chemical kinetics calculations [34]. Mixture averaged transport properties are used for the calculation of heat and species diffusion fluxes.

The species instantaneous reaction rates in the subgrid is calculated by using the ANN approach as a function of the species mass fractions and the temperature: $\phi = (\dot{\omega}_1, \dot{\omega}_2, ..., \dot{\omega}_{Ns}) = ANN(Y_1, Y_2, ..., Y_{Ns}, T)$. The ANN is trained on an *unsteady* thermo-chemical database constructed through stand-alone LEM computations. An ANN architecture of 3 hidden layers with 5, 3 and 2 number of processing elements at each hidden layer is used for data training. The further details of the table generation by stand-alone LEM, ANN training and architecture selection relevant to the conditions considered here are discussed in another study [2], and will not be repeated here for the sake of brevity.

3.2.3 Extinction and reignition predictions

The mean value of the probability density function (PDF) of OH mass fraction conditioned on mixture fraction obtained at non-dimensional times t_j =20 and 40 by Cases M-1, M-2 and the DNS is shown in Figs. 3.13a-b, respectively. The time is non-dimensionalized by the reference time given as $t^* = H/U$, where H and U are the initial width of the fuel slab and the characteristic jet velocity, respectively [34]. The initial data at $t_j = 0$ used for all calculations, and the laminar flamelet value at extinction are also shown in the figures for comparison purpose. At $t_j = 20$, as shown in Fig 3.13a, the LES and DNS results starting from the initial profile drops below the extinction limit predicted by the laminar flamelet solution. Both LES results are very similar to each other at this time instant. They also predict values less than the DNS at almost every mixture fraction, indicating that the ANN-LEMLES predicts more extinction. At reignition (Fig 3.13b), however, all the profiles show increased level OH. Especially for mixture fraction values between 0.4 and 0.75, the OH mass fraction is greater than the extinction limit, clearly indicating a reignition process. The finer grid LES (Case M-2) predicts a solution that is closer to the DNS data.

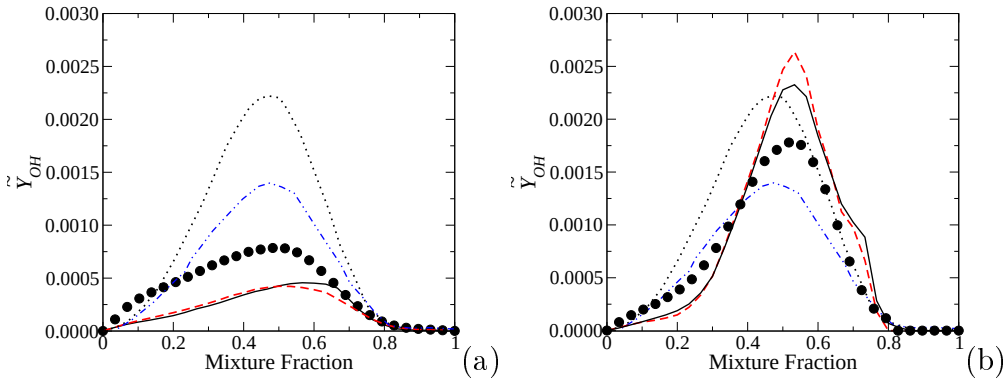

Figure 3.13: Comparison of the OH statistics obtained by the ANN-LEMLES and DNS at t_j = (a) 20 and (b) 40. (•) DNS, (- - -) Case M-1, (—) Case M-2, (...) initial data and (- . -) laminar flamelet value at extincion.

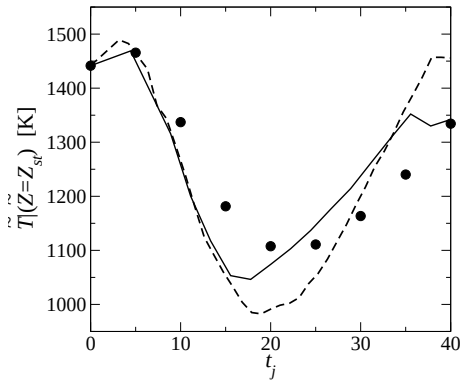

Figure 3.14: Variation of the mean temperature at the stoichiometric mixture fraction obtained by the DNS (•), Case M-1 (- - -) and Case M-2 (—).

Although there are differences, overall both LES predict extinction and reignition at approximately the same instant as in the DNS with relatively good agreement in the trends. As discussed below, other results also confirm the overall accuracy of the ANN-LEMLES approach.

The time variation of the mean value of PDF of temperature at the stoichiometric mixture fraction is shown in Fig. 3.14. The DNS data starts initially at 1450 K, and then decreases down to approximately 1100 K at $t_j = 20$. After this time instant, the temperature starts to build up again, indicating the reignition process, and finally reaches 1300 K, which is less than its initial value. Both ANN-LEMLES computations exhibit a similar variation. However there are some differences. Case M-1 prediction of the temperature at extinction is 1000 K, which is around 100 K less than the prediction in the DNS. On the other hand, the finer grid Case M-2 is closer to the DNS data, with very little discrepancy at t_j =20 and 40. Overall, the results obtained for Case M-2 show a consistent behavior for the entire simulation period, and therefore, the discussion below focus only on this case while doing more quantitative comparison

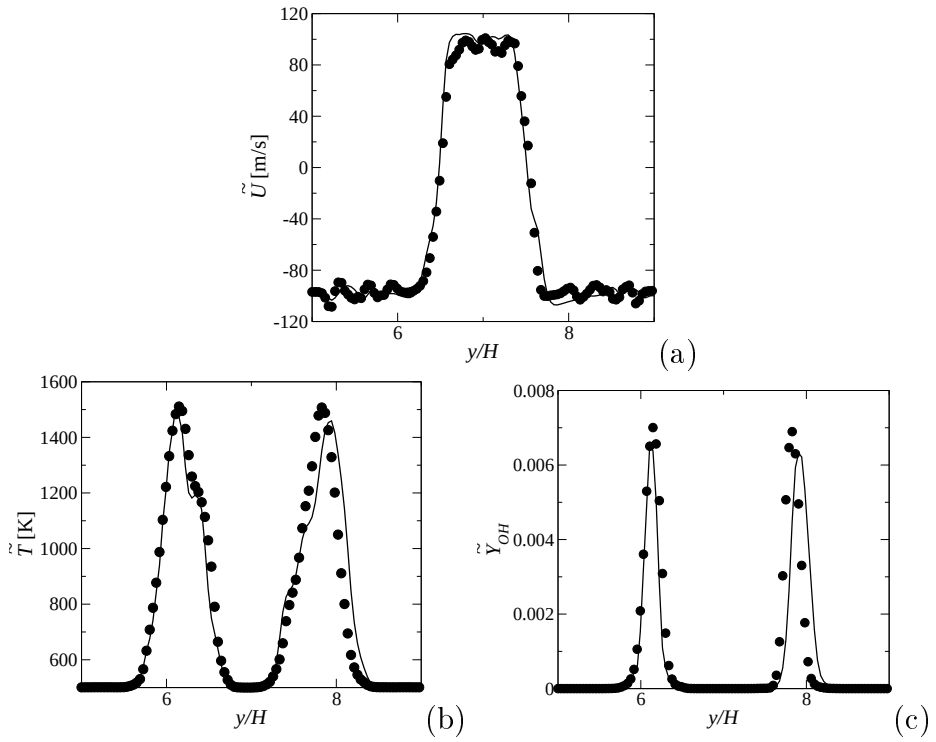

Figure 3.15: Comparison of the instantaneous data obtained by the Case M-2 LEMLES using DI (•) and ANN (—) at t_j=4.5.

with the DNS.

Figures 3.15a-c shows the ANN-LEMLES and LEMLES using DI (DI-LEMLES, hereafter) results obtained for Case M-2. Here, the axial velocity, the temperature and the OH mass fraction comparisons are presented. The figures show the instantaneous data obtained at t_j =4.5 at the mid-$x-y$ and $y-z$ planes. The accuracy of the ANN for this case is comparable to the DI. The maximum value of the temperature within the reaction zone is predicted well. Also, the thickness of the reaction zone, as predicted by temperature (Fig. 3.15b) and OH mass fraction (Fig. 3.15c) profiles indicates that the ANN is working reasonably well. There is a slight mismatch in the peak value of the OH mass fraction, between the ANN- and DI- LEMLES. This mismatch is also observed for the axial velocity in particular at $y/H \cong 7$. However, it should be noted that the results cannot be expected to match perfectly well, since they are extracted at two slightly different time instants. Regardless, the accuracy of the ANN-LEMLES is acceptable, and can be considered as representative for the actual DI-LEMLES. In the following, we primarily compare the ANN-LEMLES predictions against the DNS data in order to obtain a candid assessment of this approach. Some of this DNS data reported below are also new and have been extracted specifically to investigate both the physics and the ability of ANN-LEMLES to predict them.

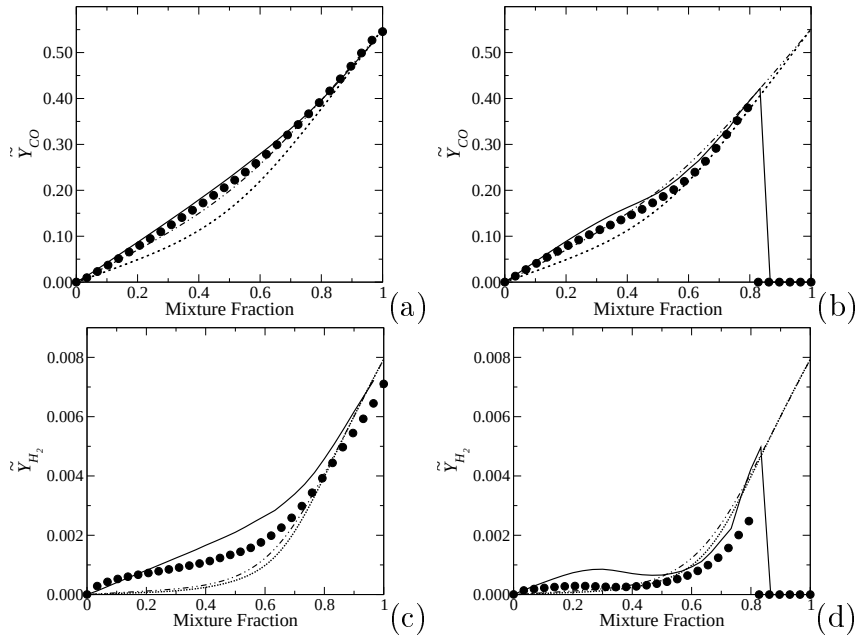

Figure 3.16: Conditional means of $\tilde{Y}_{CO}$ and $\tilde{Y}_{H_2}$ at extinction (a, c) and reignition (b, d) obtained by ANN-LEMLES and DNS. (•) DNS, (—) ANN-LEMLES, (...) initial data and (- . -) laminar flamelet value at extincion.

3.2.4 Scalar field conditional statistics

The mean value of the PDFs of H_2 and CO mass fraction conditioned on the mixture fraction at extinction ($t_j = 20$) and reignition ($t_j = 40$) are shown in Figs. 3.16a-d. The data used to initialize the LES and the laminar flamelet value at extinction are also shown in the figures. The DNS data shows that the conditional PDF of CO mass fraction varies almost linearly with respect to the mixture fraction at both $t_j = 20$ and $t_j = 40$, in Figs. 3.16a-b, respectively. The variation of the conditional PDF of H_2 mass fraction, on the other hand, exhibits different slopes with respect to the mixture fraction. Starting from the fuel stream ($Z = 1$), the PDF of H_2 mass fraction decreases with a much steeper slope than the CO (Fig. 3.16c). This is a direct result of an early H_2 consumption within the fuel stream, which release H and OH radical species that play a key role in speeding up CO oxidation [39]. Then, between $Z = 0.2$ and 0.6, the H_2 consumption speed decreases and the variation of the conditional statistics exhibits a relatively flat distribution, which is a result of the H_2 recombination reactions occurring within this range. At $t_j = 40$, Figs 3.16b-d show negligible CO and H_2 for $Z > 0.8$ indicating that the fuel is all consumed by this time due to the reignition.

The means of the conditional PDFs obtained by ANN-LEMLES are given in Figs. 3.16a-d. The ANN predictions at both extinction and reigntion for the CO statistics matches perfectly well with the DNS data as shown in 3.16a-b. For H_2 statistics, the profiles obtained by the ANN seem to capture the same trend as the DNS. Fig. 3.16c shows that the slope at $0.2 < Z < 0.6$ is somewhat larger than the DNS prediction.

Also, at $t_j = 40$, as given in Fig. 3.16d, the value of H_2 at $Z = 0.8$ is higher than the DNS value. This indicates that the H_2 consumption is predicted slightly off especially on the fuel rich side.

The mean value of the PDF of CO_2 mass fraction at $t_j = 20$ and $t_j = 40$ are compared in Figs. 3.17a-b. Similar to the OH mass fraction (as given in Fig. 3.13a), the conditional CO_2 mass fraction exhibits smaller values than the laminar flamelet value at extinction. This feature can also be seen in Fig. 3.17 (c), where the mean of the PDF of H mass fraction conditioned on the mixture fraction is given at $t_j = 20$. All of these figures (Figs. 3.13a, 3.17a and 3.17c) indicate that the decrease in the conditional species mass fractions is not specific for only one species (i.e., OH), but is actually a general trend for all the species, except for the ones in the fuel mixture (CO and H_2). For both CO_2 and H, the ANN-LEMLES results follow the same trend as the DNS even though the former approach slightly underpredicts the DNS data in the range of $0.4 < Z < 0.8$. Interestingly, the error is less than that is observed for the OH mass fraction.

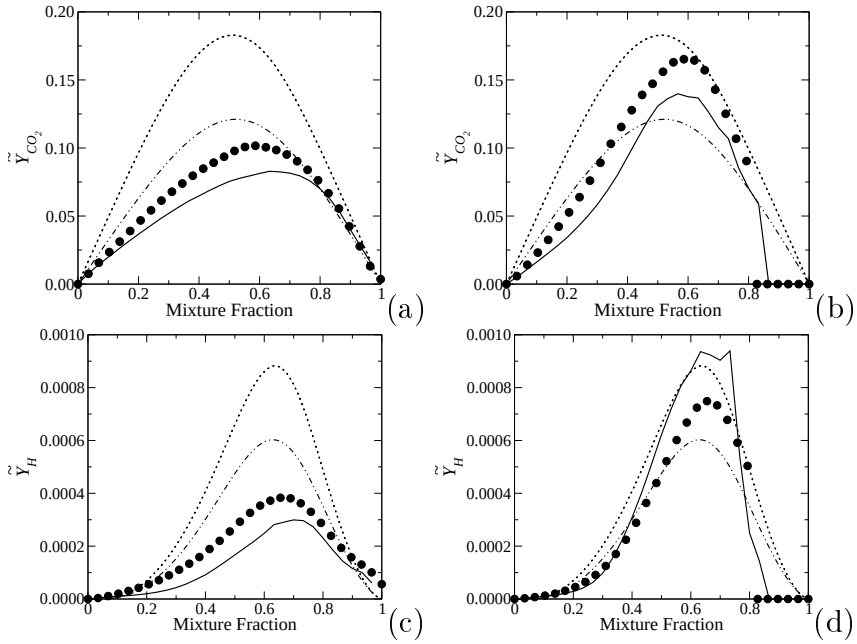

Figure 3.17: Conditional means of the $\tilde{Y}_{CO_2}$ and $\tilde{Y}_H$ at extinction (a, c) and reignition (b, d) obtained by ANN-LEMLES and DNS. (•) DNS, (—) ANN-LEMLES, (...) initial data and (- . -) laminar flamelet value at extincion.

At reignition ($t_j = 40$) in Fig. 3.17b, the mean of the PDF of CO_2 mass fraction conditioned on the mixture fraction shows an increased level compared to the value at $t_j = 20$. The values at $t_j = 40$ for both species (CO_2 and H) and temperature are above the laminar flamelet values at extinction indicating reignition, consistent with the OH data shown in Fig. 3.13b. The CO_2 is slightly underpredicted, whereas the H value is larger (Fig. 3.17d). However, the overall prediction of all species are reasonable using the ANN-LEMLES approach.

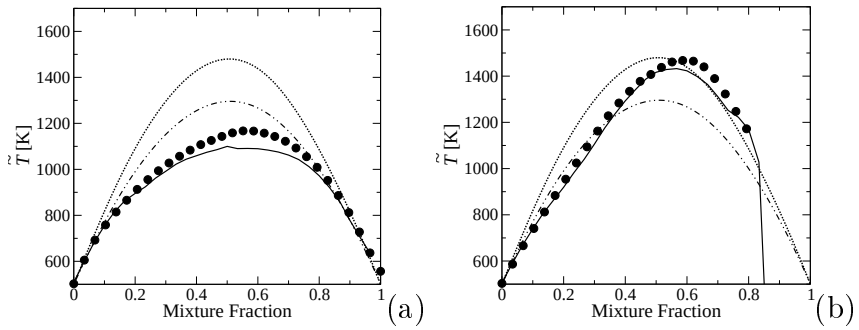

Figure 3.18: Conditional mean of the temperature at extinction (a) and reignition (b) obtained by ANN-LEMLES and DNS. (•) DNS, (—) ANN-LEMLES, (...) initial data and (- . -) laminar flamelet value at extincion.

The variation of the mean value of the PDF of temperature conditioned on the mixture fraction at $t_j = 20$ is shown in Fig. 3.18a. The maximum value of temperature at the stoichiometric surface at this time is approximately 1100 K, which is almost 300 K less than its initial value. At reignition (Fig. 3.18b), the temperature recovers its initial value. The agreement between ANN-LEMLES and DNS is really good for the conditional PDF of the temperature indicating the accuracy of the current ANN methodology.

The stoichiometric mixture fraction (Z_{st}) based on Bilger's definition is approximately 0.43 for the current case. The stoichiometry refers to a perfect combustion where all the fuel is burned. Hence, typically, the scalar PDFs conditioned on the mixture fraction for temperature and the intermediate species peak at the stoichiometric mixture fraction value [40]. For this particular study, however, it is interesting to note that both the DNS and ANN-LEMLES extracted PDFs exhibit the maximum temperature not at the stoichiometric value but at a slightly fuel rich side. The CO_2 mass fraction and temperature peaks at approximately $Z = 0.6$ as seen in Figs. 3.17a-e. The H mass fraction, on the other hand, peaks at $Z = 0.7$. At reignition, the peak of the PDFs are shifted towards the fuel rich side further. The main reason behind these observations is that the mixture fraction inherently assumes that the both fuel and oxidizer have the same diffusion velocity. This is not correct for syngas flames, where the fuel mixture is composed of a relatively light (H_2) and heavy species (CO) that have different diffusion velocities. Hence, the results indicate that the mixture fraction formulation may not be an accurate modeling approach for syngas flames to parameterize thermochemical state-space in the LES applications. This is an issue that is being further investigated.

The evolution of the PDF of temperature at the stoichiometric mixture fraction is shown in Fig. 3.19. The PDF at $t_j = 10$ exhibits a narrow distribution, with a most probable state residing at 1300 K. This value decreases to 1000 K at $t_j = 20$. The probability of temperatures less than 1000 K also increases substantially compared to $t_j = 10$. This leads to a wider PDF, and the probability of the most probable state decreases from 0.03 to 0.02 at $t_j = 20$. The PDF at later instants shifts towards

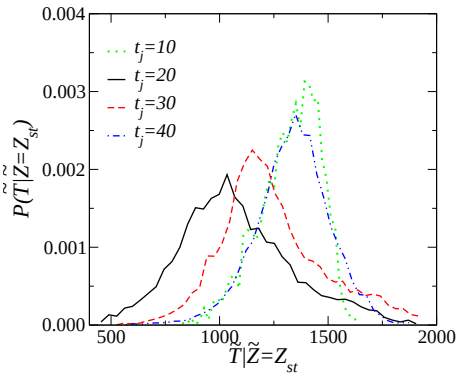

Figure 3.19: The time variation of the PDF of temperature at the stoichiometric surface obtained by the ANN-LEMLES.

higher temperature values, denoting a most probable state of 1100 K and 1400 K at $t_j = 30$ and $t_j = 40$, respectively. These results indicate that the PDFs at reignition and fully burnt states are much narrower than the one at extinction.

3.2.5 Syngas flame structure

The surface plots of CO and H_2 mass fraction at $t_j = 20$ and $t_j = 40$ are shown in Figs. 3.20a-d. The stoichiometric mixture fraction ($Z_{st} = 0.43$) is also shown in these figures. The mass fractions of both species show that from $t_j = 20$ ((a) and (c)) to $t_j = 40$ ((b) and (d)) the flame front is distributed over a finite region. Both CO and H_2 mass fractions decrease at $t_j = 40$ indicating consumption of the fuel. As seen in Figs. 3.20a-c, the stoichiometric mixture fraction at $t_j = 20$ looks like a boundary, after which both CO and H_2 cease to exist. At $t_j = 40$, however, the CO and H_2 mass fraction is spread over a much wider surface and the stoichiometric mixture fraction resides within this region.

Another interesting observation in Fig. 3.20a, at $t_j = 20$, is that the CO mass fraction is spread almost homogeneously, and its peak value is not changing much up to the stoichiometric mixture fraction. The H_2 mass fraction, on the other hand, exhibits peak values in pockets concentrated at the center part of the computational domain. Evidently, the H_2 is mostly consumed within the fuel stream, in contrast to CO, which is consumed at the stoichiometric surface. Similar to the earlier computational studies of the syngas flames [41], the current observations suggest that the syngas flames exhibit two reaction zones: A H_2 reaction zone, which is followed by CO combustion. This is also consistent with our previous observations based on the conditional mean PDFs (i.e., Figs. 3.16a-c).

In CO oxidation the main chain branching reaction is the $CO+OH \rightleftharpoons CO_2+H$ step [42]. Hence, OH is a key species, which determines the oxidation rate of the CO in syngas combustion. The OH surface plots obtained by using the current ANN-LEMLES approach at $t_j = 20$ and $t_j = 40$ are given in Figs. 3.21a-b, respectively. In Fig. 3.21a, the OH mass fraction peaks at the fuel rich side of the stoichiometric

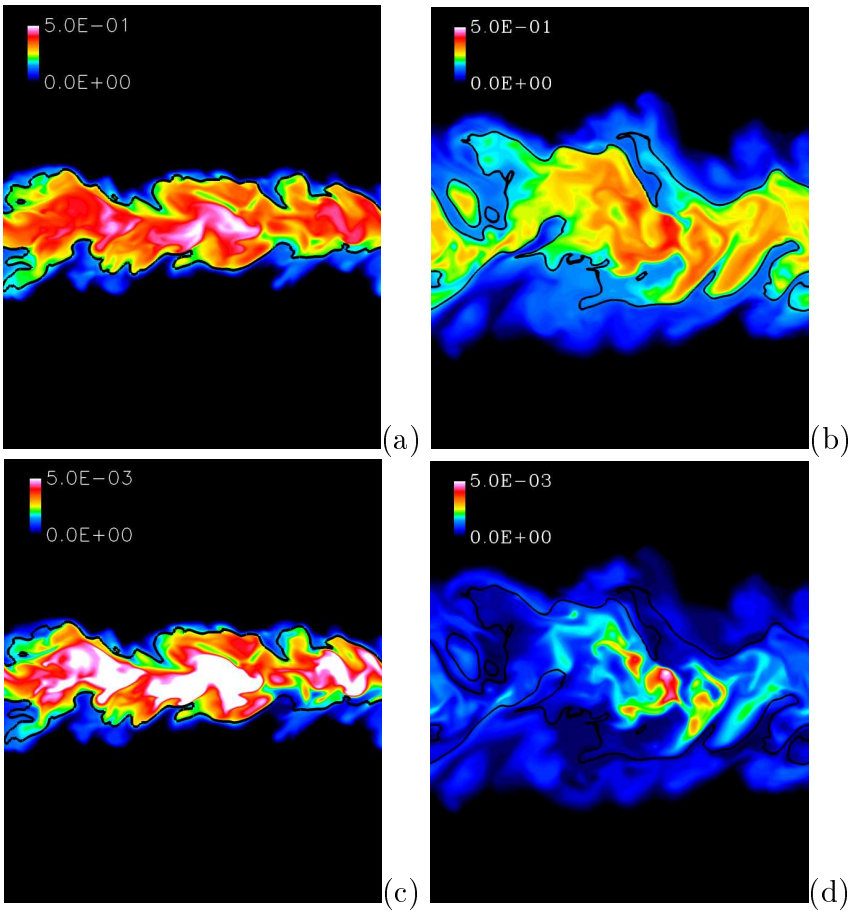

Figure 3.20: Instantaneous surface plot of $\tilde{Y}_{CO}$ ((a)-(b)) and $\tilde{Y}_{H_2}$ ((c)-(d)) mass fraction at $t_j = 20$ ((a)-(c)) and $t_j = 40$ ((b)-(d)) obtained by ANN-LEMLES.

surface. Comparing with H_2 surface plot shows that the OH is produced roughly around the H_2 pockets. Then, OH (and CO) is consumed through the chain branching reaction, and hence it vanishes near the stoichiometric surface. The OH mass fraction at $t_j = 40$ (Fig. 3.20c) is not spread as much as the fuel mixture (CO and H_2) on the fuel lean side of the stoichiometric surface. There exists localized pocket-like structures with high OH content. This observation suggests that at this time instant the H_2 is mostly consumed by chemical reactions, which leads to the formation of excessive amount of OH. This is also the reason for the decreased amount of H_2 within the center part of the shear layers, as seen in Fig. 3.20d.

The OH mass fraction surface plots obtained from the DNS study are shown in Figs. 3.21c-d for $t_j = 20$ and 40, respectively. The DNS and ANN-LEMLES results are overall, in good agreement. At $t_j = 20$, as seen in Fig. 3.21c, the DNS OH mass fraction peaks along the shear layer. At this time instant the OH contours are broken indicating local extinction process. This is followed by re-ignition at $t_j = 40$ within localized pocket-like structures. The overall characteristics of the are qualitatively smaller in both studies.

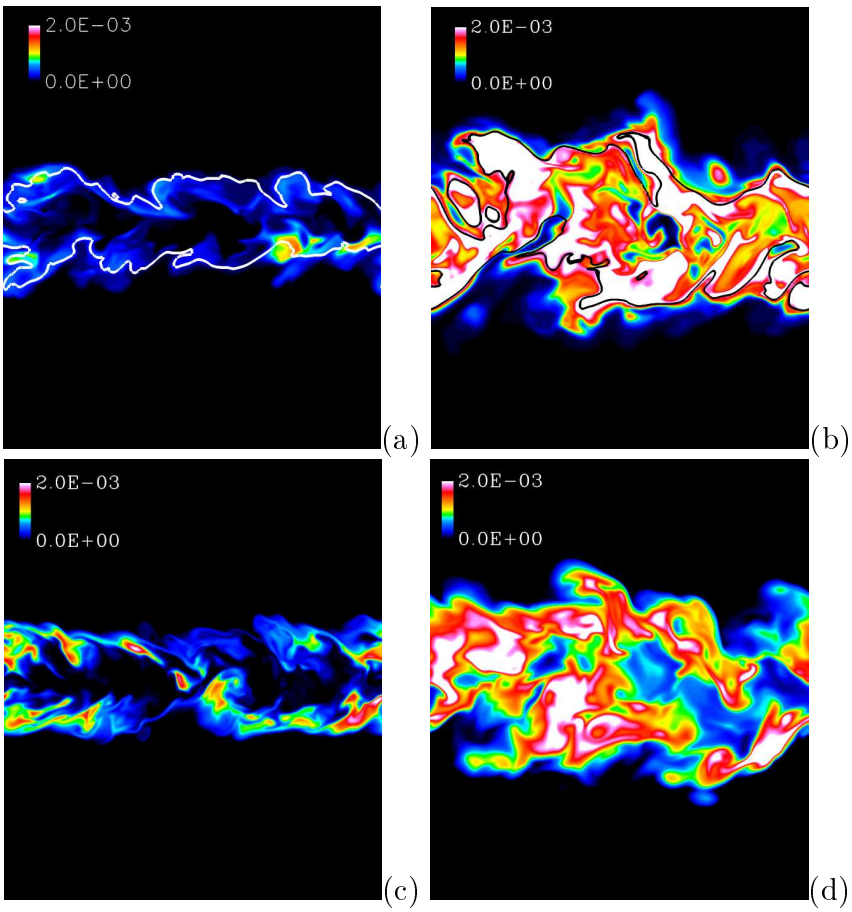

Figure 3.21: Instantaneous surface plot of $\tilde{Y}_{OH}$ at (a) $t_j = 20$, (b) $t_j = 40$ obtained by the ANN-LEMLES and at (c) $t_j = 20$, (d) $t_j = 40$ obtained by the DNS.

The DNS study at this time instant indicates that the shear layer is not wrinkled extensively by the large scale vortices as the ANN-LEMLES results show. However, it should be noted that discrepancies between the computations are expected, but the overall physics are seem to be captured well.

The surface plot of HO_2 radical species mass fraction at $t_j = 20$ and $t_j = 40$ is shown in Figs. 3.22a-b, respectively. Unlike OH, the HO_2 species is mostly concentrated on the fuel-rich side of the stoichiometric surface at both $t_j = 20$ and $t_j = 40$ as seen in the figures. Interestingly, the HO_2 mass fraction seems to be almost unaffected by the extinction process. In contrast to the rest of the species, the HO_2 exhibits a continuous and thin layer along the stoichiometric surface. At reignition (Fig. 3.22b), the HO_2 layer is thicker than at extinction, $t_j = 20$. The maximum HO_2 mass fraction value at reignition is only slightly larger than what is observed at extinction. Here, it should be noted that, although the peak value is larger at reignition, it can only be observed on a local sense. The HO_2 mass fraction at extinction on the overall is higher than that is for reignition. This indicates that at extinction the HO_2 exhibits a radical pool, whereas OH is decreasing. This result needs to be

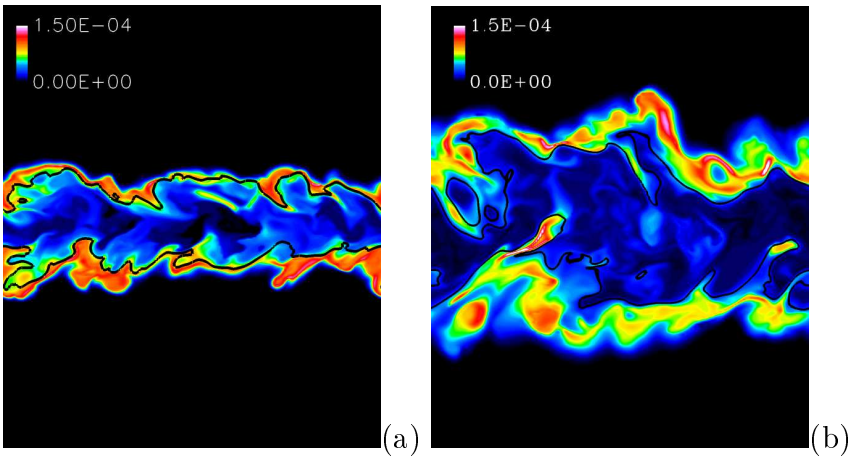

(a) (b)

Figure 3.22: Instantaneous surface plot of $\tilde{Y}_{HO_2}$ at (a) $t_j = 20$ and (b) $t_j = 40$ obtained by ANN-LEMLES.

studied further to come up with any concrete conclusion and is the subject of a future work.

3.2.6 Scalar dissipation rate statistics

Figures 3.23a-b shows the surface plot of the logarithm of normalized scalar dissipation rate ($log10(\tilde{\chi}/\chi_q)$) at $t_j = 20$ and $t_j = 40$, respectively. At extinction (Fig. 3.23a), the scalar dissipation rate is mostly concentrated around the stoichiometric surface. The variation clearly follows the stoichiometric line, since the gradient term ($\bigtriangledown Z$) attains its maximum value across the stoichiometric surface. At reignition (Fig. 3.23b), $\tilde{\chi}$ seems to be more distributed over the computational domain in the form of thin sheets. Here, it should be noted that the maximum value of the $\tilde{\chi}$ is almost similar to that obtained at extinction. Also, the sheets of $\tilde{\chi}$ cover a much wider region in the computational domain, which suggests that based on the $\tilde{\chi}$ information, same level of extinction should be expected at this instant similar to $t_j = 20$. This issue will be further discussed below.

The normalized PDF of the $log_{10}\chi$ at the stoichiometric mixture fraction is given in Fig. 3.24 at an intermediate time $t_j = 30$. The figure shows the PDFs obtained by the DNS study and the current ANN-LEMLES along with the log-normal distribution. Here, the scalar dissipation rate obtained by the ANN-LEMLES is the filtered value ($\tilde{\chi}$), whereas raw data is shown for the DNS (χ). The PDF extracted through ANN-LEMLES computation follows the same trend calculated by DNS. There are some minor discrepancies especially for the values of the normalized χ_{st} less than -3. ($(log_{10}\chi_{st} - \mu_{st})/\sigma_{\chi_{st}} < -3$). The ANN-LEMLES PDF tends to overpredict the DNS PDF in this range. Both DNS and ANN-LEMLES PDFs exhibit a negative skewness with a log-normal distribution, which is consistent with earlier studies [43]. The results indicate that the DNS PDF can be predicted well by the LEMLES (since it does not carry out any assumption regarding the shape of the PDF). This is a

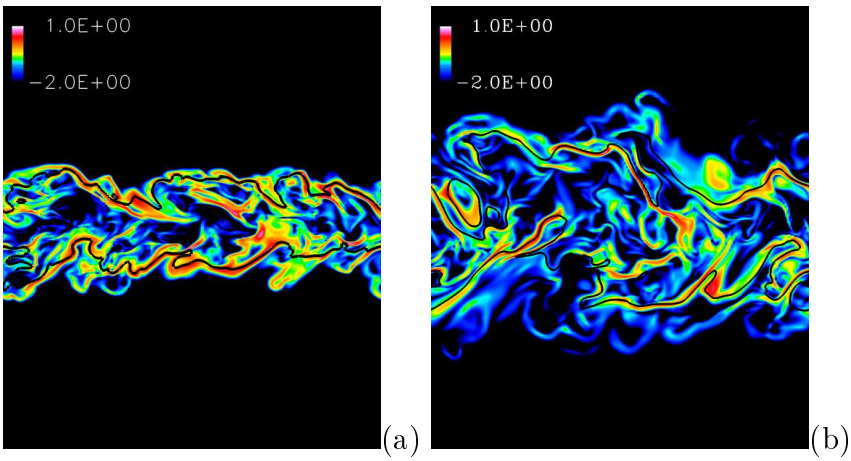

(a) (b)

Figure 3.23: Surface plot of $log_{10}(\tilde{\chi}_{st}/\chi_q)$ at (a) $t_j = 20$ and (b) $t_j = 40$ obtained by ANN-LEMLES.

unique ability of the LEMLES (with DI or ANN). The log-normal distribution tends to overpredict the correct PDF at higher and underpredict at lower values of χ_{st}, respectively for this case. The log-normal distribution is used in flamelet approaches to model the PDF of the χ_{st} [37, 5]. Both the DNS and ANN-LEMLES data show that the correct PDF differs from this shape at high and small values of χ_{st}. These results point to a possible modified model for the flamelet approach and needs to be explored further.

The normalized PDF of the scalar dissipation rate at $t_j = 20$ and $t_j = 40$ obtained by the ANN-LEMLES is given in Figs. 3.25a-b. The scalar dissipation rate is typically calculated based on the mixture fraction [5]. However, each species have their own scalar dissipation rates as well, and Figs. 3.25a-b show these PDFs calculated at different times of evolution. Here, in addition to the scalar dissipation rate calculated based on the mixture fraction ($\tilde{\chi}$), the CO ($\tilde{\chi}_{CO} = 2D_{CO}\nabla\tilde{Y}_{CO}.\nabla\tilde{Y}_{CO}$) and the OH ($\tilde{\chi}_{OH} = 2D_{OH}\nabla\tilde{Y}_{OH}.\nabla\tilde{Y}_{OH}$) scalar dissipation rates are also shown along with the log-normal distribution. For comparison purposes, all the PDFs are normalized as before (Fig. 3.24). As seen in Fig. 3.25a, at $t_j = 20$ all PDFs follow the log-normal distribution. As seen in Fig. 3.25a, the computed PDFs attain lower values than the log-normal distribution at dissipation rate greater than 2. The PDFs obtained at reignition are given in Fig. 3.25b. Here, the discrepancy between the model and computed PDFs decreases at higher values of the scalar dissipation rate. The PDF of $\tilde{\chi}$ and $\tilde{\chi}_{CO}$ are indistinguishable from each other, and the log-normal distribution seems to be a proper function for modeling purposes. The PDF of $\tilde{\chi}_{OH}$ at lower values of the scalar dissipation rate tends to overpredict the log-normal distribution. It should be noted that this is not very important for the overall flow physics, since the model deviates more at very small values of the scalar dissipation rate.

Figures 3.26a-c show the PDFs of $\tilde{\chi}$, $\tilde{\chi}_{CO}$ and $\tilde{\chi}_{OH}$ at the stoichiometric surface at different times. The scalar dissipation rate at the stoichiometric surface is an important quantity in modeling flame-turbulence interactions in LES [5], since it

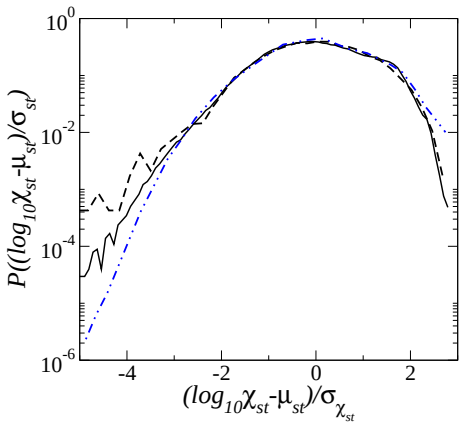

Figure 3.24: PDF of normalized logarithm of scalar dissipation rate at the stoichiometric mixture fraction at $t_j = 30$. (—) DNS, (- - -) ANN-LEMLES, (-..-..-) log-normal distribution

directly provides time scale information on the most reactive portion of the flame. A high $\tilde{\chi}$ at the stoichiometric surface leads to extinction, since local time scales are very short and the reactions cannot generate required amount of heat release [44]. The variation of $\tilde{\chi}$ at $Z = Z_{st}$ as given in Fig. 3.26 (a), however, shows interesting results. Similar to the PDF of temperature, given in Fig. 3.19, the PDF of $\tilde{\chi}$ at $t_j = 10$ exhibits a narrow distribution, with its most probable state located at roughly 0.8. This indicates that at this time scalar dissipation rate acting on the flame is almost as high as the critical scalar dissipation rate obtained at extinction by the flamelets. At $t_j = 20$, the most probable state shifts towards lower values of $\tilde{\chi}$ compared to $t_j = 10$. Also, the tail of the PDF extends barely to 1, which indicates that the time scale at the stoichiometric surface is large enough for reactions to occur. However, as it was discussed in details previously, at $t_j = 20$ the flame goes through an extinction process. For $t_j = 30$ and 40, $\tilde{\chi}$ decreases slightly and exhibits a similar shape.

The time variation of the PDF of $\tilde{\chi}_{CO}$ at the stoichiometric surface is shown in Fig. 3.26b. Both $\tilde{\chi}_{CO}$ and $\tilde{\chi}$ shows almost exactly the same variation. It starts from a narrow PDF and at extinction decreases to more wider distribution. After this point, the shape of the PDF does not show any change, but it rather shifts towards smaller value of $\tilde{\chi}_{CO}$. The PDF of $\tilde{\chi}_{OH}$, on the other hand, is the only one that shows a change with respect to time. At the initial stage ($t_j = 10$) and at reignition ($t_j = 40$), the PDF of $\tilde{\chi}_{OH}$ shows a narrow and negatively skewed distribution. For both of the time instants, the $\tilde{\chi}_{OH}$ obtains a value of -1, with the probabilities of 0.8 and 0.6, respectively. The shape of the PDF at $t_j = 20$ and $t_j = 30$ is more like Gaussian.

3.2.7 Time and memory savings

Each state obtained from the stand alone LEM computations is used as an entry in the thermo-chemical database used to train the ANN. The final training table includes approximately 600K states and its size is 3.18 GB. The ANN trained on this

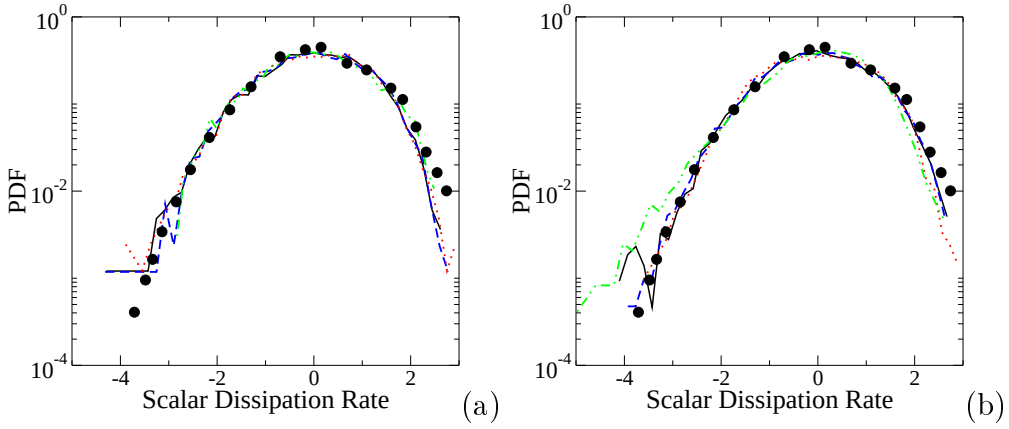

Figure 3.25: PDFs of normalized logarithm of scalar dissipation rate at the stoichiometric mixture fraction at (a) $t_j = 20$ and (b) $t_j = 40$ obtained by ANN-LEMLES. (•) log-normal distribution, (—) $\tilde{\chi}$, (- - -) $\tilde{\chi}_{CO}$, (-..-..) $\tilde{\chi}_{OH}$.

table stores the data through its weight coefficients, which requires a memory of only 0.1 MB. These coefficients are used by the LES solver to calculate the instantaneous species reaction rates for the subgrid scalar field computations. Hence, a considerable reduction in memory requirement is achieved by using ANN.

Table 3.9: Comparison of Speed-up Obtained by Different Models

	Species Equation	Time/(step×cell)	Speed-Up
ANN-LEMLES	LEM level (12 cells/LES)	1.29×10^{-2}	5.5
DI-LEMLES	LEM level (12 cells/LES)	7.10×10^{-2}	1.0

The computational time required to run a single iteration per grid points on a single processor INTEL PC (3.2 GHz Xeon) by ANN-LEMLES and DI-LEMLES is given in Table 3.9. The current ANN approach provides 5.5 times speed-up compared to the DI with a reasonable accuracy. It should be noted that the ANN speed-up is directly related with the stiffness of the reduced mechanism. For a much stiffer syngas mechanism, the speed-up is 11 as reported earlier [2].

3.2.8 Conclusions

The applicability of ANN as an interpolation and data storage scheme for multi-step finite-rate kinetics within the LES framework is addressed in this study. The ANN is used as a chemistry subgrid model for a non-premixed flame previously studied using DNS [34]. The thermo-chemical tabulation is achieved by using stand-alone LEM computations of the relevant composition (but not the actual geometry) as reported earlier [2]. In this approach, the species reaction rates are tabulated with respect to the thermodynamic state vector without any reduction in the number of input parameters and are later used for the ANN training. Once trained, ANN provided the instantaneous species reaction rates ($\dot{\omega}_i = ANN(Y_k, T)$).

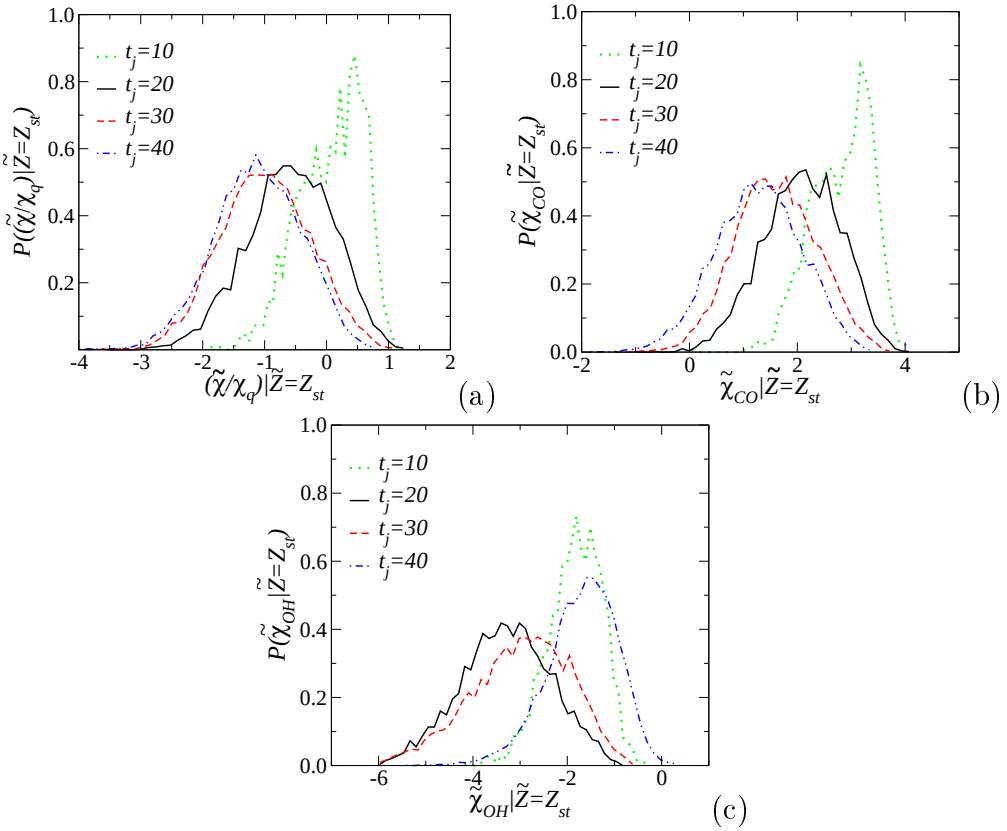

Figure 3.26: The time variation of the PDF of $\tilde{\chi}$, $\tilde{\chi}_{CO}$, $\tilde{\chi}_{OH}$ at the stoichiometric surface obtained by the ANN-LEMLES.

The ANN-LEMLES results on two separate grids (Cases M-1 and M-2) are compared with the DNS data. The results indicate that the current ANN-LEMLES captures both the extinction and the reignition physics with reasonable accuracy. The finer grid (Case M-2) provides slightly better results, as expected, but both cases show consistent results.

The ANN-LEMLES approach is investigated further by extracting additional data from the previous DNS study [34] for the species conditional statistics. The statistics obtained for the fuel components H_2 and CO show that they exhibit different characteristics due to their distinct diffusion and reaction characteristics. The conditional mean of H_2 drops much faster than the CO with respect to the mixture fraction, indicating an earlier H_2 consumption within the flame zone. Similar to the OH statistics, CO_2, H and temperature conditional means exhibit values less than the laminar flamelet value at $t_j = 20$, which is followed by an increase at $t_j = 40$. Direct comparison of the conditional statistics with DNS data shows that local extinction and reignition processes can be detected with reasonable accuracy using the ANN-LEMLES and at a substantially lower cost than the DNS.

The current ANN-LEMLES results are used to calculate the PDF of the normalized χ at the stoichiometric surface. The PDFs obtained by both the DNS and

the current LES exhibit a log-normal distribution with a negative skewness, which is consistent with theory. The PDF obtained by the ANN-LEMLES deviates slightly from the DNS PDF at the high and low end of the normalized values of the χ_{st}. Interestingly, the χ surface plot obtained by the ANN-LEMLES shows that the level of χ is actually almost similar at both extinction and reignition. The PDF of the scalar dissipation rate calculated based on the mixture fraction and CO mass fraction also supports the same observation. The dissipation rate calculated based on the OH mass fraction, however, is found to be more sensitive to extinction and reignition. This may suggest that perhaps dissipation rate calculated by OH mass fraction would be a better parameterization of the compositional state-space for future studies. This is outside the scope of this study and is an issue being looked at for a future study.

The ANN approach used in the current study provides a 5.5 times speed-up compared to the DI. The memory savings were also considerable. The size of the table used for ANN training is 3.18 GB, whereas ANN required only 0.1 MB of memory to store this data. It is noted that the ANN speed-up is strongly affected by the stiffness of the reaction mechanism used in the computations.

3.3 TANN based Filtered Reaction Rate Closure for LES

The ANN-LEMLES presented in Section 3.2 was shown to reproduce the results from the corresponding DNS study [34] satisfactorily. Computational savings arising from avoiding the solution of the stiff kinetics mechanism online [2] were shown to be significant. In this section, a new model is presented wherein the filtered reaction rates are obtained directly from a net created from modified ANN training strategy. The filtered reaction rates are directly used in the LES species transport equations in a strategy to be henceforth referred to as Turbulent ANN-LES (TANN-LES). Naturally, TANN-LES is expected to yield further computational savings over the relatively expensive subgrid simulation approach of ANN-LEMLES. To evaluate the accuracy aspects of this new model, the configuration investigated in the previous Section 3.2 is re-examined. Analyses and comparisons performed in the previous section are repeated to assess predictive capabilities of extinction and reignition [34, 2] for the new model. Additionally, it is shown that the TANN-LES using TANN generated for a large range of Re_t is capable of capturing the extinction-reignition physics with a very little loss of accuracy compared to the TANN-LES using TANN generated for the specific test case.

3.3.1 ANN based Chemical Kinetics Model

As in Section 3.2, a 21-steps 11-species syngas-air reduced kinetics mechanism based on Arrhenius model is used [34] for training the Artificial Neural Networks. The species retained are: $(H_2, O_2, O, OH, H_2O, H, HO_2, CO, CO_2, HCO, N_2)$. As explained previously, the instantaneous reaction rate is given by the Arrhenius model as:

$$\frac{dY_k}{dt} = F_k(Y_1, Y_2, ..., Y_{Ns}, T, P) = \omega_k \tag{3.2}$$

The $\overline{\dot{\omega}_k}$ needs to be determined for both LEMLES and LES simulations. To reduce the cost of chemical kinetics ANN instead of stiff ODE solver is employed. For ANN-LEMLES, the average reaction rates on the LEM domain are obtained as:

$$\frac{\overline{\dot{\omega}_i}}{\overline{\rho}} = f(Y_k, T) \tag{3.3}$$

For TANN-LES, the average filtered reaction rates are obtained as:

$$\frac{\overline{\dot{\omega}_i}}{\overline{\rho}} = f\left(\widetilde{Y}_k, \widetilde{T}, Re_\Delta, \frac{\partial \widetilde{Y}_i}{\partial x_j}\right) \tag{3.4}$$

The filtered species concentrations, temperature and the source terms are obtained by Favre-filtering the data obtained from the standalone LEM simulation on the LES grid size. The subgrid Reynolds number in the LES is calculated as $Re_\Delta = u'\Delta/\nu$, where $u' = (2/3)^{1/2} k^{sgs}$ and Δ is the LES grid filter. In the stand-alone LEM, the grid spacing, stirring length and time scales are selected as a function of the Re_t

and L. Note that the Re_t is a *global* variable for the stand-alone LEM, and thus is different than the Re_Δ, which is a *local* variable calculated by the LES. Stand-alone LEM provides the instantaneous scalar profile but the turbulence level *locally* is not known. In order to link the stand-alone LEM simulation to the LES turbulent scales, the following kinetic energy k model equation is solved by the stand-alone LEM in addition to the species and energy equations:

$$\frac{dk}{dt} = P_k - \epsilon \tag{3.5}$$

where P_k is the production term determined approximately as $C_k k^*/\Delta t_{stir}$, where $C_k = O(1)$ is constant and Δt_{stir} is the stirring time used in the LEM model [17]. To begin the simulation k is initially assigned zero in the LEM domain. Then, the u' on a segment of length l, where triplet-map (which is representative of the turbulent stirring) is applied can be estimated as $u' = \frac{\nu Re_t}{l}$, where l is the instantaneous characteristics eddy size used for turbulent stirring. Hence, whenever triplet-map is applied on the scalar field, the representative k^* is calculated as $3u'u'/2$ and is used in the production term (P_k). The dissipation term is modeled as $\epsilon = (u')^3/\Delta s$, where Δs is the LEM resolution. The main idea in the above equation is that the turbulence is homogeneous, which is consistent with the basic LEM assumption as well. Hence, the proposed way of calculating k does not contradict any assumptions already being made in the LEM formulation.

The TANN training table is obtained by spatially sub-filtering the LANN table used for the previous study [2]. The stand-alone LEM code is started from the same initial species profiles and is run for the same range of conditions (Re_t, L) with the DNS case. Unlike the procedure followed in the earlier study [2], the results here are filtered by a filter size equal to the grid spacing used in the LES. In addition to the previous chapters, the details of the ANN training algorithm are also given in Refs. [45, 46]. As will be shown in the results, the same TANN can be used for a range of problems having different levels of grid resolution with significant reduction in computational cost and reasonable accuracy of results.

3.3.2 Problem Setup and ANN training

All three cases, L, M and H respectively corresponding to low, medium high Re, from the aforementioned DNS study [34] are considered here. The composition of the fuel and oxidizer streams for cases L and H are identical to case M discussed in Section 3.2. The domain size is $L_X = 12H$ in stream-wise direction, $L_Y = 14H$ in the transverse direction and $L_Z = 8H$ in the span-wise direction. The boundary conditions are periodic, non-reflecting outflow and periodic in the stream-wise, transverse and spanwise directions, respectively. The DNS study employs a uniform grid. The details two DNS cases are give in table 3.10.

The LES study employs grids clustered in the shear layer with smooth stretching towards the transverse boundaries. Uniform spacing is used in the other two directions. The details of the LES setup for cases L and H, is given in table 3.11 where a grid resolution study is performed. Like the DNS study, the LES is initialized with

Parameter	Case L	Case M	Case H
$H(mm)$	0.72	0.96	1.37
Re_{jet}	2510	4478	9079
Grid Size (M)	1.48	5.5	5
Grid Resolution	0.83η	2.5	1.67η

Table 3.10: DNS parameters for test cases

Grid Resolution	Size	min. Δy	max. Δy
Case L	$90 \times 126 \times 50$ $(0.56M)$	0.055 mm	0.152 mm
Case H (C-GRID)	$120 \times 180 \times 90$ $(1.9M)$	0.045 mm	0.218 mm
Case H (M-GRID)	$160 \times 240 \times 120$ $(4.6M)$	0.035 mm	0.161 mm
Case H (F-GRID)	$200 \times 300 \times 150$ $(9M)$	0.028 mm	0.129 mm

Table 3.11: LES grid resolution

a laminar flamelet solution at a scalar dissipation rate $\chi = 0.75\chi_q$ ($\chi_q = 2194s^{-1}$ extinction scalar dissipation rate). Isotropic background turbulence is added to trigger the shear generated turbulence, with initial turbulent length scale $H/3$ and turbulent intensity $0.05U$, where U is the characteristic jet velocity. For calculating the heat and species diffusion fluxes mixture-averaged transport properties are used.

3.3.3 TANN-LES validation: Case M

Earlier DNS [34] and LEMLES [2] showed (as also shown in 3.2) that as the mixing layer evolves, the flame first goes extinct at around t_j =20, where t_j is the non-dimensional time given as $t_j = t/(H/U)$, with H and U denoting the jet height and characteristic velocity, respectively. Later, as the strain drops, the flame reignites around t_j =40. Although data over t_j 0-50 is obtained, for comparison with the DNS, only these two instants are discussed here.

The conditional mean of the OH mass fraction obtained by the TANN-LES is shown in Fig. 3.27 at t_j =20 and 40. The DNS data (shown by symbols) and the laminar flamelet value at extinction (also given by the DNS study) are also shown for comparison purposes. The TANN-LES can detect extinction (at $t_j = 20$) and reignition (at $t_j = 40$) with an acceptable error. The TANN-LES tends to slightly overpredict the OH profile especially at oxidizer rich conditions. At reignition, the TANN-LES shows higher values of OH mass fraction within the computational domain. The variation of the OH mass fraction with respect to the mixture fraction is skewed towards the oxidizer side compared to the DNS data as well. Nevertheless, the overall accuracy is considered acceptable.

The conditional H_2 mass fraction at extinction (Fig. 3.28b) also agrees well with the DNS data. At reignition, however there are two main differences. The first one is the maximum value of the mixture fraction up to which H_2 exists. This is similar to

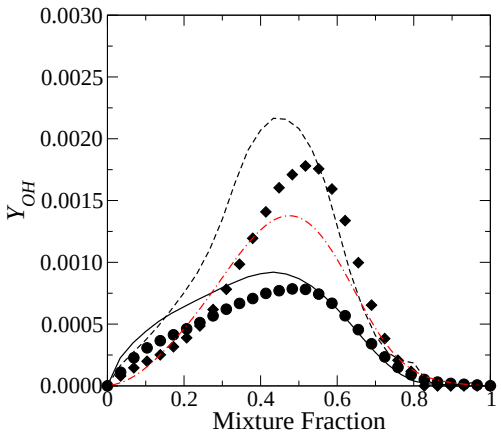

Figure 3.27: Conditional mean of OH mass fraction obtained by TANN-LES and DNS. (•) DNS, (—) TANN-LES at $t_j = 20$; (⧫) DNS, (- - -) TANN-LES at $t_j = 40$; (- . -) laminar flamelet value at extinction.

that of observed for CO mass fraction in Fig. 3.28a. The second difference is that the TANN-LES tends to overpredict the H_2 mass fraction at all mixture fraction values compared to the DNS data. Here, it should be re-emphasized that although both CO and H_2 are fuel species, their conditional statistics represent different variations with respect to the mixture fraction. The CO is almost linear, whereas H_2 is more non-linear. The curvature for H_2 statistics is changing with respect to time as seen in Fig. 3.28b. Regardless, inspite of the slight over-prediction, the TANN-LES seems to be capturing all of these features consistently for both species.

The capability of the TANN-LES to predict flame dynamics is further evaluated by comparing the results obtained by the current model against subgrid combustion models that exist in the literature. Figure 3.29 shows the variation of the mean OH mass fraction conditioned on the mixture fraction obtained by TANN-LES, LANN-LEMLES and EBU-LES. Among the models considered here, the EBU-LES gives the worst results. The LANN-LEMLES and TANN-LES, on the other hand provides results comparable with the DNS data. The LANN-LEMLES predicts more extinction compared to TANN-LES at t_j =20. At $t_j = 40$, on the other hand, the LANN-LEMLES gives better agreement with the DNS data compared to the TANN-LES. Although the TANN is trained on a data extracted from a similar grid resolution, LANN-LEMLES is solving the subgrid scalar field variation on-line and thus, has an effectively much finer grid compared to the TANN-LES. Strictly speaking, this implies that TANN-LES should be using a grid that is finer than what was used for LANN-LEMLES. Another difference between the two approaches is that in the TANN-LES a conventional eddy diffusivity closure is used to close the subgrid scalar flux whereas the LEMLES employs a subgrid scalar mixing model that is known capable of capturing both gradient and counter-gradient diffusion. Finally, the two approaches employ different closure for the reaction rate. In TANN-LES approach the filtered reaction rate is actually a closure model wheres in the LEM the kinetics are

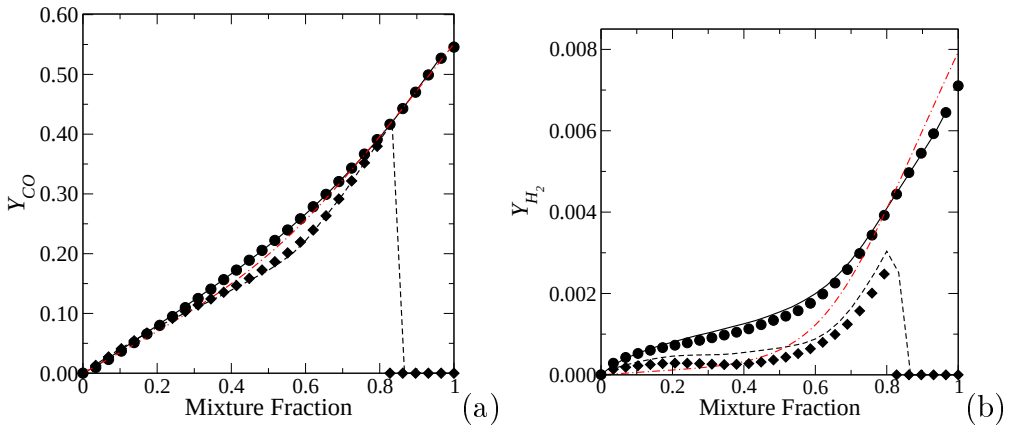

Figure 3.28: Conditional means of (a) CO and (b) H_2 mass fraction obtained by TANN-LES and DNS. (•) DNS, (—) TANN-LES at $t_j = 20$; (⧫) DNS, (- - -) TANN-LES at $t_j = 40$; (- . -) laminar flamelet value at extinction.

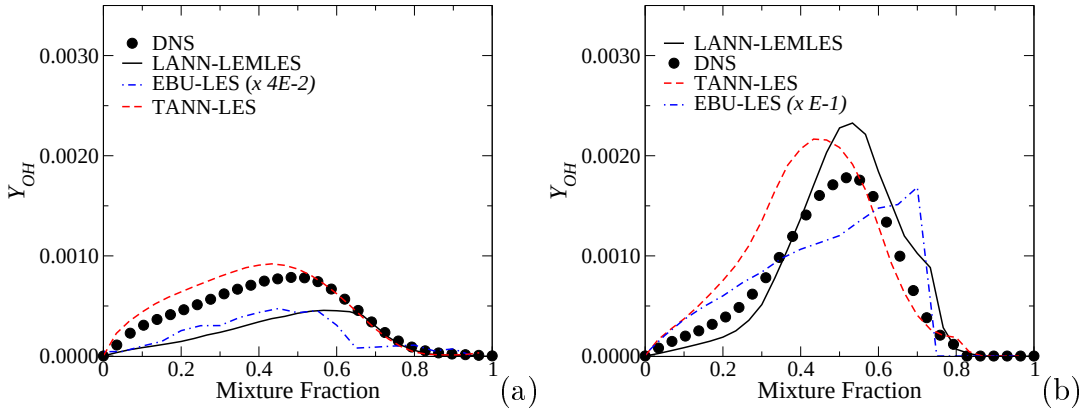

Figure 3.29: Mean value of the PDF of Y_{OH} conditioned on mixture fraction calculated by LANN-LES, TANN-LES and EBU-LES at $t_j =$ (a) 20 and (b) 40.

closed exactly. Nevertheless, the overall ability of the TANN approach is encouraging considering the enormous reduction is cost that is achieved as explained below.

3.3.4 TANN-LES validation: Cases L and H

To further validate the TANN methodology the Case L is run first with DI-LEMLES, ANN-LEMLES and later with TANN-LES. The ANN and the TANN net were generated for a small range of Re_t upto 800 and time step size 2.5e-08s and filter size of 0.1 mm (TANN-1). Fig. 3.30(a) shows the variation of the mean temperature on the stoichiometric plane ($Z_{st} = 0.43$) with respect to the nondimensionalized-time (t_j) for DNS, DI-LEMLES, ANN-LEMLES and TANN-LES using TANN-1. The time is non-dimensionalized by the reference time obtained as $t^* = H/U$, where U is the characteristic jet velocity [34]. The DNS data shows that the temperature begins at 1455 K and drops off to approximately 1210 K near $t_j = 20$, indicating extinction.

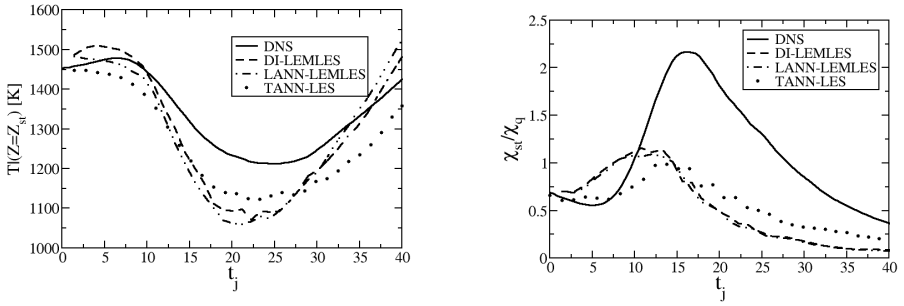

(a) (b)

Figure 3.30: (a) Variation of the mean of temperature at stoichiometric mixture fraction with respect to non-dimensional time for Case L, (b) Variation of the mean χ/χ_q at stoichiometric mixture fraction with respect to non-dimensional time for Case L

Beyond this point the temperature starts increasing again and reaches 1425 K at $t_j = 40$, showing the reignition process. The DI-LEMLES initially overpredicts the temperature till $t_j = 10$ beyond which it drops off faster than the DNS temperature profile. ANN-LEMLES and TANN-LES almost at all instants till $t_j = 20$ underpredict the mean temperature. The DI-LEMLES, ANN-LEMLES underpredict the temperature by approximately 150 K and the TANN-LES underpredicts the temperature by approximately 100 K at $t_j = 20$, indicating more extinction. Beyond this point, the profile for DI-LEMLES and TANN-LES increases at a higher rate compared to DNS temperature profile, while the TANN-LES temperature profile increases at the same rate as the DNS. At $t_j = 40$ the DI-LEMLES, ANN-LEMLES overpredict the temperature by approximately 100 K and TANN-LES underpredicts the temperature by approximately 50 K. The major cause of these descripencies is the overall grid coarseness [2]. Inspite of these descripencies the results in general show a good match with the DNS data. Fig. 3.30(b) shows the variation of the mean χ_{st}/χ_q on the stoichiometric plane with respect to t_j. The DNS simulations initializes at $\chi_{st}/\chi_q = 0.75$ (approx.) and increases to 2.16 at $t_j = 16$ due to the shear generated turbulence. Beyond this point it starts decaying and drops off to 0.35 at $t_j = 40$. Comparing Fig. 3.30(a) and 3.30(b) it is observed that the local extinction is due to the fluctuations of the scalar dissipation rate. Once the molecular mixing overcomes the effect of turbulent straining, it leads to the decrease of the scalar gradients which is accompanied by gradual reignition [37]. A time lag is observed between the maximum χ_{st}/χ_q and the minimum temperature on the stoichiometric plane [47] because the reaction rate does not immediately follow variations of χ_{st} due to the finite rate chemistry [48]. The DI-LEMLES and ANN-LEMLES predict a faster initial rate of growth of mean χ_{st}/χ_q compared to the DNS, while the TANN-LES predicts a slower initial rate of growth of χ_{st}/χ_q. The maximum mean χ_{st}/χ_q observed is approximately 1.1 and close to $t_j = 12$ for DI-LEMLES and ANN-LEMLES, while the maximum mean χ_{st}/χ_q for TANN-LES is observed close to $t_j = 15$ and has a

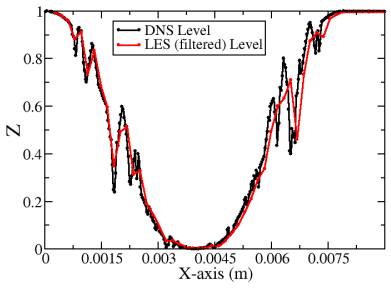

Figure 3.31: Variation of mixture fraction (Z) along the 1D standalone LEM domain at the DNS level and the LES level

value of 1 approximately. Beyond this point χ_{st}/χ_q decays off and reaches a value less than 0.2 at $tj = 40$ for DI-LEMLES and ANN-LEMLES, while it has a value of 0.25 approximately for TANN-LES. The TANN-LES underpredicts χ_{st}/χ_q compared to LEMLES till $t_j = 15$ and after that it slightly overpredicts.

Overall the data obtained from TANN-LES is in good agreement with DI-LEMLES data. The difference between the DNS data and LES data is observed due to the difference in grid resolution. This is explained in Fig. 3.31, which shows the variation of Z on the DNS level and the filtered LES level on a 1D-domain. The black dots and the red dots show the DNS and the LES grid locations, respectively. The sharp gradients in Z observed near $X = 0.0022$m and $X = 0.0056$m at the DNS level are mitigated at the filtered level. Thus, DNS grid captures the small scales and hence sees much larger fluctuations whereas the small scales are filtered over the LES grid size at the LES level which leads to lower fluctuations of the scalar field and thus lower values of χ.

The mean value of temperature and H_2O mass fraction conditioned on the mixture fraction at extinction ($t_j = 20$) and reignition ($t_j = 40$) are shown in Fig. 3.32(a)-3.32(d) with DNS, DI-LEMLES, ANN-LEMLES and TANN-LES using TANN-1. At extinction, the LES results underpredict the mean temperature at almost all values of Z compared to the DNS. Above $Z = 0.95$ TANN-LES slightly overpredicts the mean temperature. Overall the TANN-LES mean temperature profile shows the best match with the DNS temperature profile. The maximum value of Z observed for DI-LEMLES and ANN-LEMLES is 0.93. For TANN-LES the maximum value of Z observed is 0.975 and for DNS it is 0.97. Thus DI-LEMLES and ANN-LEMLES overpredict mixing while TANN-LES slightly underpredict the mixing compared to DNS, at extinction. A similar trend in mixture fraction is observed at reignition and the maximum value of Z for DNS drops to 0.83. DI-LEMLES and ANN-LEMLES overpredicts the mean temperature profile whereas TANN-LES underpredicts the temperature profile at almost all values of Z, at reignition. The deviation at higher values of Z at reignition is observed mainly due to the grid coarseness which results in very few data points in the high mixture fraction regime. The maximum temperature at both $t_j = 20$ and $t_j = 40$ is observed on the fuel-rich side instead of stoichiometric

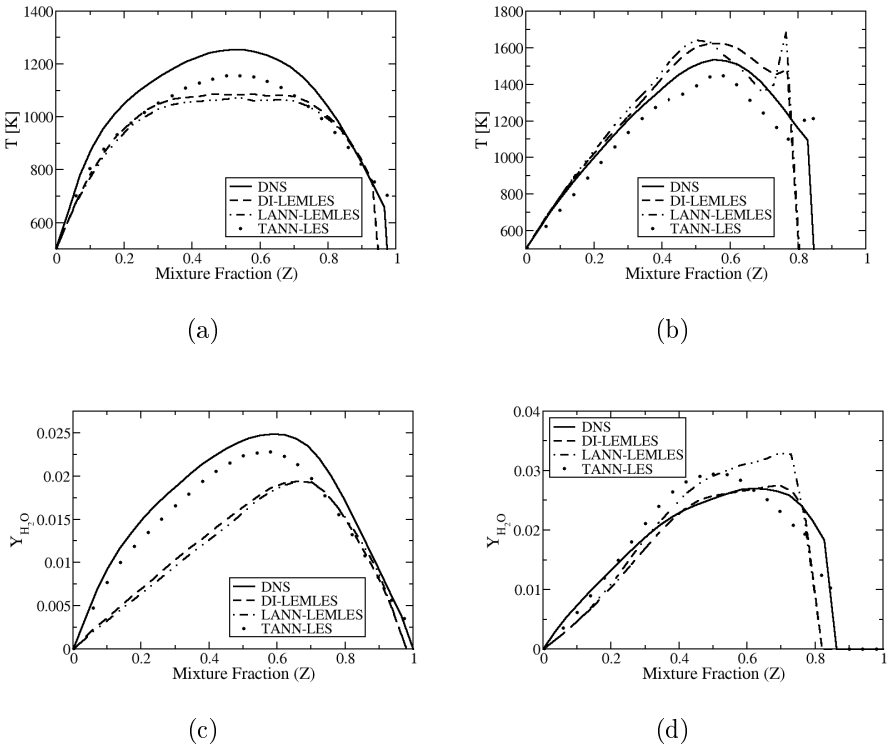

Figure 3.32: Conditional mean of temperature and Y_{H_2O} at extinction (a and c) and reignition (b and d)

plane ($Z_{st} = 0.43$). This is observed due to the significant differential diffusion effect which leads to higher diffusion velocities of lighter species like H, H_2 OH and O compared to other species. The radicals diffuse more towards the fuel side and shift the location of the maximum heat release also making the heat release zone wider [49]. At extinction, the H_2O mass fraction is underpredicted for all values of Z by the LES simulations. DI-LEMLES and ANN-LEMLES underpredicts the production of H_2O more whereas TANN-LES underpredicts it less compared to the DNS, which is consistent with the temperature profile predictions suggesting more extinction compared to the DNS and thus less heat release rate and less production of products. The location of the maximum mass fraction of H_2O lies in the fuel-rich side, around 0.6 for DNS and TANN-LES and around 0.7 for DI-LEMLES and ANN-LEMLES due to differential diffusion effects. The DNS data shows that maximum mass fraction of H_2O increases from 0.025 to 0.027 at $t_j = 20$ to $t_j = 40$. The LES results overpredict the maximum mass fraction of H_2O at reignition compared to DNS. The location of the maximum mass fraction of H_2O is observed further towards to the fuel-rich side for DNS, DI-LEMLES and ANN-LEMLES, whereas for TANN-LES it is observed closer to the stoichiometric mixture fraction on the fuel-rich side. Inspite of these discrepancies, considering the difference in grid resolution for LES simulations and DNS, the LES results exhibit reasonable agreement with the DNS results.

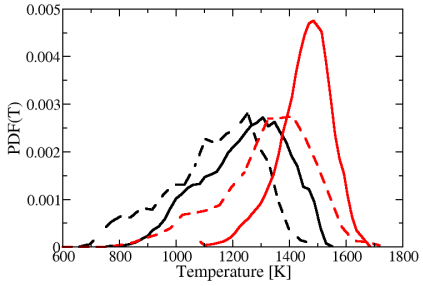

Figure 3.33: Variation of the PDF of temperature on the stoichiometric plane at extinction: black and reignition: red. Continuous line: DNS, Dashed line: TANN-LES

Fig. 3.33 shows the pdf of temperature on the stoichiometric plane at extinction and reignition, for DNS and TANN-LES using TANN-1. At extinction ($t_j = 20$), the shape of the pdf of TANN-LES matches well with the DNS pdf profile. A long tail of pdf is observed because of the fluctuations of $\chi_{st} > \chi_q$. This create extinguished regions which results from the rapid molecular mixing of the reactants with hot products, at a mixing rate greater than the chemical consumption rate of reactants. The reignition process does not follow immediately after the extinction, the cold regions get accumulated and lead to the formation of the low temperature tail of the pdf [37],[50]. Later in time, once the scalar dissipation rate has reduced and the reignition process had occurred by $t_j = 40$ the low temperature tail subsides as observed for the DNS. The TANN-LES shows the decay of this tail to a lesser degree, which suggests underprediction of the reignition process. By $t_j = 40$ the flame spreads to the coarser regions of the grid and the stoichiometric plane no longer lies in the fine grid region which leads to the prediction of the long tail at low temperature. The mean temperature is under-predicted at both extinction and reignition.

Fig. 3.34(a) and 3.34(b) show the pdf of H_2O mass fraction on the stoichiometric plane for DNS and TANN-LES using TANN-1 at extinction and reignition, respectively. At extinction, the pdf of H_2O mass fraction for TANN-LES shows good agreement with the DNS pdf profile, whereas, at reignition, the TANN-LES pdf profile exhibits more spread compared to DNS. Further, at extinction more deviation is observed from the corresponding β-pdf for both DNS and TANN-LEMLES results, compared to the DNS and TANN-LEMLES results at reignition. This is in agreement with the observations made by Goldin et. al. [51, 52]. Near extinction, due to higher levels of chemical non-equilibrium caused by the large values of χ on the stoichiometric plane the scalar field deviates away from the β-pdf [51]. At $t_j = 40$ (reignition) once the χ on the stoichiometric plane has dropped off and the Da has increased, the system once again approaches chemical equilibrium and the pdf of both DNS and TANN-LEMLES show good match with the corresponding β-pdf. More spread about the mean is observed at extinction compared to reignition due to the high scalar dissipation rates for both DNS and TANN-LES data. Inspite of these discepencies the

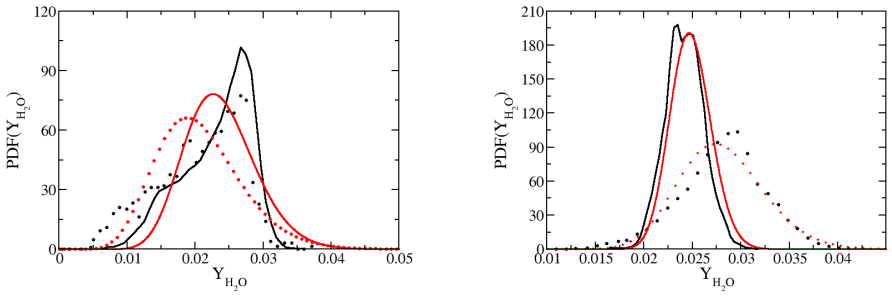

(a) (b)

Figure 3.34: Variation of the PDF of H_2O mass fraction on the stoichiometric plane at (a) extinction and (b) reignition. Black continuous line: DNS data, Red continuous line: beta pdf corresponding to DNS data, Black symbols: TANN-LES data, Red symbols: beta pdf corresponding to TANN-LES data.

TANN-LES agrees well with the DNS data.

From the above studies it is concluded that the TANN-LES is a robust methodology and the results predicted by it compare well with the DNS, DI-LEMLES and ANN-LEMLES predictions. For all the results reported hereafter only TANN-LES computations were done.

3.3.5 Capability of TANN for a range of Re and grid resolution

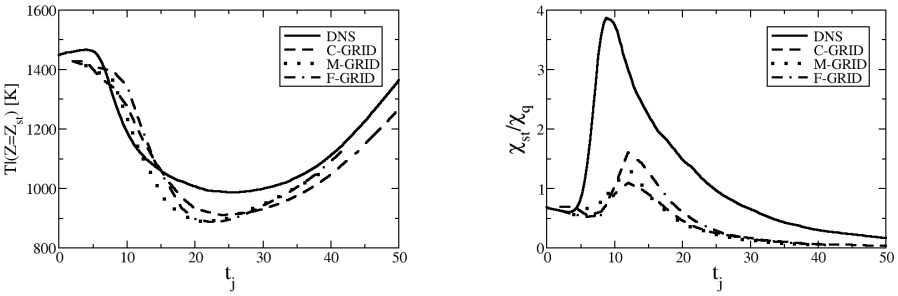

(a) (b)

Figure 3.35: Case H (a) Variation of the mean of temperature at stoichiometric mixture fraction with respect to non-dimensional time, (b) Variation of the mean χ/χ_q at stoichiometric mixture fraction with respect to non-dimensional time

The TANN-1 failed to predict extinction-reignition for Case H. Hence another TANN (TANN-2) was generated for a larger range of Re_t than TANN-1 upto 1500, filter-size of 0.042 mm and time-step size 1e-08s. TANN-LES simulation was done

using TANN-2 for all the test cases mentioned in table 2. Fig. 3.35(a) and 3.35(b) show the variation of the mean temperature and mean χ_{st}/χ_q on the stoichiometric plane ($Z_{st} = 0.43$) with respect to t_j for DNS and TANN-LES using TANN-2 for case H C-GRID, M-GRID and F-GRID. Due to variation in the grid refinement the F-GRID estimates the highest mean χ_{st}/χ_q and the C-GRID estimates the lowest. All the grids for case H predict the highest mean χ_{st}/χ_q around $t_j = 12$ which is slightly later in time compared to the prediction of DNS. After $t_j = 15$ the temperature field is slightly underpredicted by all the three grids compared to the DNS data. The M-GRID and F-GRID underpredict the temperature more near extinction $t_j = 20$ compared to the C-GRID and show better match with the DNS data near reignition $t_j = 40$. However considering the difference in grid resolution of C-GRID, M-GRID and F-GRID the mean temperature prediction of all the three grids are reasonably consistent and compare well with the DNS data.

Figs. 3.36(a)- 3.36(f) shows the comparison of the pdfs of temperature, H_2O and OH mass fractions at extinction and reignition on the stoichiometric plane for C-GRID, M-GRID, F-GRID and DNS. The pdf profile of temperature matches well with the DNS data at extinction for all the three grids with a slight underprediction of mean and overprediction of the variance. At reignition the shape of the pdf does not match well with the DNS mainly because by $t_j = 40$ the flame spreads to the stretched regions of the grid in the Y-direction and hence grid coarseness affects the shape of the pdf. From C-GRID to F-GRID with increase in refinement the pdf approaches the DNS pdf shape. At extinction, the pdf of the mass fraction of both H_2O and OH match well with the DNS for all the three grids with the variance slightly overpredicted, indicating more extinction. However at reignition, for both the species the TANN-LES pdf profiles exhibit lesser spread compared to DNS, indicating a faster decay of the scalar dissipation rates and more reignition. More deviation from the β-pdf is observed for the H_2O mass fraction compared OH mass fraction because OH radical has smaller chemical time scales compared to H_2O and hence is less affected by the reduction in diffusion time scales due to high scalar dissipation rate. Overall the TANN-LES pdfs for all the three grids are in good agreement with the pdfs obtained from DNS.

Fig. 3.37(a) and 3.37(b) show the comparison of the pdf of the normalized χ_{st} at different instants of time for C-GRID and F-GRID, respectively. Maximum negative skewness is observed at $t_j = 10$ where the mean χ_{st} is maximum for both the cases. The negative skewness is observed because at high values of mean χ_{st} only at very limited number of points on the stoichiometric plane the χ reaches very high values and shift the mean. At majority of the points on the stoichiometric plane the χ values lie below the mean and hence result in negative skewness. This phenomenon is explained in Fig. 3.38(a) and 3.38(b), which show the distribution of χ with respect to temperature on the stoichiometric plane for C-GRID and F-GRID, respectively. At $t_j = 10$ maximum points lie below mean χ_{st} value of 2000 and 2300 for C-GRID and F-GRID, respectively. A very small fraction of points lie above this mean and has χ_{st} values as high as 4 times and 8 times greater than mean χ_{st} for C-GRID and

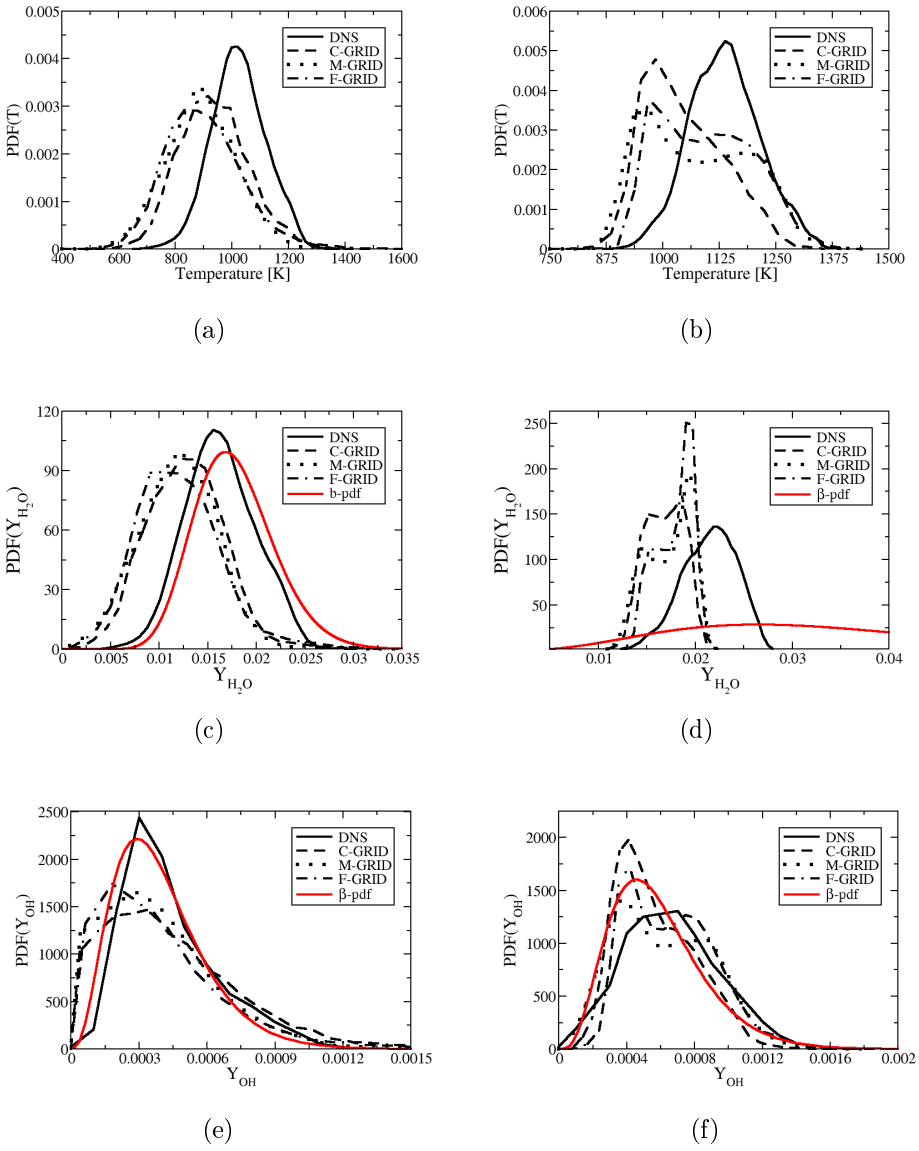

Figure 3.36: Variation of PDF of temperature, H_2O and OH mass fraction on stoichiometric plane at extinction: (a),(c),(e) and reignition: (b),(d),(f) for Case H with TANN-2

F-GRID, respectively. It is also observed that at χ_{st} above the mean the temperatures are lower indicating the formation of extinguished regions [53]. At $t_j = 40$ the stoichiometric data is spread over a wider range of temperature compared to the stoichiometric data at $t_j = 10$ and it is spread more uniformly about a lower mean of χ_{st} of 130 and 160 for C-GRID and F-GRID, respectively, which indicates partial reignition. This results in less negative skewness. Further it is observed that at $t_j = 10$ the stoichiometric data is more clustered below $\chi_{st} = 2000$ for F-GRID compared to C-GRID. This has lead to the smoother normalized χ_{st} profile for F-GRID compared to C-GRID at normalized χ_{st} values less than -3. Similar to $t_j = 40$ at $t_j = 20$ and

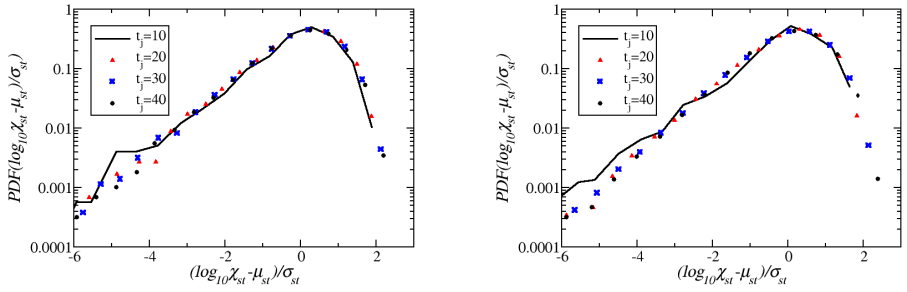

(a) (b)

Figure 3.37: PDF of the normalized scalar dissipation rate at the stoichiometric mixture for Case H with TANN-2. (a) C-Grid, (b) F-Grid

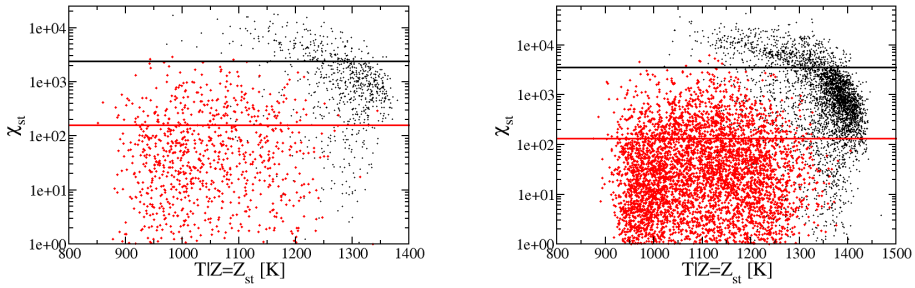

(a) (b)

Figure 3.38: Distribution of χ_{st} with respect to temperature on the stoichiometric plane for Case H. Black dots: $t_j = 10$, Red dots: $t_j = 40$ for (a) C-GRID, (b) F-GRID

$t_j = 30$, the mean χ_{st} is low and hence the negative skewness is not observed. Overall the pdf of normalized χ_{st} for C-GRID and F-GRID are in good agreement.

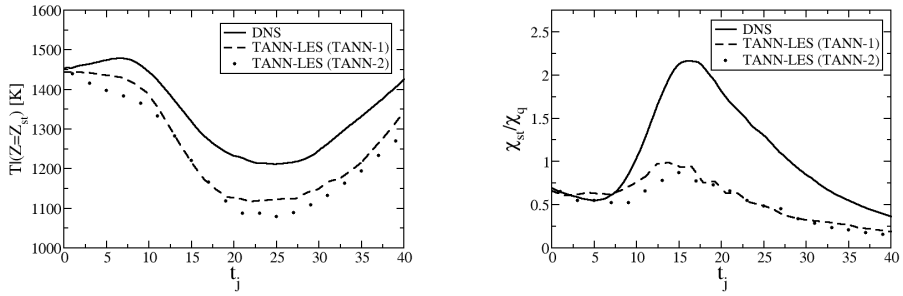

(a) (b)

Figure 3.39: Comparison of the variation of (a) mean temperature and (b) mean χ/χ_q on the stoichiometric plane for Case L using TANN-1 and TANN-2

To show that TANN-2 which is more "generalized" compared to TANN-1, is capable of handling a range of Re, case L was simulated with TANN-LES using TANN-2. Fig. 3.39(a) and 3.39(b) show the comparison of the temporal variation of mean temperature and mean χ_{st}/χ_q on the stoichiometric plane for case L using TANN-1 and TANN-2. Both TANN-1 and TANN-2 underpredict the temperature on the stoichiometric plane throughout the course of the simulation. TANN-1, trained on a smaller range of Re_t and grid-size matching with case L predicts a solution closer to DNS compared to TANN-2 trained on a wider range of Re_t and smaller grid spacing. The mean χ_{st}/χ_q is slightly underpredicted by TANN-2 compared to TANN-1 till $t_j = 15$, beyond which the TANN-1 results almost overlap with TANN-2 results. Overall the TANN-1 and TANN-2 results match well for case L and loss of accuracy by using the generalized net TANN-2 compared to the case specific net TANN-1 is negligible.

3.3.6 Conclusions

The ANN methodology is used for multi-step finite rate kinetics within the LES framework. Unlike the previous work [45] where ANN was used as a subgrid combustion model within the LES framework (ANN-LEMLES), here ANN is used for calculating the filtered reaction rates directly within the LES framework (TANN-LES). The thermo-chemical data for training the TANN is obtained by filtering the data obtained from a 1D standalone simulation over the LES grid-size [54]. The comparison of the average laminar source terms and average filtered source terms for the same composition show significant difference. The average filtered source terms are trained as a function of the filtered mass fraction of all the species, filtered temperature and the gradient of the species. The species are trained separately.

The TANN-LES is used to simulate the temporally evolving syngas-air diffusion flames, exhibiting significant extinction-reignition, extensively studies by DNS [34] previously. TANN-LES methodology is first validated against DI-LEMLES, ANN-LEMLES and DNS results for the low Re case. The temporal variation of the mean temperature on the stoichiometric plane from TANN-LES results compare well with the DI-LEMLES, ANN-LEMLES and DNS with significant speed-up. To further investigate the TANN-LES approach the conditional statistics are extracted and compared with the DNS data at extinction ($t_j = 20$) and reignition ($t_j = 40$). It is observed that the location of the maximum mean temperature does not lie at the stoichiometric mixture fraction due to differential diffusion effects, instead it lies towards the fuel rich side. The same trend is observed for the H_2O mass fraction. A comparison of the pdf of temperature and H_2O mass fraction indicate slight underprediction of reignition by TANN-LES. Overall the TANN-LES predictions match well with LEMLES and DNS predictions.

The low Re case specific TANN fails to capture the extinction-reignition phenomenon for the high Re case. An attempt is made in generalizing the TANN approach by generating a TANN that can simulate cases with different Re and grid

resolutions. The training table for the "generalized" net is generated by running the standalone LEM simulation for a large range of Re_t and an intermediate filter-size. The TANN-LES results using the generalized net obtained for the high Re case with three different grid resolutions compare well with the DNS data, showing grid independence and capability of the generalized net in handling different grid resolutions. Both coarse grid and the fine grid capture the negative-skewness at high scalar dissipation rate in the pdf of the normalized scalar dissipation rate. Comparison of the TANN-LES results for the low Re case using the generalized net with the TANN-LES results using the case specific net show that loss in accuracy by the use of the generalized net is negligible.

A comparison of the training data for the two TANNs with the data from the two two Re cases show that both the nets cover the same compositional data space and the thermochemical data from the LES forms a subset of the thermochemical datapsace of the nets. The χ and the Re_t dataspace explored by the two nets differ. The Re_t dataspace of the LES still forms a subset of the training data of the two nets. However, the χ dataspace of the high Re case falls outside the training dataspace of the first net which leads to its failure in simulating the high Re case. The χ dataspace for both Re cases form a subset of the χ dataspace of the generalized net training dataspace and hence it is capable of simulating different Re cases.

3.4 Application of TANN-LES in a Stagnation Point Reverse Flow Combustor (SPRF)

3.4.1 SPRF combustor

The second test case is the SPRF combustor, designed at Georgia Tech, that uses a novel exhaust gas re-circulation technique to reduce both NOx and CO emissions. The combustor can work both in premixed and non-premixed modes. Here, only the premixed mode is considered to demonstrate the ANN capabilities. In the premixed mode, the methane/air mixture is injected into the combustion chamber at an effective equivalence ratio of 0.58. Flow enters and leaves the combustion chamber at the same plane, which provides extensive reactant preheating and mass entrainment across the shear layers. Thus, the reaction rates are enhanced and the flame can be stabilize at very lean conditions. This phenomenon, which is known as the exhaust gas recirculation technique, allows feeding the CO leaving the combustor back into the incoming flow stream, so that any CO that may exist due to partial combustion can be subsequently burnt again.

The flow features and the combustion characteristics of the combustor were investigated previously by using LEMLES with a global 2 step reaction mechanism [1]. The LEMLES results where compared with a conventional Eddy Breakup (EBU) type LES (EBU-LES) and an artificially thickened flame (ATF) LES (TF-LES) The results using LEMLES showed reasonable agreement with measured velocity field and flame structure, and analysis showed that significant mixing between the reactants and the recirculating products occur in the near field, which provided pre-heating as well as dilution effect. This led to a complex reignition and extinction process in the near field but was only approximately captured using the reduced 2-step kinetics. The current study aims to investigate the same flame with the TANN approach, which is trained by using a 12 step-16 species reaction mechanism. LEMLES using the same kinetics is deemed computationally very expensive due to the stiffness of the chemistry and the long time needed to reach stationary state since the recirculation from the stagnation plane is a very slow process. However, as shown here, using the TANN approach it is feasible to simulate this type of partially premixed ignition and combustion process in this geometry.

The numerical set-up used in the current study is identical to that of used in the earlier study [1], and the schematics is given in Fig. 3.40. The combustion chamber (5) is enclosed with an end-plate (6) at one end. The outflow (4) is at the same plane with the injectors (2, 3). In the non-premixed mode the fuel (2) and the oxidizer (3) streams are introduced into the combustion chamber through different pipes. In the premixed mode, the central tube (2) is closed and the fuel/air mixture is discharged from the same pipe (3). The annular jet is preheated to 500 K and the annular injector Reynolds number is 12,900. A 1/8 turbulent velocity profile is imposed as a boundary condition at the inlet with the mean velocity of 122 m/s. The boundary conditions are listed in details in Table 3.12. The chemical reaction rates are calculated using a 12-step, 16 species skeletal methane/air reaction mechanism [55].

The grid used for the computations is shown in Figs. 3.41a-b. A two-domain

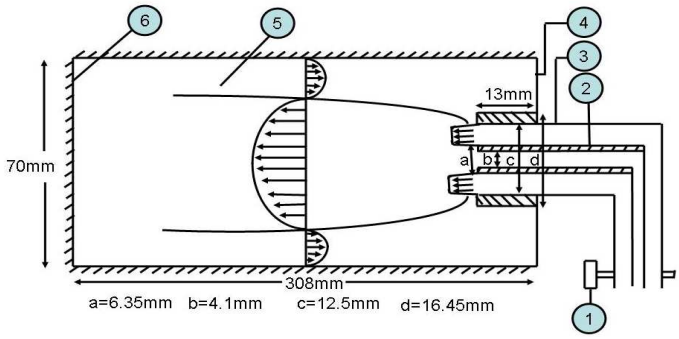

Figure 3.40: Schematics of the SPRF combustor [1].

Table 3.12: Boundary conditions used for the LES [1].

	Reacting premixed	Reacting non-premixed
Annular jet rate $[m^3/s]$	0.00676	0.00638
Central jet flow rate $[m^3/s]$	-	0.00038
Annular jet temperature K	500	450
Central jet temperature K	-	300
Annular jet bulk velocity m/s	122	104
Equivalence ratio (ϕ)	0.58	0.58
Annular injector Re (Re_a)	12,900	10,160
Central jet Re (Re_c)	-	7,680
Subgrid Re (Re_Δ)	304	274

butterfly type of grid, which comprises of a cartesian grid in the center of a cylindrical grid is used. Here, 194×75×57 and 194×15×15 number of nodes in x, y and z directions are used for the cylindrical and cartesian grids, respectively. The grid is clustered towards the dump plane and the shear layers in order to increase the quality of the LES in these regions. The validation of the selected grid is given in the previous studies [1] and is not repeated here for the sake of brevity.

The ANN training table for this case is generated by using the same stand-alone LEM code but for the premixed combustion mode. The database is constructed based on the conditions relevant to the SPRF combustor, i.e., the scalar field is initialized based on the laminar solution obtained for an equivalence ratio of 0.58 and the Re_t range used in the training varied between 10 to 400.

3.4.2 TANN-LES of the SPRF combustor

The instantaneous and time averaged surface plots of the temperature are shown in Figs. 3.42a and b, respectively. The variation of the instantaneous temperature within the combustion chamber suggests a highly wrinkled flame front. Hot pockets of temperature exists within these structures indicating that the combustion is mainly occurring at these locations. On a time averaged sense, however, as seen in Fig 3.42b,

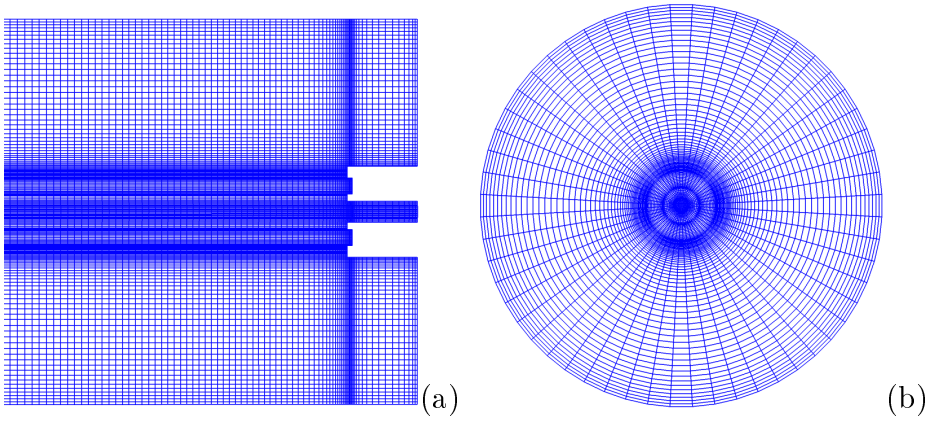

Figure 3.41: Side and cross-sectional views of the grid used for the LES.

these instantaneous fluctuations vanish and the flame front becomes much smoother. Towards the end of the combustor the temperature reaches its peak value. The flow, which leaves the combustor, however, has a lower temperature, since it mixes with the incoming fresh reactants and provides pre-heating.

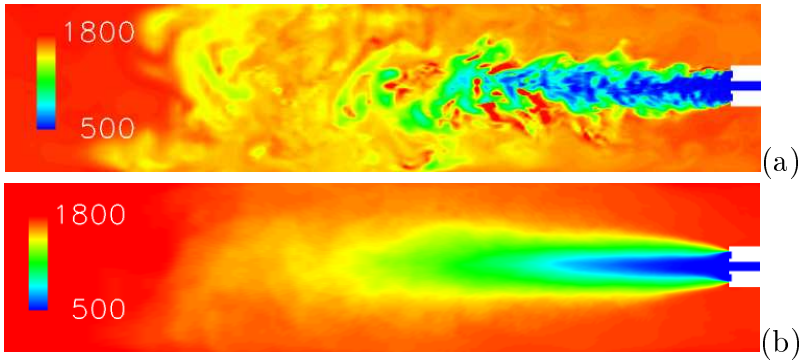

Figure 3.42: (a) Instantaneous and (b) time-averaged temperature surface plot.

The instantaneous and time averaged surface plots of the CH_4 mass fraction are shown in Figs. 3.43a-b. Both figures show that the fuel is completely consumed within the combustion chamber. The vorticies shedding from the injection plane provides mixing (and combustion) in the shear layer, which is evidenced by the decrease in the peak value of the CH_4 mass fraction as shown in Fig. 3.43a. Towards the middle of the combustor the fuel mass fraction decreases significantly and exists only in large pockets.

The center line variations of the time averaged axial velocity and temperature are given in Figs. 3.44a and 3.44b, respectively. For comparison purposes earlier predictions obtained using the same grid and flow conditions, but with different sub-grid combustion models [1] are also given in the figures. All the models considered here show the existence of a re-circulation zone, which is located approximately 5

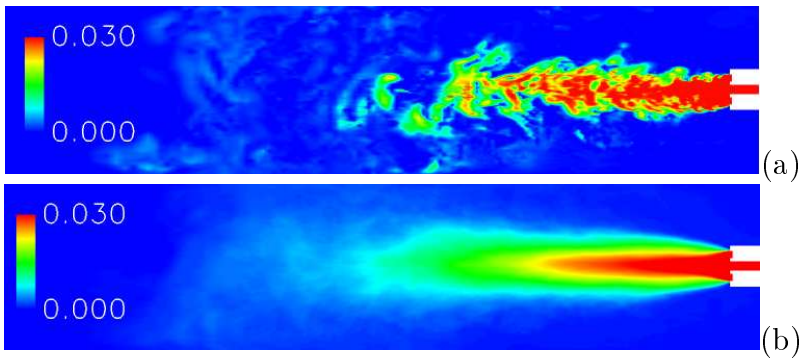

Figure 3.43: (a) Instantaneous and (b) time-averaged CH_4 mass fraction surface plot.

mm downstream of the inlet. This is followed by a very rapid increase of the axial velocity. The LEMLES overpredicts the axial velocity, whereas TANN-LES shows a slightly smaller values than the experimental data. Towards the stagnation plane, the TANN-LES is providing similar results with the EBU-LES and TF-LES.

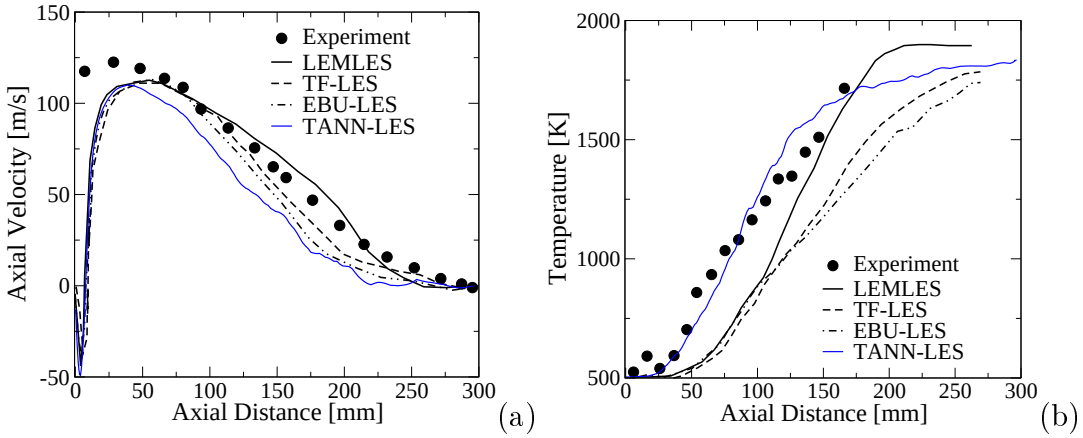

Figure 3.44: Comparison of the time-averaged (a) axial velocity and (b) temperature along the centerline.

The centerline variation of the temperature (Fig. 3.44b), however is somewhat different for each of the models. The TANN-LES, similar to the experimental data, predicts that the temperature monotonically increases starting at an axial distance of 25 mm. Both the location of the increase and the slope of the variation are captured by the TANN-LES. All the other models using the reduced 2-step kinetics, show that the temperature is constant almost up to 50 mm. The better agreement with data for the location of ignition by TANN-LES may be due to the more detailed kinetics employed.

Figures 3.45a-b show the centerline variation of the time averaged CH_4 and CO mole fraction. The plot for CH_4 shows that the TANN-LES approach agrees well

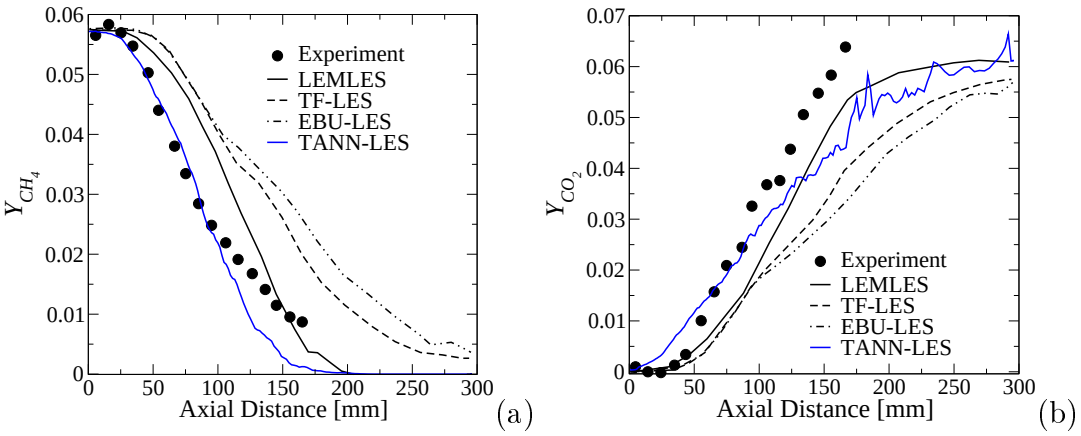

Figure 3.45: Comparison of the time-averaged (a) CH_4 and (b) CO_2 mole fraction along the centerline. Experiment, LEMLES, TF-LES and EBU-LES, from [1].

with the experimental data especially close to the injector (axial distance less than 100 mm.). The earlier LEMLES study showed that the fuel consumption starts at a point further downstream of the TANN-LES. Both TANN-LES and LEMLES show that the fuel is consumed completely at an axial distance of 175 mm. The EBU-LES and TF-LES exhibit a similar behavior in the near field and largely overpredict the experimental data. The centerline variation of the CO_2 mole fraction (Fig. 3.45b) is captured fairly well by using TANN-LES. The LEMLES and TANN-LES exhibit the same level of CO_2 mole fraction close to the stagnation plane.

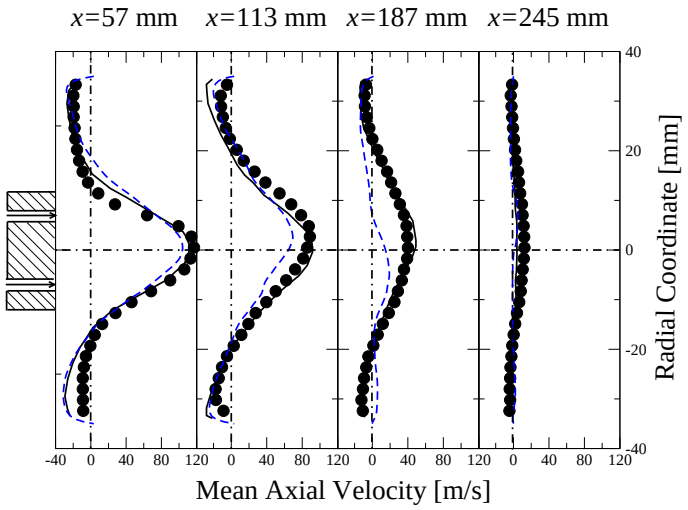

Figure 3.46: Comparison of the time-averaged axial velocity radial profiles at four sections. (•) Experiments, (—) LEMLES with DTSE and (- - -) TANN-LEMLES. Experiments and LEMLES from [1].

Figure 3.46 shows the radial variation of the mean axial velocity profiles at four

Table 3.13: Speed-up obtained for 12 steps methane skeletal mechanism.

	Species Equation	Time/(step×cell)	Speed-Up
TANN-LES	LES level	7.78×10^{-5}	134.9
LANN-LEMLES	LEM level (LES/12)	2.14×10^{-4}	49.2
DI-LEMLES	LEM level (LES/12)	1.05×10^{-2}	1.0

axial locations; x = 57, 113, 187 and 245 mm. For the sake of clarity, TF-LES and EBU-LES results are excluded for this figure, but their results were discussed earlier. At x =57 mm, the incoming jet can be seen in the center of the combustor, which has a peak velocity of 120 m/s. The velocity profile also exhibits negative axial velocity at the either edges, indicating the flow exiting the combustor. Here, it should be noted that the computational data exhibits a more symmetric profile than the experimental data. This is likely due to the slight misalignment of the inner tube within the annular injector in the experimental setup [1]. The TANN-LES tends to slightly underpredict the peak velocity profile in the centerline compared to the LEMLES and the experimental data. This is similar to what was observed earlier in Fig. 3.44a. Regardless the comparison of the LES with the experimental data shows good agreement.

3.4.3 Time and memory savings

The comparison of the speed-up obtained for the TANN-LES, LANN-LEMLES, and DI-LEMLES are given in Table 3.13. Although the results obtained by LANN-LEMLES are here, the speed-up obtained by this method is also included in the table for comparison purposes. LANN-LEMLES is 49.2 times faster than the direct integration method. This is much more than that of obtained for the syngas mechanism. The 12 step-16 species methane mechanism is much more stiffer than the syngas mechanism used in the study, hence the speed-up is much bigger. The speed-up obtained by the TANN-LES is even better. TANN-LES is 134.9 times faster than the DI-LES and clearly demonstrates the overall speed up that is possible using the TANN approach.

3.5 Conclusions

The accuracy of the TANN-LES approach is further investigated on a practical premixed combustor simulation. The simulations are performed on a grid and with test conditions used previously [1] except that in the current effort TANN-LES is for a more detailed 12-steps, 16-species reduced chemical kinetics mechanism (such stiff kinetics if included directly in LEMLES has a very large computational cost overhead). The current TANN-LES methodology can be provides better comparisons with the experimental data compared to the other subgrid models, again with a substantial reduction (by a factor of 135) in cost. It is determined that for stiffer mechanism the computational cost can be significantly reduced using the TANN-LES, and this

is possibly one key advantage of this method. Finally, although all the current studies have been exploring application of TANN in the LES environment, it is possible to consider a similar strategy for unsteady RANS (URANS) type of applications. However, this is an issue that will be addressed in another study.

3.6 LEMLES of LDI combustor with ANN chemistry

The proposed ANN methodology for calculating the instantaneous reaction rates at the sub-grid within the LEM framework is tested for the LEMLES of lean direct-injection (LDI) combustor. For a first step in this effort, the ANN is used to replace a relatively low-order three steps seven species reduced mechanism. Here it should be noted that the speed-up obtained from ANN is more pronounced for high order chemical kinetics mechanisms. Hence, for the reduced mechanism employed for this particular study there is almost no merit of using ANN. However, the main purpose of this step is to provide comparisons between the current ANN-LEMLES calculation and our previous simulations which were well documented and published [56, 57].

LDI has been of active interest due to its potential for low emissions at operational (high temperature, high pressure conditions [57]. In the LDI concept, the liquid fuel is injected from a venturi directly into the incoming swirling airstream, and the swirling air flow is used both for atomizing the injected liquid and for fuel air mixing. The venturi is followed by a short divergent diffuser section that ends at the dump plane. The base of the diffuser has a radius of 3.78×10^{-3} mm (L_1), where as the dump plane has a rectangular cross-section with a length of 12.61×10^{-3} m (L_2). Existing LES computations report η to be 18×10^{-3} mm.

3.6.1 ANN Training

The ANN training is achieved by using the methodology outlined previously in Section 3.1.2. The idea is essentially based on calculating the scalar field evolution on a one-dimensional line across the flame front by using the stand-alone LEM solver. The LEM computations are started for an initially laminar scalar field which is obtained from an opposed flow flame calculation. The integral length scale for the LEM computations is selected to be equal to $0.5\times R_0$ (R_0 =12.6 mm). Also, based on the range of turbulent Reynolds numbers observed in the previous LEMLES computations, the turbulent Reynolds number (Re_t) is varied between 10-400 In this manner, the effect of turbulence re-distributing the scalar gradients is achieved on eddies with a wide range of length-scales. A typical snapshot of scalar field variation along the one-dimensional line during the LEM computations is given in Fig 3.47 (a) for the fuel ($C_{12}H_{23}$). The initial variation of the fuel is also shown with dashed lines in the figure. As seen, the initial laminar data exhibits a smooth variation along the computational domain. LEM variation, however, is highly wrinkled due to the effect of turbulent eddies acting on the flame front. The flame is thickened by the turbulent eddies and there are multiple flame crossings along the one-dimensional LEM line.

Fig. 3.47 (b) shows the variation of the temperature with respect to the mixture fraction during the LEM computations. As seen in the graph, the states are well spread over the given scalar hyper-plane, denoting that the LEM can predict the effect of flame turbulence interaction somewhat similar to the actual process observed by the previous LES computations of the same combustor [57].

(a) Instantaneous snap-shot of the LEM level variation and the initial data.

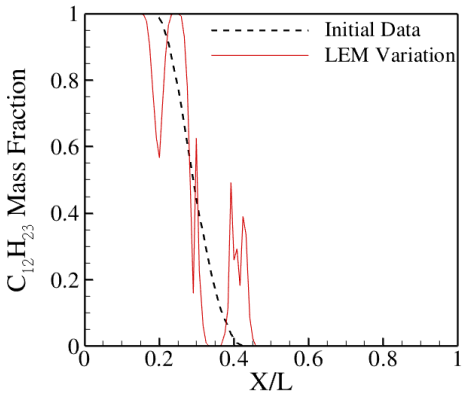

(b) Compositional state-space accessed by the stand-alone LEM.

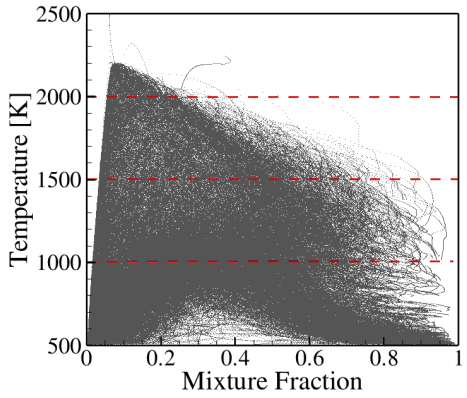

Figure 3.47: ANN training phase.

3.6.2 Results for LEMLES with ANN

In order to demonstrate the capability of using ANN for spray combustion in complex geometries, simulations were carried out on the Lean Direction Injection (LDI) rig that has been used in previous experimental and computational studies [56, 58]. The simulations were carried out using the block-structured, multidomain code used in the aforementioned computational work.

The simulations were initialized with a previous restart file where the flame structure had developed, but convergence had not yet been acheived. Averaged statistics were computed for 20000 iterations which is approximately twice the characteristic time, τ, where τ is defined as the time necessary for one rotation of the precessing vortex core. Although this is not nearly long enough for convergence, the objective of the simulation was to determine any issues arising from the implementation of the ANN into a complex geometry, not to obtain statistically significant results. The preliminary ANN results are compared with results obtained using indirect integration (i.e., evaluation of the kinetics) with five chemistry time steps per Eulerian time

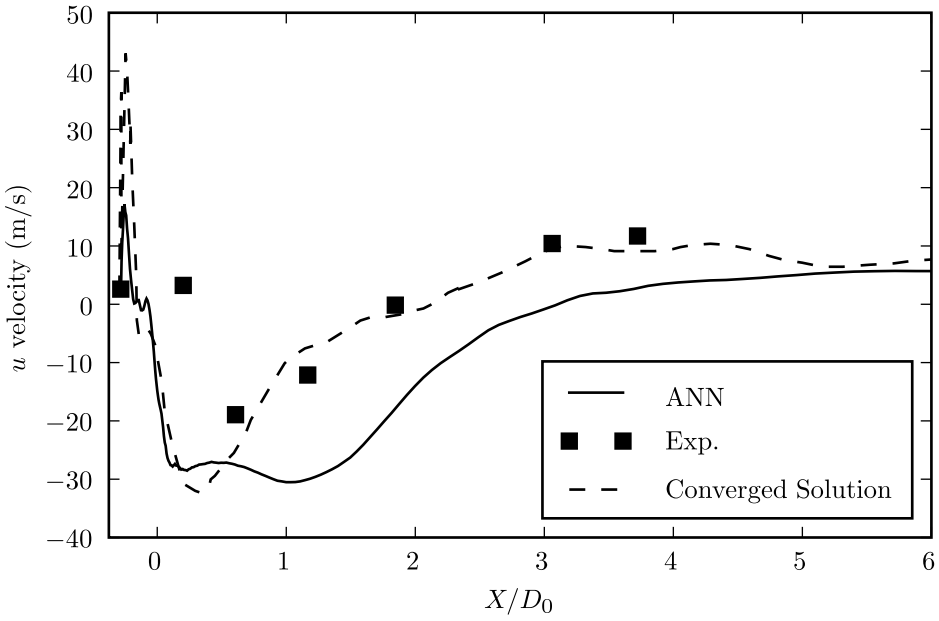

Figure 3.48: Time-averaged centerline axial velocity

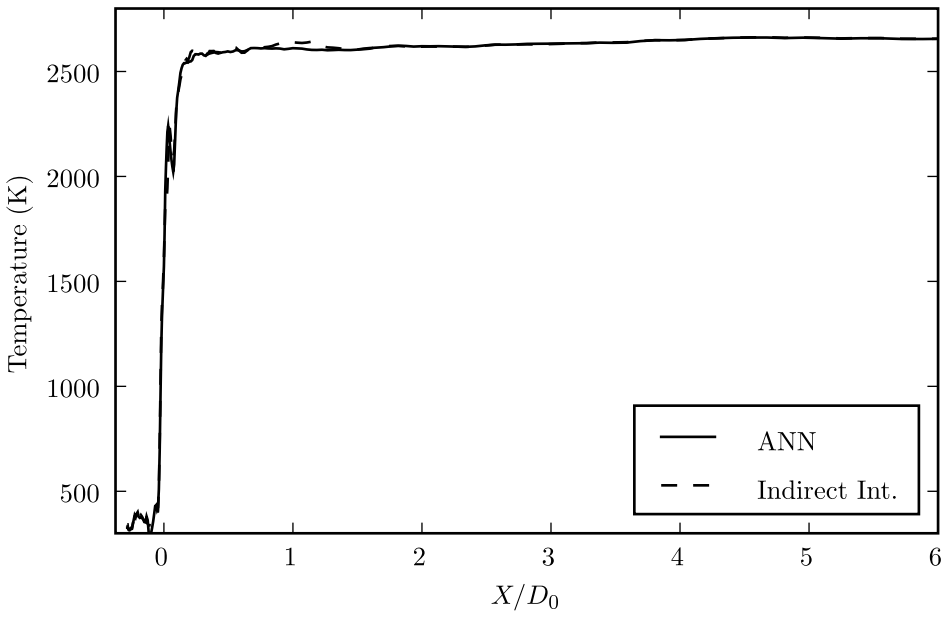

Figure 3.49: Instantaneous centerline temperature

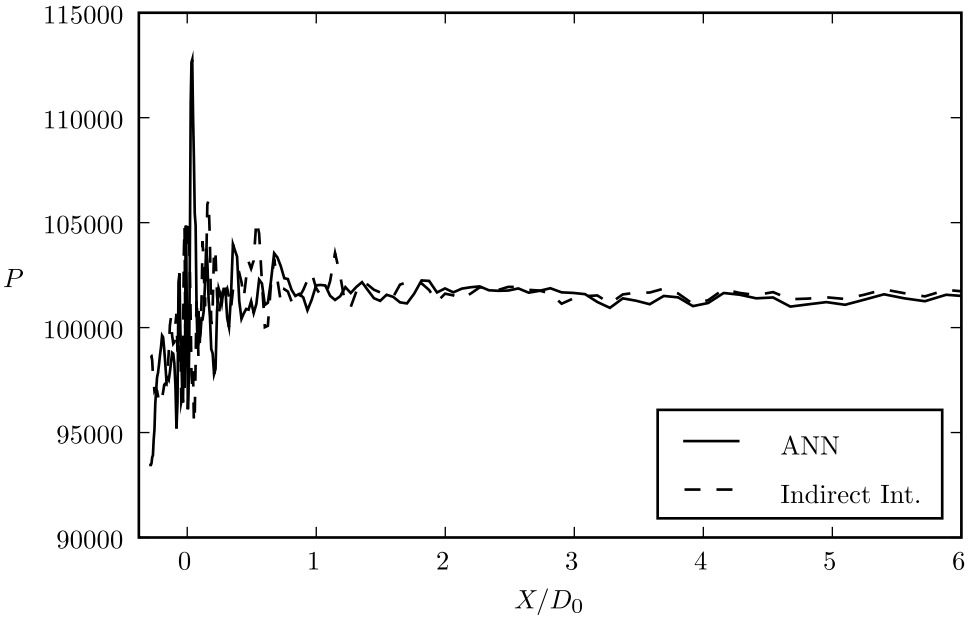

Figure 3.50: Instantaneous centerline pressure

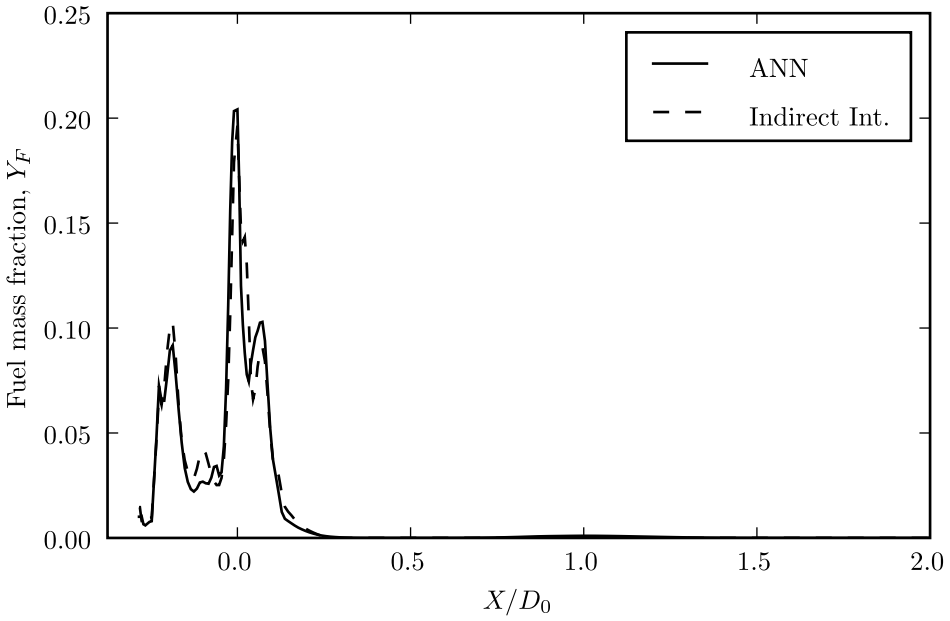

Figure 3.51: Instantaneous centerline fuel mass fraction

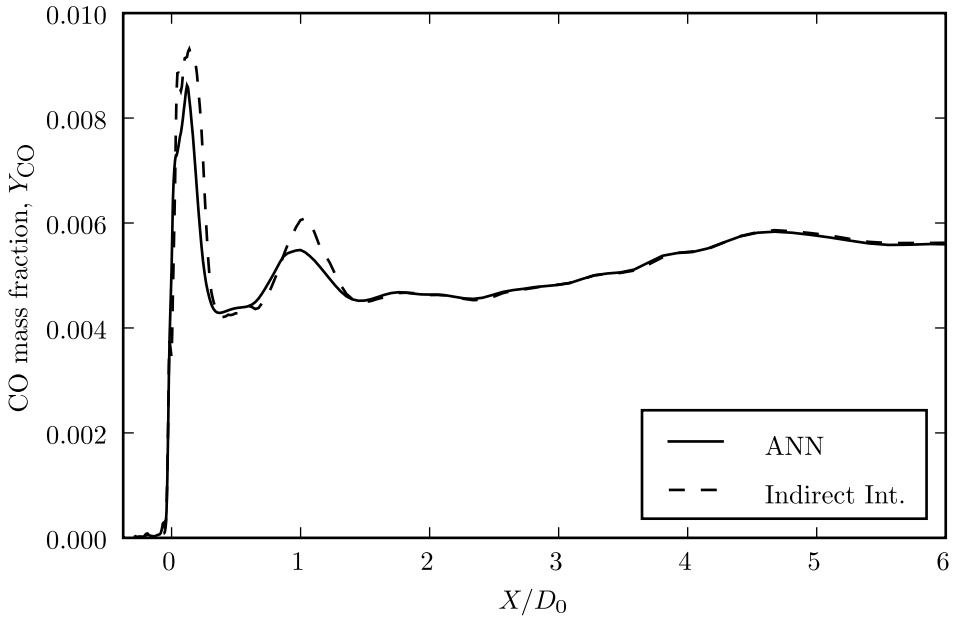

Figure 3.52: Instantaneous centerline CO mass fraction

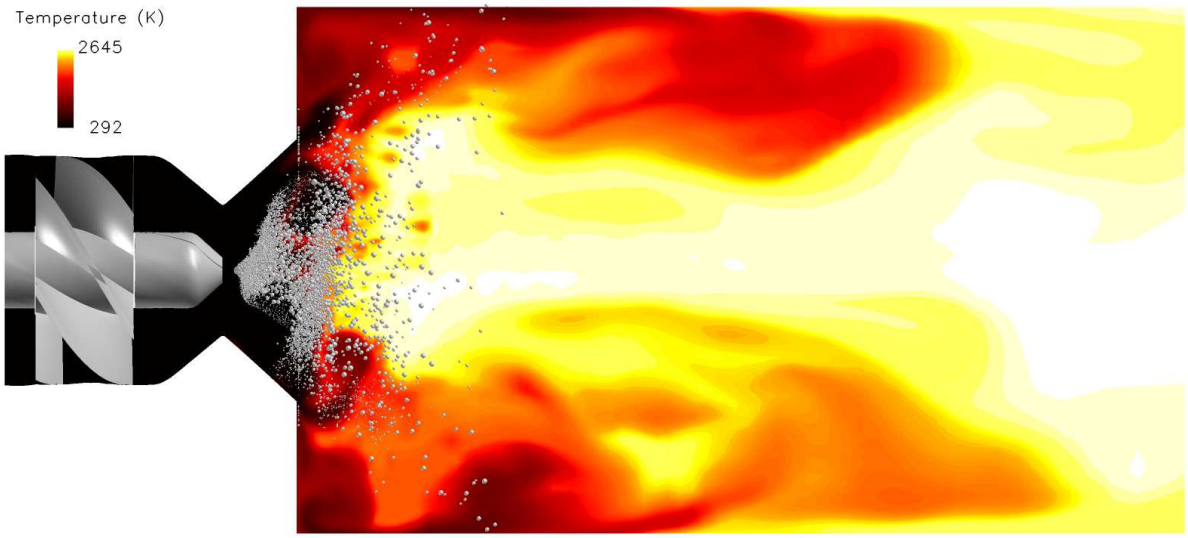

Figure 3.53: LEMLES with ANN: temperature contours and fuel droplets after 1τ

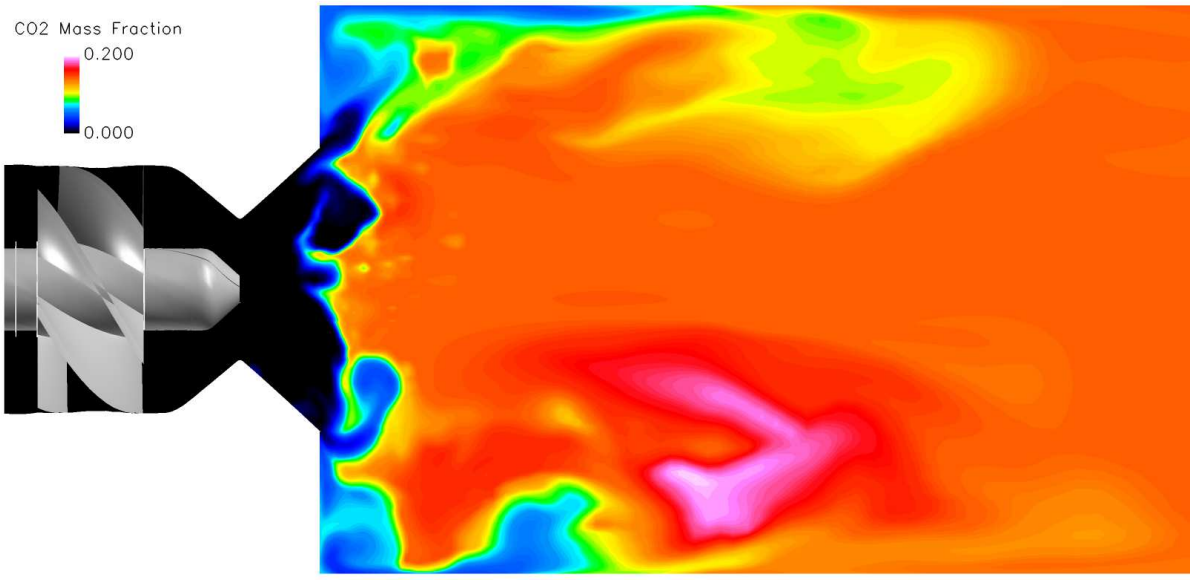

Figure 3.54: LEMLES with ANN: CO_2 mass fraction after 1τ

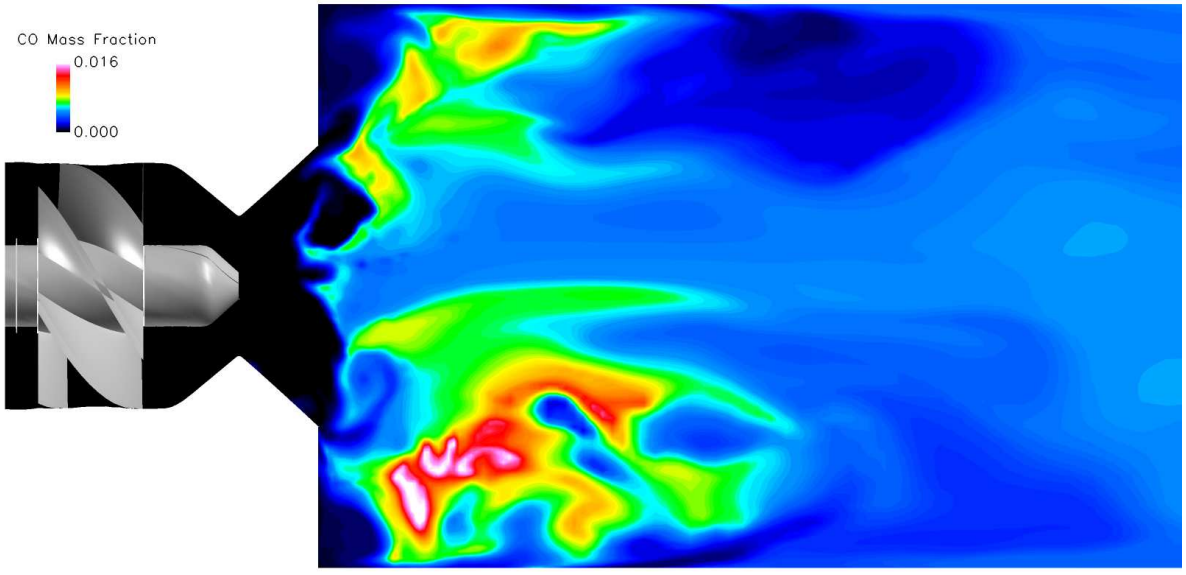

Figure 3.55: LEMLES with ANN: CO mass fraction after 1τ

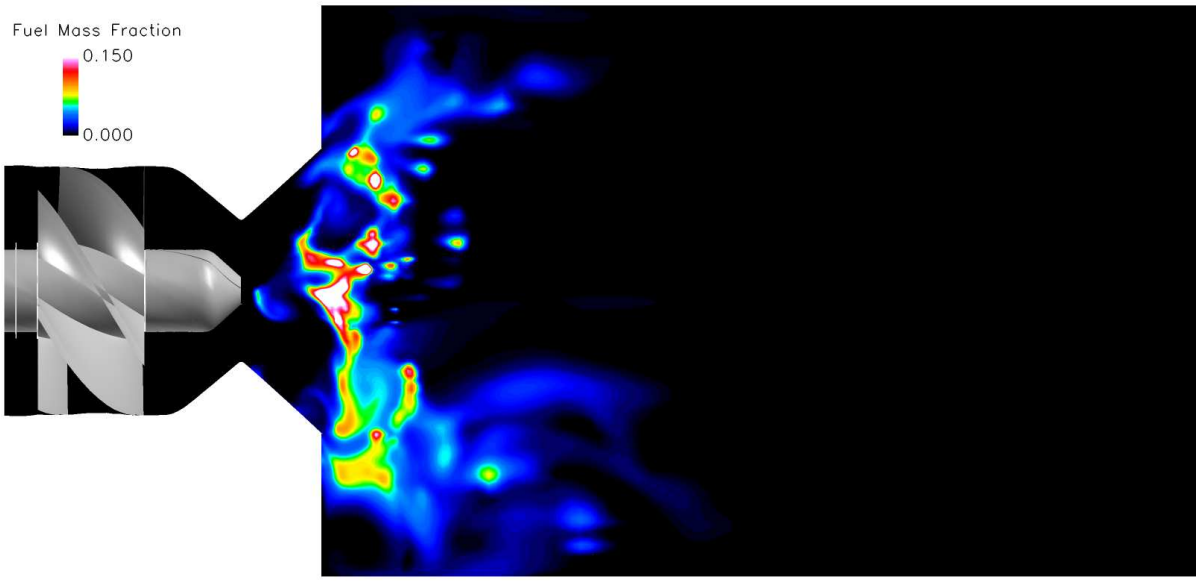

Figure 3.56: LEMLES with ANN: Fuel mass fraction after 1τ

step as well as with experimental data. The results for the indirect integration are shown for an averaging period of 21τ, and thus, they match more closely with the experimental results.

The simulation with the ANN has only run out to one flow through time whereas the previous solution had been simulated substantially more. Further simulation is underway but here we show some preliminary results for the ANN-LES. Instantaneous comparisons of the ANN and indirect integration methods are given in Figures 3.49–3.52 for temperature, pressure, fuel mass fraction and CO mass fraction after one characteristic time. The data is very consistent between the ANN and indirect integration results. ANN performs well for both the global heat release rate, as indicated by the temperature profile, as well as the intermediate reactions evidenced by the CO mass fraction plot.

It must be emphasized that ANN is only used for the chemistry calculation within the large eddy simulation linear eddy mixing (LEMLES) modeling framework. The contour plots in Figs. 3.53–3.56 are snapshots of the LEMLES with ANN results taken at the same time as the axial line plots. The figures are representative of the time-accurate wrinkled flame structure that can be captured with LES but would be lost with a time-averaged numerical scheme.

The outcome of these simulations indicate that although there are still areas relating to the implementation of ANN for spray combustion in complex geometries that need to be addressed, ANN can be a feasible replacement for other chemical reaction rate solution methods.

3.7 Kinetic Eddy Simulation of a Lean Direct Injection Combustor

The kinetic eddy simulation (KES) method was used to simulate cold flow of a lean direct injection (LDI) combustor. Simulations were carried out on a multiblock grid with 72 blocks containing nearly 1.5 million grid points, seen in Figure 3.57, utilizing the rtjones computing cluster. Initial simulations proved to be difficult due to the

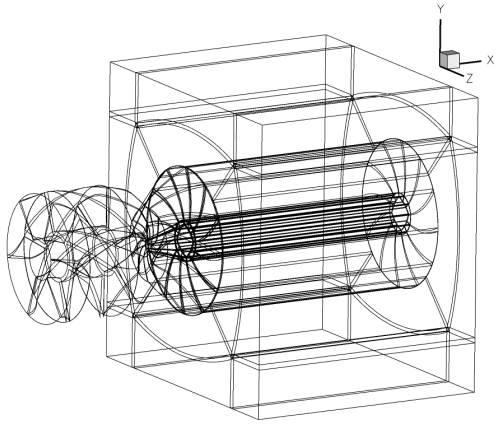

Figure 3.57: Multiblock LDI combustor grid

calculation of ℓ^{sgs} which causes problems in areas where the subgrid kinetic energy approaches zero. This causes the subgrid length scale, and thus the turbulent eddy viscosity, to become very large. In order to avoid the unbounded growth of ℓ^{sgs}, a limiter must be used. Initially the subgrid length scale was limited to $\ell^{sgs}/\overline{\Delta} \leq 200$, however this did not stabilize the solution for the LDI near the walls of the swirler vanes. Figure 3.58 shows the ℓ^{sgs} profile near the wall in the swirler vanes. At the

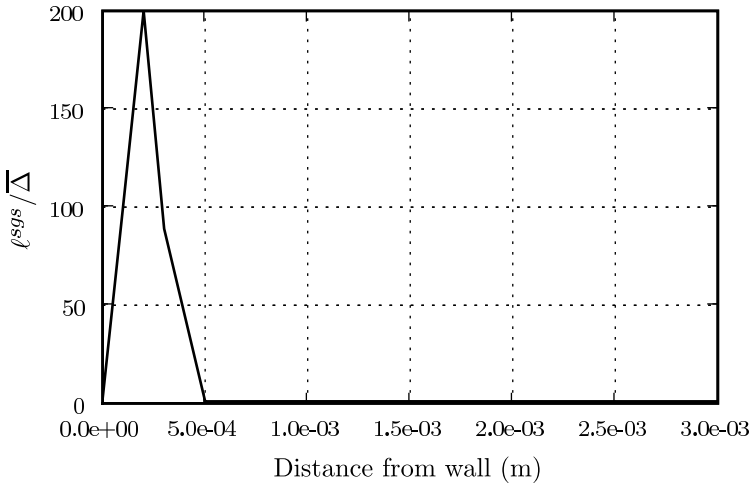

Figure 3.58: Subgrid length scale near walls without proper limiting

upper limit, the subgrid length scale should tend toward the integral length scale,

which is determined by the geometry of the flow. Because of this, a subgrid length scale limiter based on geometrical constraints was used, such that $\ell^{sgs} \leq 2y$, where y is the normal wall distance. This value was chosen based on channel flows, roughly approximating a swirler vane, where the largest eddies in the flow are the size of the channel height. Figures 3.59(a) and 3.59(b) show ℓ^{sgs} and $\ell^{sgs}/\overline{\Delta}$, respectively, using the modified limiter. The profiles shown are at an axial position downstream of the swirler vanes in the diffuser section. In areas where $\ell^{sgs}/\overline{\Delta} = 1$ the simulation provides the same results as the traditional LES and where $\ell^{sgs}/\overline{\Delta} > 1$ the solution is comparable to that of a very large eddy simulation (VLES). Figure 3.59(b) indicates that near the wall the solution is limited based on geometric and stability constraints before transitioning to a region of LES-like behavior and finally to VLES near the centerline. Figure 3.60 shows areas of both VLES and LES in the swirler vane region.

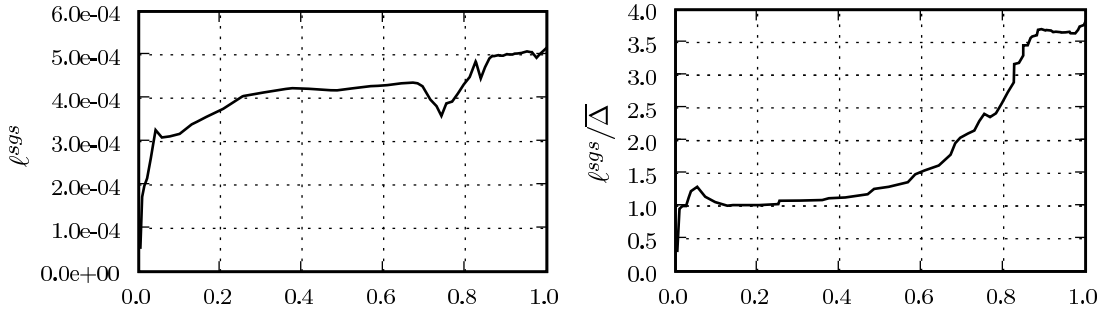

(a) Subgrid length scale, ℓ^{sgs} (b) $\ell^{sgs}/\overline{\Delta}$

Figure 3.59: Subgrid length scale and $\ell^{sgs}/\overline{\Delta}$ profiles in the swirler region with near-wall limiting

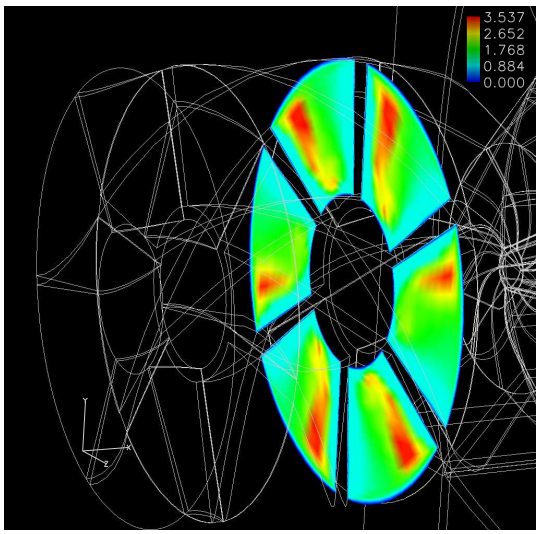

Figure 3.60: $\ell^{sgs}/\overline{\Delta}$ in the swirler vane region

CHAPTER IV

CONCLUSIONS

The report discusses calculating instantaneous chemical source terms in multi-step, multi-species reaction kinetics mechanism based on the ANN method. The ANN training is achieved by stand-alone LEM simulations, where the unsteady interaction of small-scale structures with a laminar flame front is captured. The first section of the report deals with evaluating the proposed methodology for canonical flame studies. The first test case (Case A) is a series of LEMLES of premixed flame-turbulence-vortex interaction computations, where ANN is used to replace DI in the sub-grid LEM model. Cases B-C provided *a priori* ANN testing in the stand-alone LEM computations by evaluating the ANN predictions inside and outside the compositional state-space that it was trained for. The LEM computations are carried out and used for ANN training for the composition of interest in the LEMLES. Thus, this strategy has te potential for developing ANNs independent of the geometry of interest. In the second secsion, the proposed ANN methodology is applied to the LES of LDI combustor study.

The LES studies of the canonical flames demonstrate that the current ANN approach is capable of detecting the correct species evolution calculated by the DI. Also, while results by L-ANN and F-ANN are comparable to each other, the P-ANN approach provides the worst predictions. This confirms that the ANN accuracy is strongly affected by the look-up table used for ANN training. The table constructed based on laminar flame calculations lacks the *unsteady* mixing effect caused by turbulent structures, and therefore, is not suitable for ANN training. This effect is included both in the 3D simulation of FVI and in the stand-alone LEM calculations, which leads to accurate ANN predictions.

The thermo-chemical database constructed through LEM does not contain all the states accessed during the computation. Thus, the ANN ability to predict states that it was not trained for (so-called *generalizibility*) is adressed by using ANN within the stand-alone LEM computations to replace DI, and simulating conditions outside the training base. Results obtained by Case B for a premixed methane/air flame demonstrates that the LEM with ANN is indistinguishable from the LEM with DI. The same behavior is observed for a non-premixed syngas/air LEM simulation (Case C). The ANN ability to predict the LEM evolution for a Re_t that is not included in the database is also adressed in Case C, and again, the results are satisfactory.

The ANN speed-up against DI is shown to be highly dependent on the stiffness of the reduced mechanism used to calculate the chemical source terms. For Case A, the ANN provided approximately 11X speed-up compared to DI, whereas for Case C, the speed-up is around 4-5X. This is related to the less stiffer mechanism used for Case C. It should be noted that the maximum speed-up that can be obtained for Case C is only 5X. The reason for achieving lesser speed-up than Case A, is that the reduced

mechanism used for this case is not as stiff as it is for Case A. Among the cases considered in the report, the maximum speed-up is obtained for Case B (35X), since the methane skeletal mechanism used here is much stiffer than the syngas mechanism. Regardless of the speed-up, for all cases there is huge memory saving, e.g., for Case C, the look-up table size is 3.18 GB, whereas only 0.1 MB is needed for the ANN.

To reduce the computational costs further the above apporach is adapted for LES simulations where the filtered reaction rate is directly computed from ANN kinetics in an approach called TANN. Since the subgrid LEM equations are not solved in lieu of the LES species transport equations, and the online solution of stiff-ODEs for multistep kinetics are avoided, the computational gains are significant. To test this approach, the DNS results from Case C (non-premixed syngas/air) are again validated against, for three cases. These cases L, M and H represent respectively, the low, medium and high Reynolds number based configurations. TANN shows the ability to capture the extinction/reignition phenomenon for all three cases satisfactorily. Furthermore, the TANN-LES is almost 18 times faster than the conventional LEMLES approach. The LANN-LEMLES, on the other hand provides a speed-up of 5.5 times compared to the LEMLES using a stiff ODE solver. The TANN used filtered values from the stand-alone LEM table, which resulted in a training table of 372 MB. The same database (without filtering) was used in our previous study to train the LANN, which was 3.18 GB [2], which is considerably bigger than the current table.

The accuracy of the TANN-LES approach is further investigated on a practical premixed combustor simulation. The simulations are performed on a grid and with test conditions used previously [1] except that in the current effort TANN-LES is for a more detailed 12-steps, 16-species reduced chemical kinetics mechanism (such stiff kinetics if included directly in LEMLES has a very large computational cost overhead). The current TANN-LES methodology can be provides better comparisons with the experimental data compared to the other subgrid models, again with a substantial reduction (by a factor of 135) in cost. It is determined that for stiffer mechanism the computational cost can be significantly reduced using the TANN-LES, and this is possibly one key advantage of this method.

The LDI simulation with ANN kinetics provides reasonable results when compared with the experimental and previous computational studies of the same combustor [57]. However, the simulation has not yet run long enough to obtain statistical time averaged results, and this will be investigated in more detail in the future.

The kinetic eddy simulation (KES) model, defined by the addition of a second subgrid turbulence equation for $(k\ell)^{sgs}$, is studied for LES. The second equation provides a method for the explicit calculation of the subgrid length scale allowing for an automatic bridging between LES and VLES results, independent of the grid. The subgrid length scale and thus the subgrid turbulent eddy viscosity are continuous functions independent of the filter width. This model was intially applied to a LDI combustor to determine its feasibilty and will be applied to canonical problems in the future. Near-wall limiters on the subgrid length scale were investigated to stabilize the numerical result based on geometric constraints. A limiting value of $\ell^{sgs} \leq 2y$ where y is the normal distance to the wall proved more effective than previous limiters

based on ad-hoc limiting values.

CHAPTER V

FUTURE WORK

Accurate representation of the chemical kinetics with the ANN methodology requires a well established learning algorithm and training table construction strategy. Several different techniques of creating thermo-chemical database representative of the physical processes occurring in the actual problem of interest was developed and documented in our previous reports. The current report dealt with creating the database based on stand-alone LEM computations for premixed flames, and assessing the accuracy of each different ANNs trained on different tabulation tecnique. The next step in this effort would be to apply the current ANN training methodology to a non-premixed test case. Also extracting the filtered reaction rate information from the stand-alone LEM computations is needed, which can be, again, used to speed-up the LES of reactive flow computations if used together with the ANN methodology. The simulations for these two steps are underway and the results will be provided in the next report.

Several steps must be taken to improve the LDI-ANN results. The first will be to implement the ANN routines into the current multiblock-structured code. This code is improved over the previous version in many ways, most notably the current code facilitates the use of larger processor counts and contains a more efficient Lagrangian phase implementation. An updated LDI grid that contains 3.65 million cells will be used for all new simulations, which is shown in Figure 5.1. Since more processors can be used as compared with previous efforts, simulation turnaround time should be comparable. The LEMLES with ANN for the single LDI configuration will be continued until convergenced is reached to fully evaluate the impact of the chemistry model.

The accuracy of the ANN results depends on the conditions used during the training process. Well-established training methods are available for premixed and non-premixed single phase combustion but not for spray combustion. New baseline spray combustion simulations will be performed on simple geometry to provide more accurate input data to the ANN training module.

To test the capabilities of the multiblock code, LES of the 9 injector LDI rig will be investigated. Experimental and RANS simulation data exists for this setup but currently no LES has been completed [59]. A grid for this study is shown in Figure 5.2, which contains around 19 million cells. Figures 5.3 and 5.4 show the clustering at the dump plane and at a location of $x/D_0 \approx 2$, respectively. The grid is intially clustered near the injector cup walls but quickly spreads out to near uniform spacing to capture the injector-to-injector interations accurately. Preliminary coldflow simulations have been completed and reacting flows can quickly be started once sufficient computational resources have been made available. TANN will be used for reacting flows in order to keep the computational cost reasonable yet maintain

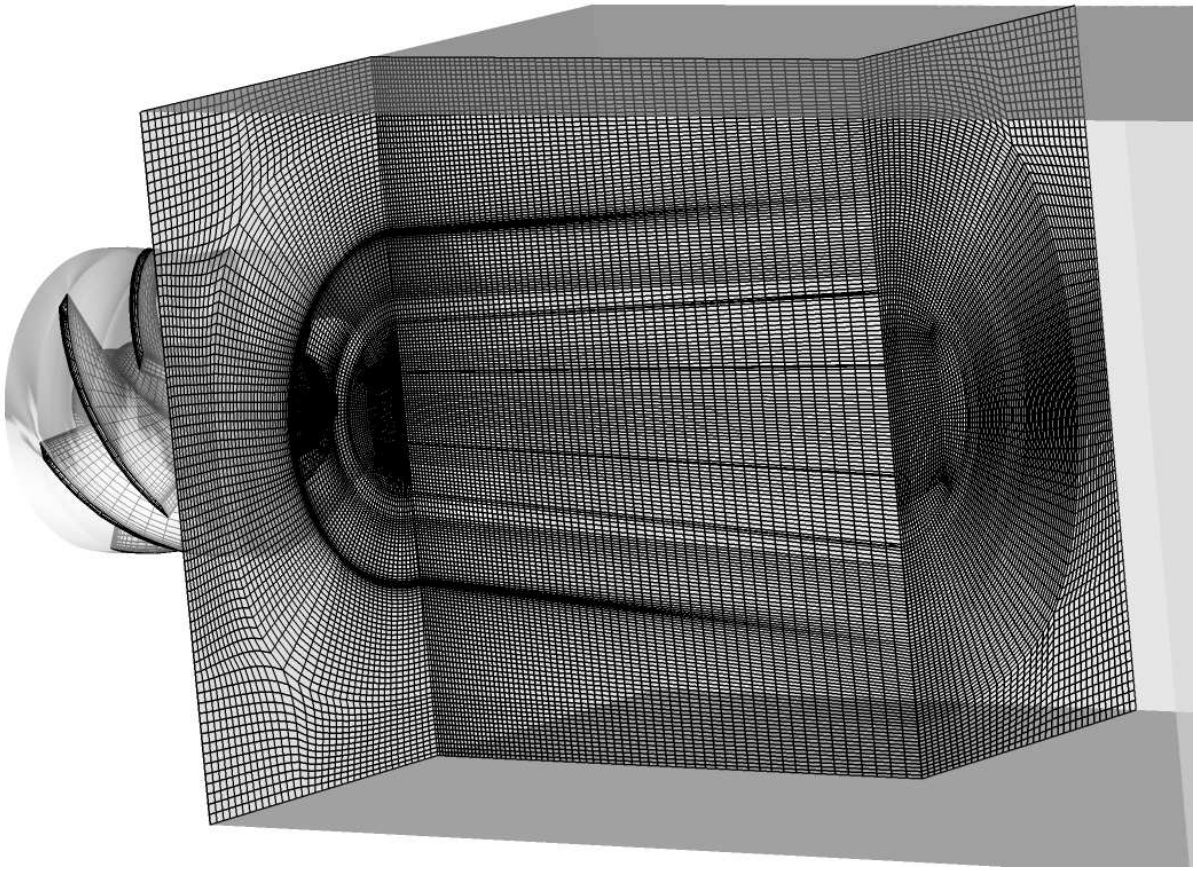

Figure 5.1: Updated LDI grid with 3.65 million cells

accuracy.

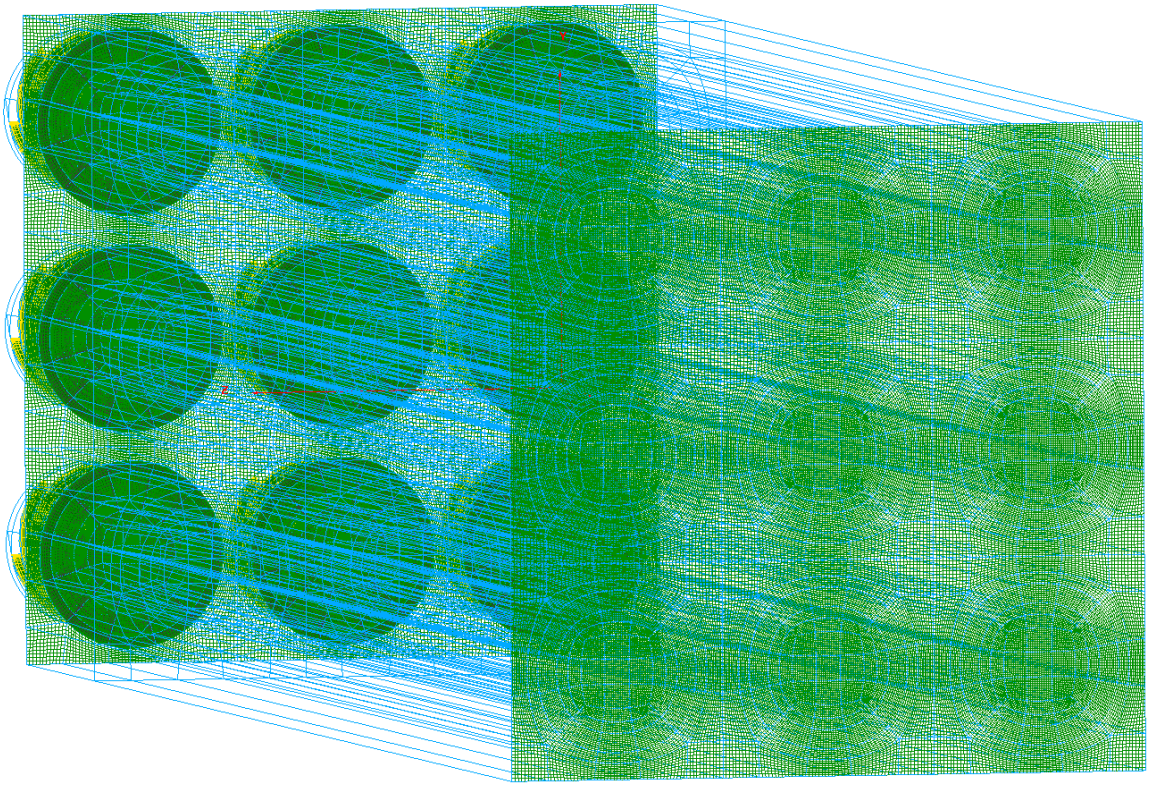

Figure 5.2: 9 injector LDI grid with 19 million cells

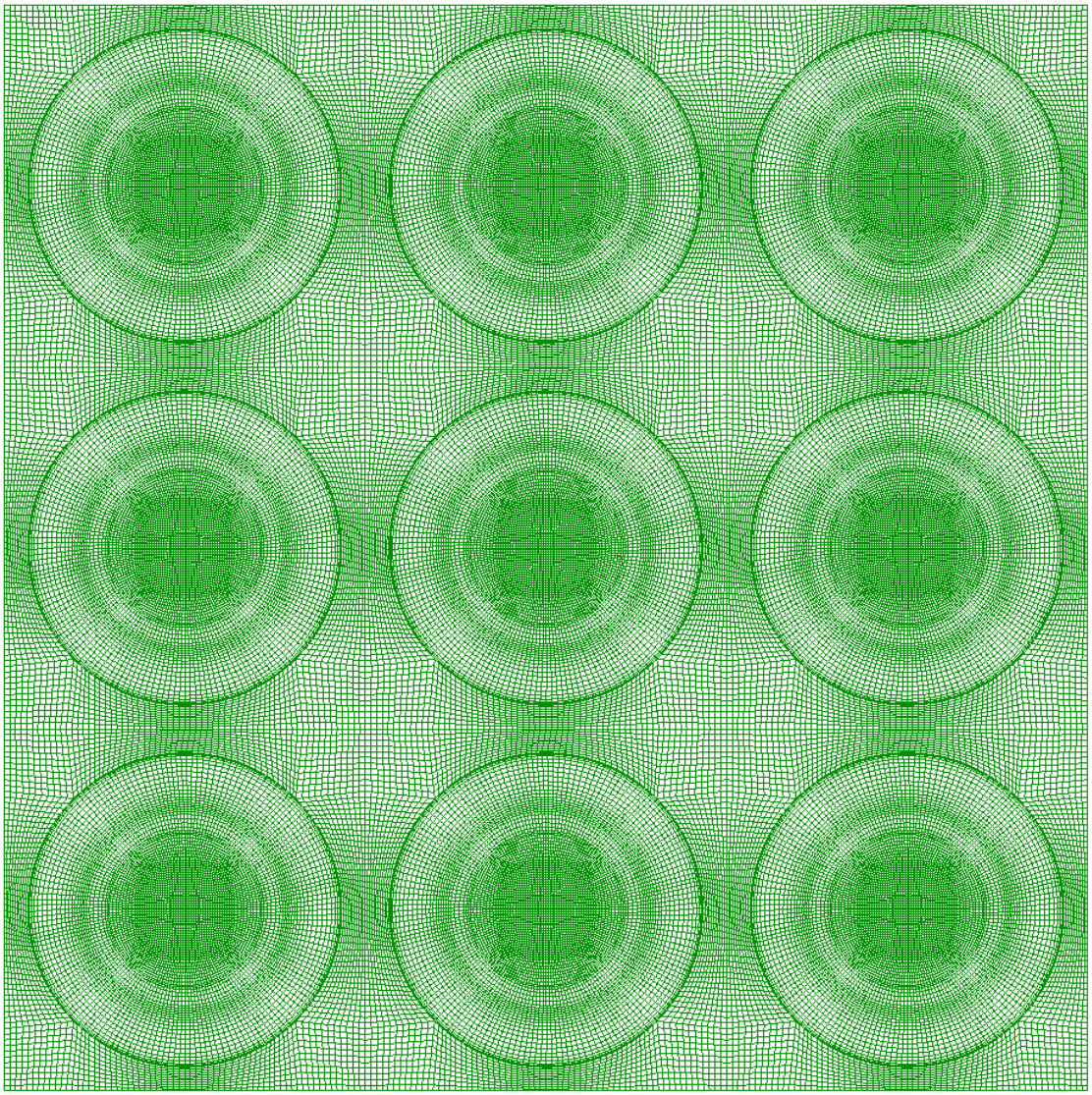

Figure 5.3: 9 injector LDI grid clustering at the dump plane

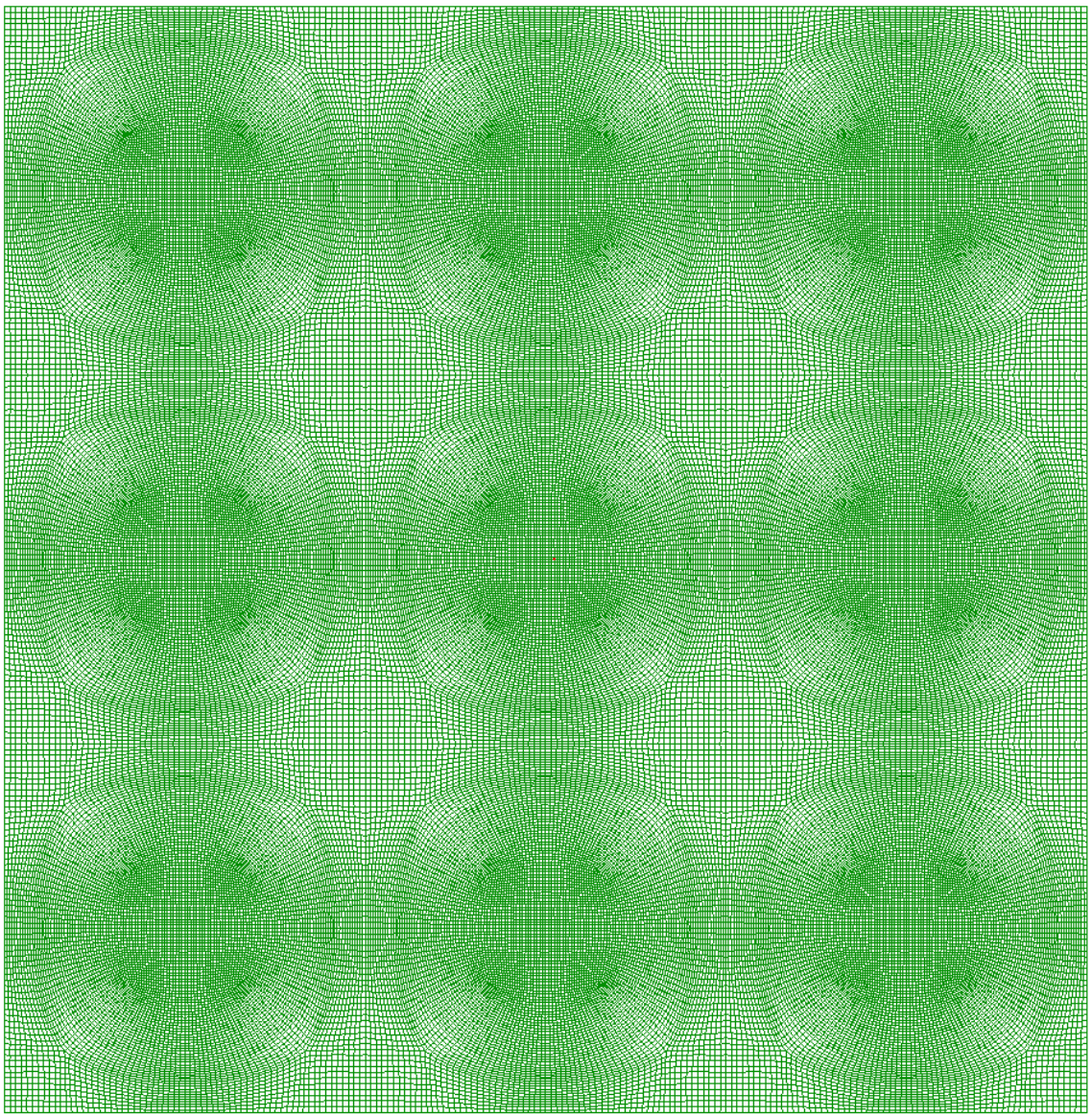

Figure 5.4: 9 injector LDI grid clustering at $x/D_0 \approx 2$

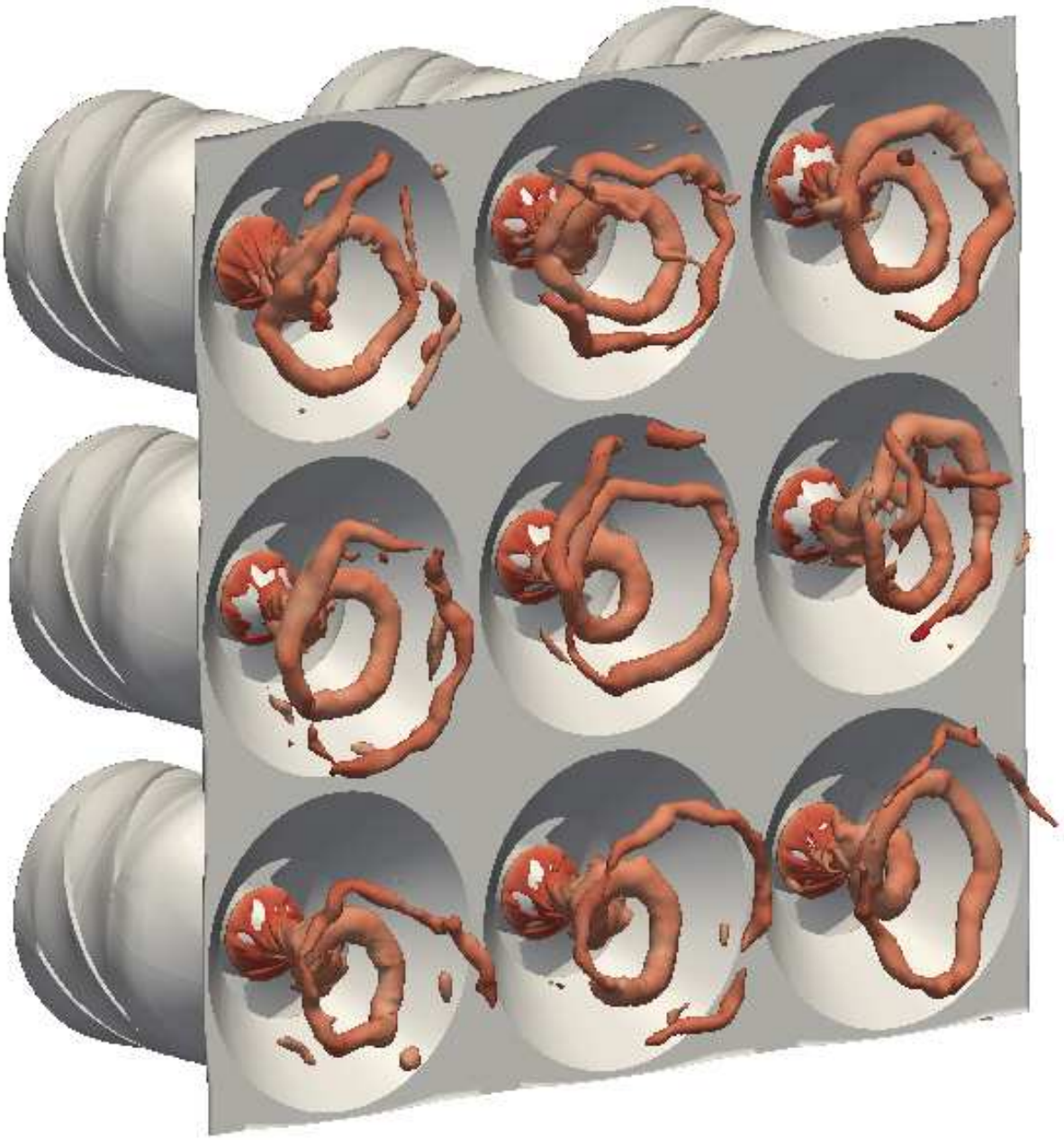

Figure 5.5: 9 injector LDI instantaneous density contour for cold flow simulation

Bibliography

[1] S. Undapalli, S. Srinivasan, and S. Menon. Les of premixed and non-premixed combustion in a stagnation point reverse flow combustor. *Proc. Combust. Inst.*, 32:1537–1544, 2009.

[2] B.A. Sen, E.R. Hawkes, and S. Menon. Large eddy simulation of extinction and reignition with artificial neural networks based chemical kinetics. *Combust. Flame*, 157:566–578, 2010.

[3] B. A. Sen and S. Menon. Artificial neural networks based chemistry-mixing subgrid model for les. *AIAA-2009-0241*, 2009.

[4] B. A. Sen and S. Menon. Turbulent premixed flame modeling using artificial neural network based chemical kinetics. *Proc. Combust. Inst.*, 32:1605–1611, 2009.

[5] T.J. Poinsot and D. Veynante. *Theoretical and Numerical Combustion*. Edwards, Inc., second edition, 2005.

[6] S. B. Pope. *Turbulent Flow*. Cambridge Book Company, first edition, 2000.

[7] J. Xu and H. Pope. Pdf calculations of turbulent nonpremixed flames with local extinction. *Combust. Flame*, 123:281–307, 2000.

[8] R. R. Cao and S. Pope. The influence of chemical mechanisms on pdf calculations of nonpremixed piloted jet flames. *Combust. Flame*, 143:450–470, 2005.

[9] J. Warnatz, U. Maas, and R. W. Dibble. *Combustion:Physical and Chemical Fundamentals, Modeling and Simulation, Experiments, Pollutant Formation*. Springer, 2006.

[10] J. Y. Chen, W. Kollmann, and R. W. Dibble. The mechanism of two-dimensional pocket formation in lean premixed methane-air flames with implictaions to turbulent combustion. *Combust. Sci. Technol.*, 64:315–347, 1989.

[11] U. Maas and S. B. Pope. Simplifying chemical kinetics: Intrinsic low-dimensional manifolds in the composition space. *Combust. Flame*, 88:239–264, 1992.

[12] S. B. Pope. Computationally efficient implementation of combustion chemistry using in situ adaptive tabulation. *Combust. Theory Modelling*, 1:41–63, 1997.

[13] G. Eggenspieler and S. Menon. Combustion and emission modeling near lean blow-out in gas turbine engines. *Prog. Comp. Fluid Dyn.*, 5(6):281–297, 2005.

[14] A. R. Kerstein. Linear-eddy model of turbulent scalar transport and mixing. *Combust. Sci. Tech.*, 60:391–421, 1988.

[15] A. R. Kerstein. Linear-eddy modeling of turbulent transport. part 6. microstructure of diffusive scalar mixing fields. *Journal of Fluid Mechanics*, 231:361–394, 1991.

[16] A. R. Kerstein. Linear-eddy modeling of turbulent transport. part 4. structure of diffusion-flames. *Combust. Sci. Tech.*, 81:75–86, 1992.

[17] T.M. Smith and S. Menon. One-dimensional simulations of freely propagating turbulent premixed flames. *Combust. Sci. and Tech.*, 128:99–130, 1996.

[18] V.K. Chakravarthy and S. Menon. Linear-eddy simulations of reynolds and schmidt number dependencies in turbulent scalar mixing. *Physics of Fluids*, 13:488–499, 2001.

[19] V. Sankaran, T. G. Drozda, and J. C. Oefelein. A tabulated closure for turbulent non-premixed combustion based on the linear eddy model. *Proc. Combust. Inst.*, 32:1571–1578, 2009.

[20] C. Christodoulou and M. Georgiopoulos. *Applications of Neural Networks in Electromagnetics*. Artech House, 2000.

[21] K. Mehrotra, C. K. Mohan, and S. Ranka. *Elements of Artificial Neural Networks*. MIT Press, 1997.

[22] J. A. Blasco, N. Fueyo, C. Dopazo, and J. Ballester. Modelling the temporal evolution of a reduced combustion chemical system with an artificial neural networks. *Combust. Flame*, 123:38 – 52, 1998.

[23] J. A. Blasco, N. Fueyo, J. C. Larroya, C. Dopazo, and J. Y. Chen. A single-step time-integrator of a methane-air chemical system using artificial neural networks. *Comput. Chem. Eng.*, 23:1127 – 1133, 1999.

[24] Y. Choi and J.-Y. Chen. Fast prediction of start-of-combustion in hcci with combined artificial neural networks and ignition delay model. *Proc. Combust. Inst.*, 30:2711–2718, 2005.

[25] J. Y. Chen, J. A. Blasco, N. Fueyo, and C. Dopazo. An economical strategy for storage of chemical kinetics:fitting *insitu* adaptive tabulation with artificial neural networks. *Proc. Combust. Inst.*, 28:115–121, 2000.

[26] R. Kapoor, A. Lentati, and S. Menon. Simulations of methane-air flames using isat and ann. *AIAA-01-3847*, 2001.

[27] A. Kempf, F. Flemming, and J. Janicka. Simulation of soot formation in turbulent premixed flame. *Proc. Combust. Inst.*, 30:557 – 565, 2005.

[28] R. (Ed.) Barlow. *Proceedings of the TNF Workshops*. Sandia National Laboratories, Livermore, CA, 2005. www.ca.sandia.gov/TNF.

[29] M. Ihme, C. Schmitt, and H. Pitsch. Optimal artificial neural networks and tabulation methods for chemistry representation in les of a bluff-body swirl-stabilized flame. *Proc. Combust. Inst.*, 32:1527–1535, 2008.

[30] David C. Wilcox. DCW Industries, Inc., third edition, 2006.

[31] Y. Fang and S. Menon. A two-equation subgrid model for large-eddy simulation of high reynolds number flows. *AIAA-2006-116*, 2006.

[32] B. A. Sen and S. Menon. Large-eddy simulations of turbulent flames in syn-gas fuel-air mixtures. *AIAA-2007-1435*, 2007.

[33] B. A. Sen and S. Menon. Representation of chemical kinetics by artificial neural networks for large eddy simulations. *AIAA-2007-5635*, 2007.

[34] E. R. Hawkes, R. Sankaran, J. C. Sutherland, and J. H. Chen. Scalar mixing in direct numerical simulations of temporally evolving plane jet flames with skeletal co/h2 kinetics. *Proceedings of the Combustion Institute*, 31:1633–1640, 2007.

[35] E. R. Hawkes, R. Sankaran, J. H. Chen, S. A. Kaiser, and J. H. Frank. An analysis of lower-dimensional approximations to the scalar dissipation rate using direct numerical simulations of plane jet flames. *Proceedings of the Combustion Institute*, 32:1455–1463, 2009.

[36] M. Ihme, A. L. Marsden, and H. Pitsch. Generation of optimal artificial neural networks using a pattern search algorithm: Application to approximation of chemical systems. *Neural Computation*, 20:573–601, 2008.

[37] P Sripakagorn, S Mitarai, G Kosaly, and H Pitsch. Extinction and reignition in a diffusion flame: a direct numerical simulation study. *Journal of Fluid Mechanics*, 518:231–259, 2004.

[38] C. Pantano. Direct simulation of non-premixed flame extinction in a methane-air jet with reduced chemistry. *J. Fluid Mech.*, 514:231–270, 2004.

[39] S. R. Turns. *An Introduction to Combustion*. McGraw-Hill, 2000.

[40] J. Xu and S.B. Pope. Pdf calculations of turbulent nonpremixed flames with local extinction. *Combust. Flame*, 123:281–307, 2000.

[41] B.A. Sen and S. Menon. Representation of chemical kinetics by artificial neural networks for large eddy simulations. AIAA-07-1435, 45th Aerospace Sciences Meeting and Exhibit, 2007.

[42] C.M. Vagelopoulos and F.N. Egolfopoulos. Laminar flame speeds and extinction strain rates of mixtures of carbon monoxide with hydrogen, methane, and air. *Proc. Combust. Inst.*, 25:1317–1323, 1994.

[43] L. Su and N. Clemens. The structure of fine-scale scalar mixing in gas-phase planar turbulent jets. *J. Fluid Mech.*, 488:1–29, 2003.

[44] D. Veynante and L. Vervisch. Turbulent combustion modeling. *Prog. in Energy and Combust. Sci.*, 28:193–266, 2002.

[45] B.A. Sen and S. Menon. Linear eddy mixing based tabulation and artificial neural networks for large eddy simulations of turbulent flames. *Combust. Flame*, 157:62–74, 2010.

[46] B.A. Sen and S. Menon. Turbulent premixed flame modeling using artificial neural networks based chemical kinetics. *Proc. Combust. Inst.*, 32:1606–1611, 2009.

[47] S. Mitarai, G. Kosaly, and J.J. Riley. A new lagrangian flamelet model for local extinction and reignition. *Combust. Flame*, 137:306–319, 2004.

[48] D. Veynante and L. Vervisch. Turbulent combustion modeling. *Progress in Energy and Combustion Science*, 28:193–266, 2002.

[49] R. Hilbert and D. Thevenin. Influence of differential diffusion on maximum flame temperature in turbulent nonpremixed hydrogen/air flames. *Combust. Flame*, 138:175–187, 2004.

[50] J.C. Hewson and A.R. Kerstein. Local extinction and reignition in nonpremixed turbulent co/h2/n2 jet flames. *Combust. Sci. Tech.*, 174:35–66, 2002.

[51] G.M. Goldin and S. Menon. A comparison of scalar pdf turbulent combustion models. *Combust. Flame*, 113:442–453, 1998.

[52] G.M. Goldin and S. Menon. A scalar pdf construction model for turbulent non-premixed combustion. *Combust. Sci. and Technol.*, 125:47–72, 1997.

[53] P. Sripakagorn, G. Kosaly, and H. Pitsch. Local extinction-reignition in turbulent nonpremixed combustion. annual research briefs, Center for turbulence research, 2000.

[54] Baris A. Sen. *Artificial Neural Networks based Subgrid Chemistry Model for Turbulent Reactive Flow Simulation*. PhD thesis, Georgia Institute of Technology, 2009.

[55] C. Sung, C. Law, and J. Chen. An augmented reduced mechanism for methane oxidation with comprehensive global parametric validation. *Proc. Combust. Inst.*, 27:295–304, 1998.

[56] N. Patel, M. Kirtas, V. Sankaran, and S. Menon. Simulation of spray combustion in a lean-direct injection combustor. *Proc. Combust. Inst.*, 31:2327–2334, 2007.

[57] N. Patel and S. Menon. Simulation of spray-turbulence-flame interactions in a lean direct injection combustor. *Combust. Flame*, 153:228–257, 2008.

[58] J. Cai, S.-M. Jeng, and R. Tacina. The structure of a swirl-stabilized reacting spray issued from an axial swirler. *AIAA-2005-1424*, 2005.

[59] F. Davoudzadeh, N.-S. Liu, and J.P. Moder. Investigation of swirling air flows generated by axial swirlers in a flame tube. E-15497, National Aeronautics and Space Administration, John H. Glenn Research Center at Lewis Field, Cleveland, Ohio, March 2006.